SPECTROSCOPIC STUDIES AND MATHEMATICAL MODELING OF LASER MATERIAL INTERACTION FOR DEVELOPMENT OF INTELLIGENT QUALITY MONITORING SYSTEM

by

Seung Hwan Lee

A dissertation submitted in partial fulfillment
of the requirements for the degree of
Doctor of Philosophy
(Mechanical Engineering)
at The University of Michigan
2013

Doctoral Committee:

Professor Jyotirmoy Mazumder , Chair

Professor Elijah Kannatey-Asibu Jr.

Professor Margaret S. Wooldridge

Associate Professor Kevin Patrick Pipe

To my lord and my family

But he knows the way that I take; when he has tested me, I will come forth as gold.

(Job 23:10)

ACKNOWLEDGEMENTS

First and foremost, I wish to express my deepest thanks to my advisor, Professor Jyoti Mazumder, for his supports and encouragements for my doctoral degree. He has advised me not only as an academic advisor but also as a senior in life. His patient guidance enabled this work. I also would like to truly appreciate my dissertation committee- Professor Elijah Kannatey-Asibu, Jr., Professor Margaret S. Wooldridge, and Professor Kevin Patrick Pipe. Their insights helped me to improve this dissertation.

I would like to thank to the National Science Foundation and Shinya Furusawa from Toyota for financial support during my research. Their supports and critiques helped me to improve this work.

I would like to thanks my colleagues at the Center for Laser-Aided Intelligent Manufacturing in the Department of Mechanical Engineering for enjoyable cooperation, discussion, and friendship: Joonghan Shin, Donghyuck Kam, Hyungmin Chae, Dongkyung Lee, Lijun Song, Ashish Dasgupta, Sudip Bhattacharya, Mohammad Khalid Imran, Frederick Ross Dunbar, William Charles Johnson, and Deborah M. Hemmeter.

I would like to thank my friends and seniors for their encouragements and friendships: Dr. Taeho Moon, Kwanchul Lee, Dr. Taehyung Kim, Dr. Gyemin Lee, and Wongun Choi.

I also would like to thank past and present members of Campus Town Church of Ann Arbor for their encouragements and prayers. Especially, I would like to express my heartful thanks to Ps. Sang Chun Park for his prayers and encouragements.

I would like to express thanks to my wife, Hanna Lim for her endless love and patience. Finally, I also appreciate my parents and my sister for their supports, encouragement, and pray to me. I cannot thank my wife, my parents and my sister enough. I will be forever grateful.

TABLE OF CONTENTS

LIST OF FIGURES

Chapter

Appendix A

LIST OF TABLES

Chapter

Appendix A

LIST OF APPENDICES

ABSTRACT

SPECTROSCOPIC STUDIES AND MATHEMATICAL MODELING
OF LASER MATERIAL INTERACTION
FOR DEVELOPMENT OF INTELLIGENT QUALITY MONITORING SYSTEM

by

Seung Hwan Lee

Chair: Jyoti Mazumder

This research investigates the fundamental physics of laser processing of multi-coated materials, through spectroscopic studies and a mathematical modeling of laser material interaction. This work focuses particularly on developing an in-situ quality monitoring system by detecting defects generated in the processing, understanding the effect of coated materials on defects formation, and further characterizing differences between newly developed lasers in regard to energy transfer.

First, several welding defects generated in CO_2 laser processing of a multi-coated material are monitored using Optical Emission Spectroscopy (OES). Tracking the specific constituent behaviors that induce the defects is proposed as a novel way to monitor the

process, since the OES can resolve the emission line of each constituent from among the emission spectra generated in the laser induced plasma of the processes where defects were present. Several detrimental defects frequently observed in the realistic production line, specifically, bead separation, underfill, burn-through, and pin-hole, are successfully detected using the features identified in the temporal evolution of the spectra.

Second, in order to obtain promising results in both defect detection and defect classification, a machine learning algorithm, a Support Vector Machine (SVM), is adopted for the spectral data analysis using the richness of the available data. The richness is a major benefit in the use of the optical emission spectroscopy because the spectrometer can resolve and distinguish each spectral line of the constituents of the target materials. Three classes are defined to classify the defects generated in the disk laser processing of the multi-coated material. Using the features extracted in the emission line of the constituent, the spectral data sets are trained. Based on the trained models, the multi-classification of the defect is successfully performed.

Third, a numerical simulation study is presented to investigate the effect of the coating material for understanding the interfacial phenomena in the laser processing of the multi-coated material. These interfacial phenomena are important because they determine the processed qualities of the target samples in the laser material interaction. The interfacial phenomena such as recoil pressure, capillary and thermo capillary force are investigated by comparing a coating free material with a coated material. As a specific case, zinc-coated steels are used. For this simulation study, a new computational module handling the zinc layers is established and is selectively applied for a comparative study between a zinc coated case and a zinc absent case. The hydrodynamic force induced by the vaporized zinc

induces an unstable energy balance of the liquid / vapor interface in the laser material interaction zone. Due to the vaporization pressure in the zinc layer, the liquid / vapor interface is found to be pushed backward, and hence this leads to a change of the molten flow at the position of the zinc layer. For the validation, reflective topography is used to measure the flow velocity of the two cases. The velocity of the liquid metal at the side wall of the L/V interface cavity in the zinc coated case is found to be almost double that of the zinc absent case.

Finally, characteristics of the energy transfer of the disk laser and the fiber laser are identified to provide users with insight into which laser might be more suitable for a given application. To assess the laser systems, two factors are considered: energy absorption by the laser induced plasma, which is an inevitable phenomenon in laser material interactions, and the penetration features of the samples irradiated by the attenuated laser beam after absorption by the plasma. The performances of the disk and fiber lasers, in terms of energy transfer, are found to be comparable. However, in high power densities, the disk laser has slightly deeper penetration of the target material than the fiber laser.

The work presented in this study can be utilized to achieve the quality assurance, to understand energy transfer in the laser material processing, and thus eventually to control the process.

CHAPTER 1

INTRODUCTION

1.1. Background

In recent decades, laser welding has been widely used as a technique for joining materials because a laser beam can join the material with minimal distortion and produce small heat affected zones on the target materials compared with other joining technologies. In addition, laser welding offers ease of automation and high welding speeds. For these reasons, laser welding is used in several fields such as automotive, medical, shipbuilding and aerospace industries, as illustrated in Figure **1-1**.

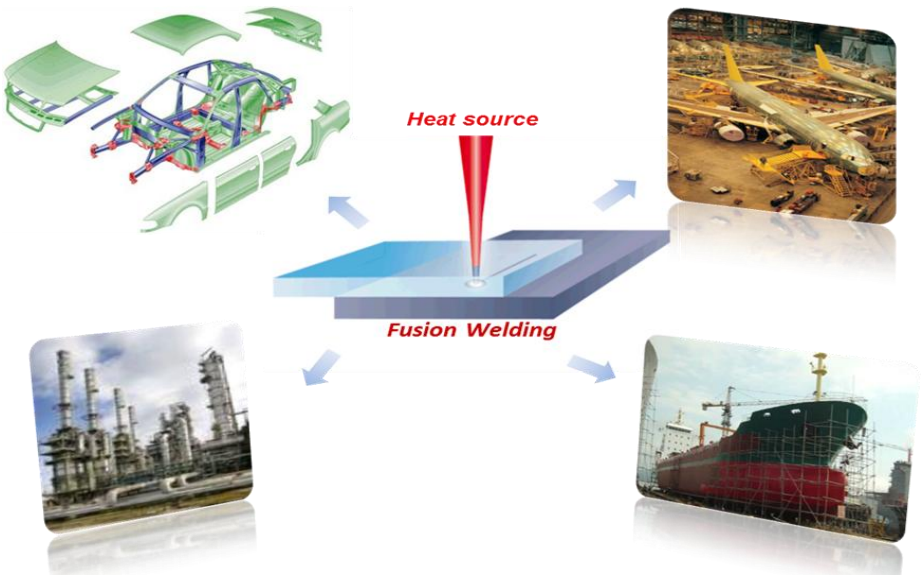

Figure 1-1 Various applications of the laser welding

Specifically, the auto industry in North America is shifting significantly toward laser welding from the traditional approach of spot welding for automotive body components. The main reasons for adoption of laser welding in the auto industry as a replacement for spot welding are that laser welding provides design flexibility by reducing steel required for tabs in spot welding, is easy to automate, has higher welding speeds and produces better welds. It also produces longer continuous welds that provide greater strength and can greatly reduce idle times between welds. Laser welding can help engineers make better trade-offs between weight and strength by reducing the size of the flange attached to the weld. In spot welding this flange can be as big as 15 mm. Laser welding can cut that by about 50 percent [1]. Moreover, in spot welding, the lower electrode sometimes needs an access hole to reach the lower part of the sheet metal to complete the two-sided welding process. However, laser welding does not require such a hole.

Volkswagen in Europe has the highest installation of lasers in production line and is the most aggressive manufacturer for using lasers in the body shop. However, other experienced European users like Volvo, Opel and Mercedes are transferring laser technology to Ford, GM and Chrysler in North America through their respective business alliances. A report by Jay Baron, Director of Manufacturing Systems at the Center for Automotive Research (CAR), based in Ann Arbor, claims that the auto industry is now considering expanding use of laser welding because of its benefits described above [1].

Despite its advantages, however, laser welding is not free of the welding defects common in all other welding techniques. Various types of welding defects are serious problems for quality assurance in welding production lines. When components are welded, a small defect in the weld can lead to scrapped parts, inferior quality, and requirements to

over-design welded joints to compensate for potential defects. In addition, the defects cause increased cycle time of the production lines, since the weld monitoring process is still largely manual and relies on the destructive testing after the welding process.

All these factors result in increased manufacturing costs and lost product value. For example, in the North American automotive industry alone, 14 million vehicles are produced annually. The scrap costs related to automotive body welding issues are estimated at $ 340 M (2007), and this is projected to grow to $434 M in five years (2012) [1]. This value is based on the automotive industry of North America alone.

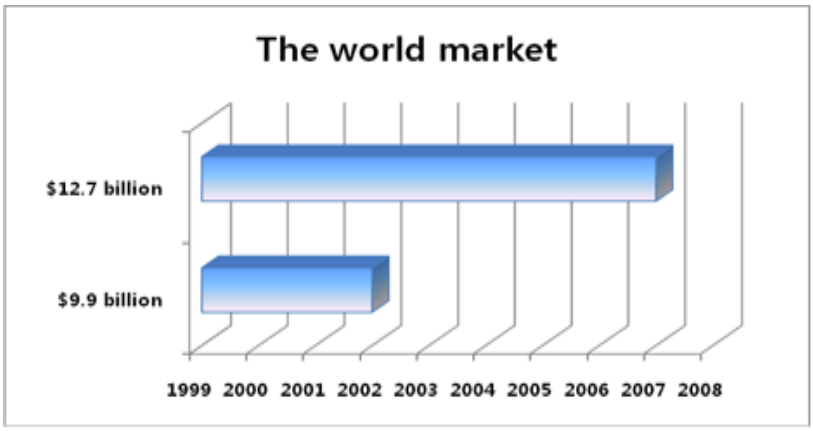

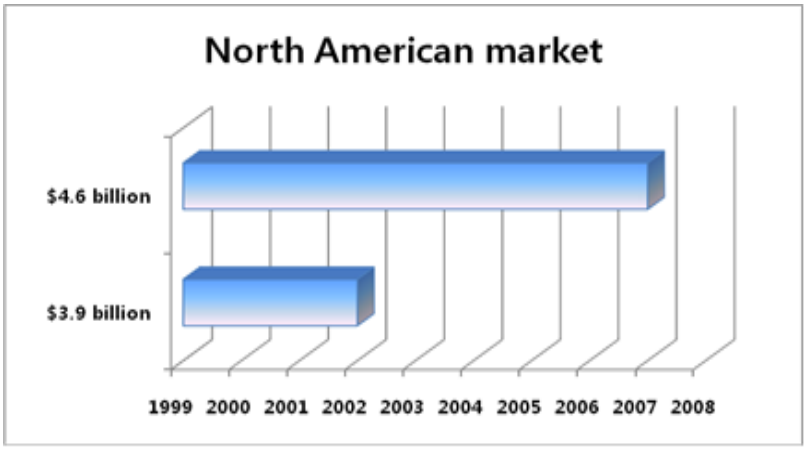

Figure 1-2 World market and North American market for welding [1]

In terms of the world welding market, the estimation was $ 9.9 billion in 2002 and was $ 12.7 billion in 2007, with an average annual growth rate of about 5.0% as shown in Figure **1-2** [1]. Among the world market, ~36% is focused in North America. Based on the annual growth rate, the market size in 2012, the estimation of the welding market in North America, would be $ 5.4 billion. In this huge market, 0.1% reduction of the scrap rate produces remarkable saving of the manufacturing cost. Therefore, the quality assurance in welding production lines is essential for the competitive manufacturing process.

1.2. Review of Quality Monitoring Methods

Much research has been conducted on defects monitoring using several techniques such as the ***acoustic emission*** method and the ***optical emission*** method, depending on the source of the monitoring signals, as illustrated in Figure **1-3**. The ***Acoustic Emission*** (AE) method captures the stress wave generated by the energy release from laser beam to the materials [2]. The wave can be divided into air-borne and structure-borne [3]. The structure-borne stress waves typically form the frequency bandwidth between 50 kHz and 200 kHz. Piezoelectric transducers are placed on the welding nozzle and welding materials for the measurement of the wave. For the air-borne emission, microphones are typically placed near the weld zone to detect the audible frequency in the range of 20 Hz-20 kHz [3, 4]. Using this AE method, several defects have been detected [5-7]. The details are summarized in Chapter II and omitted here.

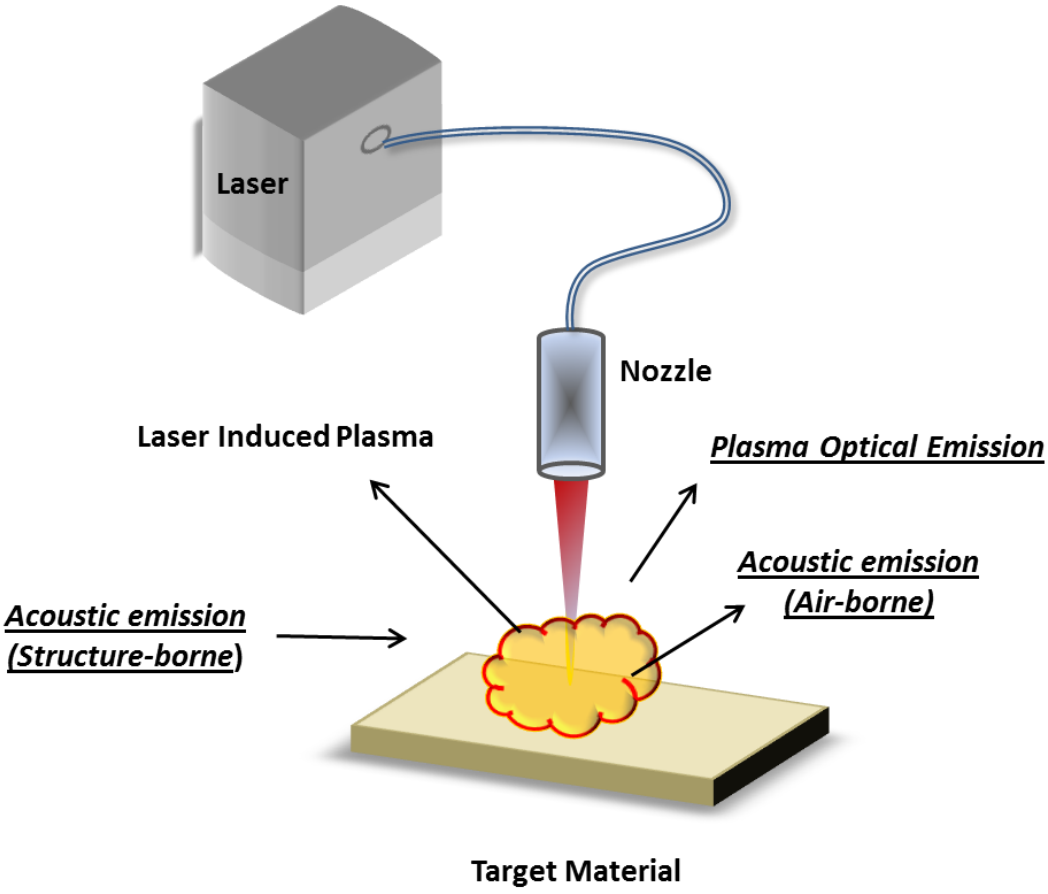

Figure 1-3 Various sources of signals for the quality monitoring methods

This AE method, though very popular, has some difficulties in the acquisition of the signals in mass production systems. These difficulties arise from the vibrations induced during the transfer of the target materials. Because of the vibration, it is hard to acquire the proper signal, since the piezoelectric transducers have to be mounted to the target materials. Moreover, the measurement of the audible signal includes the surrounding noise as well, due to the harsh manufacturing environment.

To circumvent these problems, the ***optical emission*** (OE) method is used as an alternative technique for monitoring welding defects, because the OE method is relatively

unaffected for the signal acquisition by the surrounding conditions, unlike the AE method. This OE method detects laser induced plasma as a monitoring target, using photodiodes that convert the optical emission into electrical signals. This laser induced plasma results from the laser energy absorption by the vaporized target materials. Thus, the evolution of the laser induced plasma reflects the energy absorption pattern during the process [8]. This pattern is closely related with the welding quality. For this reason, the OE method is highly suitable in welding defects monitoring. Using this OE method, several defects have been detected [4, 9-13]. The details are summarized in Chapter II and omitted here.

Although the OE method is popular for defects detections in the laser welding of two pieces of single substrate, these methods have a limitation in the laser processing of muli-layer or multi-coated substrates. In the multi-coated substrates processing, the optical emission characteristics are quite different from those of single material processing because of the various properties of coatings and layers. These differences often induce inadequacy of the photodiode for defects detection since a specific constituent often causes the defects. In other words, one or multiple constituents contained in a coating or one layer cause the instability of the entire process. However, because of the different atomic properties of constituents in each layer, the emission lines of the different constituents are frequently too spatially close to distinguish, or are overlapped. Therefore the photodiode, which converts the optical signal with broadband into one electrical signal, is inappropriate in the multi-constituent analysis; the spatial resolution of the photodiode is too low to track the behavior of constituent of interest. Moreover, as described in previous literature [4, 9-13], several photodiodes or one photodiode with customized optical filter were used for the quality monitoring because the experimental results showed that the use of one photodiode alone

cannot guarantee the quality monitoring. These set-ups result in additional cost when the target materials are changed in the production lines. For these reasons, an alternative method is required to overcome this problem. Optical Emission Spectroscopy (OES) with spectrometers can overcome this limitation, since the spectrometer can resolve and distinguish each spectral line of the constituents of interest. Several studies using the OES have been done for various purposes in laser material processing. The details are summarized in Chapter II and omitted here [14-18].

As described in the previous works [14-18], many of the studies focus on the laser energy absorption by the laser induced plasma. A few studies have been conducted on quality monitoring. However, the results of those studies have been too limited to apply in realistic cases, since the experiments have been conducted under the bead-on-plate conditions and on the joining of two pieces of single material.

1.3. Motivations and Objectives

Recently, the laser processing of multi-layer or multi-coated substrates has been receiving more attention to satisfy growing demands of customers, since various coatings and layers give desired functions to the primary material. Simultaneously, newly developed lasers have been increasing the efficiency of the laser material processing.

In the multi-coated substrates processing, the optical emission characteristics are quite different from those in single material processing, because differences of the physical properties exist between the base material and the coated materials or between each coating layer. These differences frequently induce welding defects in multi-layer material

processing. In addition, the differences cause dissimilarity of the interfacial phenomena in laser processing of the multi-layer materials, compared with that of the single material processing.

Hence, in this research, spectroscopic measurements of the laser induced plasma are performed to detect the welding defects and to understand characteristics of the interfacial phenomena. The research objectives are individually defined below:

1) Detect the laser welding defects using the principle of Optical Emission Spectroscopy (OES): As described above, differences of the physical properties exist between the base material and the coated materials or between each coating layer in multi-layer material processing. In the process, these different physical properties frequently induce the welding defects, and the conventional quality monitoring methods have limitations in detecting the defects, as described in Section 1.2. To overcome the limitations, the OES is adopted for the quality monitoring. Specifically, tracking the constituent behaviors that induce the defects is proposed as a novel way to monitor the process, since the OES can resolve the emission line of each constituent from the laser induced plasma in the defect-present cases. That is, the use of the OES gives more apparent spectral features than the use of the conventional quality monitoring method can give, since the conventional techniques convert spectral features of the broad band into one electrical signal. For the first time, using this OES, welding defects are monitored in the overlapped joints of sheet metals, the most preferred set-up in realistic laser fusion welding. Several detrimental defects, specifically, bead separation, underfill, burn-through, and pin-hole, which were not

observed in the use of the OE methods, are detected together. All detailed experiments are performed under the realistic conditions provided by Toyota.

Zinc coated steels are used for this study as the example of multi-coated materials. The zinc coated steels are popular structure materials, due to excellent corrosion resistance by the zinc layer. However, when zinc coated steels are welded using lasers, the zinc vapor is entrapped inside the liquid iron because of the difference between the boiling temperature of zinc (1180K) and the melting point of iron (1811K). The entrapped zinc vapor sometimes leads to the unstable process or the welding defects, resulting in a significant number of scrapped parts [17, 19-21]. The temporal evolution of zinc emission lines are monitored using a UV spectrometer, since the behavior of the zinc vapor inside the weld zone plays an important role in defects formation. Hence, in this study, the detrimental defects, specifically, bead separation, underfill, burn-through, and pin-hole, are detected using OES.

2) Detect and classify the welding defects using a machine learning algorithm: The laser induced plasma generates different spectra profiles based on laser types. Basically, the pre-described OES uses laser induced plasma as a monitoring target. Thus, the spectral line of our interest, which is used for the quality monitoring, sometimes has not been observed depending on the laser types. For example, the Zn I emission lines observed in the CO_2 laser (λ=10.6 μm) are not observed in the disk laser (λ=1.03 μm) welding of the zinc coated steels.

To overcome this problem, a statistical approach, a machine learning algorithm, is adopted with the OES method to detect and classify the laser welding defects. This approach produces promising results as data sets are statistically rich. The richness of the spectra data in the use of OES is a major benefit for the quality monitoring of the laser welding, compared to the use of the conventional OE method. In other words, while the OE method converts the certain band of the optical emission induced by the plasma into one electrical voltage or current, the spectrometer preserves the information of the several emission lines generated within the optical band. This difference indicates that the spectral features of the defect-present case in the OES case are more discriminative than those in the conventional quality monitoring method. Therefore, the rich input data enable better performances in the defect detection. Further, the classifications of the defects are conducted. Theses classifications give useful information to operators in production lines, because they can recognize the existing problems depending on the type of defects and further the recognition can directly lead to feedback control of the defects in the production lines. Hence the defections and classifications of the defects are performed in this section.

3) Understand the mechanisms of defects formation in the multi-layer substrates processing using the Computation Fluid Dynamics (CFD) method: In laser material processing, phase changes of materials, such as solid/liquid (S/L) and liquid/vapor (L/V), frequently occur, depending on laser power, since the intensive photon energy of the laser beam is transferred to the material [22]. These phase changes play a significant role in processing quality, since complex time-varying interfacial phenomena, such as recoil

pressure and surface tension, determine the resulting energy transfer pattern [23, 24]. Especially, phase change of materials from liquid to vapor plays a critical role in the quality of the samples in high-density laser material processing between 10^9 and10^{12} W/m^2, since various pressures mainly induced by vaporization of materials are exerted on the liquid/vapor (L/V) interface [22]. As described above, the characteristics of the interfacial phenomena in the multi-layer substrates are quite different from those of the single-layer material processing because of the difference of the physical properties between the base material and the coated materials or between each coating layer. Therefore, in order to obtain better qualities of the welded samples, understanding the role of the coating material on the liquid / vapor interface is required. Hence, in this study, the interfacial phenomena such as recoil pressure, capillary force and thermo capillary force are investigated by comparing a coating-absent case with a coating-present case. As a specific case, the zinc coated steels are employed. From this comparative study, the mechanism of the defect formation is found in the high-density laser material interaction.

4) Characterize the energy transfer of two recently-developed laser systems, the fiber laser and disk laser, through the spectroscopic measurements of the laser induced plasma. Due to relatively small footprint and excellent wall plug efficiency, diode pumped solid state lasers (DPSS) have been utilized in the laser material processing field [22]. However, the DPSS has an inherent problem called thermal lensing resulting from different thermal gradients of the gain medium, which causes a limitation in laser beam

quality [25, 26]. To improve beam quality by overcoming this issue, a disk laser and a fiber laser have been developed as alternatives to the conventional lasers [26, 27].

Even though the disk and fiber laser systems are promising solutions, laser-users need information regarding selections of the laser based on their specific need, particularly in terms of energy transfer. To assess the laser systems, two factors are considered: energy absorption by the laser induced plasma, which is an inevitable phenomenon in laser material interactions, and the penetration features of the irradiated samples by the attenuated laser beam after absorption by the plasma. Hence, in this section, characteristics of energy transfer of two laser systems, the fiber laser and disk laser, are investigated through the spectroscopic studies of the laser induced plasma and the penetration features of the sample irradiated by the attenuated beam.

1.4. Dissertation Outline

This research consists of Chapter II-V (technical chapters) and one appendix (a commercialization plan of this research). In Chapter II, the spectroscopic study of welding defects in CO_2 laser material processing will be described. In Chapter III, the spectroscopic study to detect welding defects in disk laser material processing will first be described. Then the application of the Support Vector Machine, which is a machine learning algorithm, for the classification of the welding defects, will be discussed. In Chapter IV, the results of the numerical study of the liquid / vapor interfacial phenomena in multi-coated material processing will be discussed to investigate the physical mechanism for forming defects. In Chapter V, the characteristics of the energy transfer both in the disk laser and the fiber laser

will be described based on the spectroscopic study. In the appendix, the business plan built in the Ross School of Business for commercialization of this research will be presented.

Chapter II focuses on the monitoring of the defects generated in the lap joint welding of multi-zinc coated steels using the OES. The defects generated in the CO_2 laser material processing on the zinc coated steels are experimentally simulated, specially focusing on the gap effect between the overlapped joints. Sheet metals consisting of zinc coated steels are materials used in the production lines of Toyota. As a first step in this study, the spectrum of the plasma in the zinc coated steels welding is measured. An ultra-violet spectrometer is used for the measurement of the spectra. The observed emission lines are identified using the National Institute of Standards and Technology (NIST) and the Harvard-Smithsonian Center for Astrophysics (CFA) data bases [28, 29]. Then, the specific conditions leading to failures of welding are identified to monitor several detrimental defects, specifically, bead separation, underfill burn-through, and pin-hole, frequently observed in the realistic production line. Those defects result from existing small gaps between the sheet metals. In order to simulate the gap effects, several spacers with different thickness are placed between the overlapped joints along the longitudinal direction of the samples. These defects are simultaneously correlated with the temporal evolution of the Zn I emission lines for the purpose of quality monitoring. Prior to the correlations, spectroscopic parameters are investigated to find the most suitable line among the several emission lines for the quality monitoring. In order to validate the features of defects, the welded samples by the CO_2 laser are cut and etched using 2.4% nitric acid and 97.6% ethylene. The features of the zinc emission line are studied in each defect case.

Chapter III focuses on detecting of defects generated in disk laser welding and the classification of the defects using SVM. As an initial step, the optical emission spectrum of the plasma was measured during the disk laser welding of the zinc-coated steels. The reasons for the different spectra profiles generated in the disk laser welding are discussed and compared to the results in Chapter II. Then, a statistical approach is combined with the OES method to detect and classify the welding defects using the characteristics of spectra correlated with the defects. The SVM is used to classify the defects. The experiments are divided into three classes, no-gap condition, underfill, and bead separation, since those defects are realistic concerns for the production lines. Two evident features, the average intensity and the standard deviation of the Fe I emission intensities in each defect-present case, are individually extracted through the series of the experiments. The spectra data are optimized for training features observed through the experiments. The trained models, $\mathbf{w}$ and b, are obtained by the features. The classification results are presented using the hyperplane, $\mathbf{w}^t\mathbf{x}$-b=0, which is defined by the trained models. Classifications tests using the cross-validation are performed.

Chapter IV investigates that the characteristics of the interfacial phenomena in the laser processing of the multi-coated materials compared with that of the single material processing using the Computation Fluid Dynamics (CFD) method. As a specific case, the effect of the zinc coating on the interfacial phenomena is studied in the high-density laser material interaction in the zinc coated steel. Specifically, the role of the coating layer in the transition of the interfacial physics, such as penetration depth, capillary force, temperature, thermo-capillary force and recoil pressure, considering the hydrodynamic force driven by the vaporized zinc. In order to investigate the effect of the zinc coating on the L/V

interfacial behavior, the previous mathematical model built in our group [19, 23, 30] is further developed. This model adopts a mathematical technique called level set method to track the L/V interface self-consistently by solving the Navier's stokes equation, continuity equation and energy equation. A new computational module regarding the zinc layers is established and is selectively applied for a comparative study between a zinc coated case and a zinc absent case. Hence, the zinc coated case and the zinc absent case are compared simultaneously under the same process parameters, such as laser power and scanning speed. At the same time, an optimized reflective topography is used as a method of experimental validation. The laser material interaction zone covered by bright laser induced plasma is clearly visualized by controlling the reflective beam from the interface zone. From the visualization, several physical phenomena are investigated. This result can be a guideline for the processing of the multi-layer substrates.

Chapter V explains the characteristics of energy transfer of two laser systems, the fiber laser and disk laser, to provide users with insight into which laser might be more suitable for a given application. Spectroscopic studies are performed to investigate the characteristics of energy transfer of two laser induced plasmas. First, electron temperatures are calculated to compare the two cases. These electron temperatures are obtained under an assumption of the local thermodynamic equilibrium (LTE). In order to validate the assumption, the electron density is calculated. For the calculation, line broadening is used to measure the electron density. The electron temperature is evaluated from the observed Fe I lines using the Boltzmann plot, whereas the electron number density is determined from the broadened Fe I 381.58 nm line. Based on the electron temperature and electron density, the coefficients of Inverse Bremsstrahlung are estimated to compare the energy absorption

by the plasma in the two systems. In addition, the LTE assumption is validated using those two parameters. The penetration characteristics of the sample welded by the two laser systems are examined to study the role of the attenuated beam by the plasma absorption. The experimental sets are divided into four groups to investigate the penetration characteristics depending on laser power. The laser powers are 1 kW, 2 kW, 3 kW and 3.9 kW in each set. The 3.9 kW is used instead of 4 kW for the protection of the laser systems. The corresponding power densities are 3.1×10^9 W/m^2, 6.2×10^9 W/m^2, 9.3×10^9 W/m^2 and 12.4×10^9 W/m^2, respectively. To investigate the clean boundaries of the re-solidification area, 2.4 % nitric acid and 97.6 % ethylene are used for the chemical etching. All the experiments were conducted under bead-on-plate conditions. Based on the observed features, the performances of the disk and fiber lasers, in terms of energy transfer, are compared.

Chapter VI describes the contributions, limitations and recommendations of this research.

The Appendix presents a commercialization business plan. This business plan was established by a team of five people, including the author, through the MBA course (FIN 629) that is offered in the Ross school of Business. This plan covers the technology review and Intellectual Property (IP) review prior to entry into the real market. In addition, the realistic market size is professionally estimated. Based on the reviews, a company strategy and a development plan were built. This business plan has enabled the startup of SenSigma LLC. through the support of the Michigan government and the office of Technology Transfer (University of Michigan).

CHAPTER 2

SPECTROSCOPIC MEASUREMENTS OF LASER INDUCED PLASMA FOR DEFECT DETECTION IN CO_2 LASER MATERIAL PROCESSING

In this chapter, Optical Emission Spectroscopy (OES) is used to detect welding defects generated in CO_2 laser material processing. Specifically, tracking the constituent behaviors which induce the defects is proposed as a novel way to monitor the process, since the OES can resolve the emission line of each constituent from the laser induced plasma. Using this OES, welding defects are monitored in the overlapped joints of sheet metals, the most preferred set-up in realistic laser fusion welding.

2.1. Introduction

Laser welding has been widely used as a novel joining technique in the automobile, medical, shipbuilding and aerospace industries, since a laser beam can join materials with minimal distortion and a smaller heat affected zone on the target materials, compared with other joining technologies [22].

When several components are welded, one small defect leads to huge expenses to compensate for the defect. For example, in tailored-welded blanks technology, effective for joining several pieces of sheet metal, a welding defect can cause the loss of the entire welded part. In general, a typical automobile body consists of more than 300 pieces, and 12 % of the total cost is related to welding [22]. Therefore a well-established quality monitoring system is required to reduce manufacturing cost.

In laser welding, much research has been conducted for defects monitoring using several techniques such as the Acoustic Emission (AE) and the Optical Emission (OE) method, depending on the monitoring targets. The AE method captures the stress wave generated by the energy release from laser beam to materials [2]. The wave can be divided into structure-borne and air-borne [3]. The structure-borne stress waves typically form the frequency bandwidth between 50 kHz and 200 kHz. Piezoelectric transducers are placed on the welding nozzle and welding materials for the measurement of the wave. For the air-borne emission, microphones are typically placed near the weld zone to detect the audible frequency in the range of 20 Hz-20 kHz [3, 4].

Duley *et al.* analyzed acoustic signals generated during the laser welding of Al 1100 [6]. Fast Fourier Transform (FFT) was used to correlate the signal with the weld penetration of the sample. They found that the range of 3-9 kHz was associated with the closure of the keyhole, which is a cavity formed by liquid / vapor interface, throughout the process. Moreover, the frequency band between 9-10 kHz was found to be correlated with the ablation of surface oxide in the Al samples. Kannatey-Asibu and Liu developed a mathematical model to correlate AE with martensitic transformation [5]. The amplitude of the AE signal was found to be inversely proportional to the distance between the position of

the transformation and the location of the sensor. In addition, they found that the AE signal was correlated with carbon content during the martensitic formation. Luo *et al.* tried to detect welding defects arising from misalignment and gap in butt welding from the AE signal [7]. They found that the signal in the range of 10-20 kHz represented the characteristics of sound welds. Additionally, a wavelet transform was used to decompose the signal into several frequency bandwidths. They concluded that the intensity of the frequency band below 718 Hz decreased dramatically when welding defects existed. This AE method, though popular, has some difficulties for acquiring the signals in mass production systems. These difficulties arise from the vibrations induced during the transfer of the target materials. Because of the vibration, it is hard to acquire a proper signal, since the piezoelectric transducers have to be mounted to the target materials. Moreover, the measurement of the audible signal includes the surrounding noise as well, due to the harsh manufacturing environment.

To circumvent these problems, the optical emission (OE) method is used as an alternative technique for monitoring welding defects, because the OE method is relatively unaffected in the signal acquisition by the surrounding conditions, unlike the AE method. This OE method detects laser induced plasma as a monitoring target, typically using photodiodes which convert the optical emission into an electrical signal. The laser induced plasma results from the laser energy absorption by the vaporized target materials. Thus, the evolution of the laser induced plasma reflects the energy absorption pattern during the process. This pattern is closely related with the welding quality. For this reason, the OE method is highly suitable for use of the welding defects monitoring.

Miyamoto *et al.* studied plasma behavior to monitor welding defects generated in the CO_2 laser welding of mild steels with five photodiodes [9]. These five photodiodes were located at both the top and the bottom of the samples. They found the optimal position of the photodiodes to observe the behavior of the laser induced plasma by changing process parameters, such as laser power, welding speed, and flow rate of shielding gas. Through the measurement, several weld defects such as underfill and pits were detected by the photodiodes. Park *et al*. detected the plasma generated in CO_2 laser welding using ultraviolet (UV) and infrared (IR) photodiodes [31, 32]. Based on this measurement, they classified factors that can affect weld qualities into five categories: optimal heat input, low heat input, slightly low heat input, partial joining, and nozzle deviation. The measured signals were correlated with the welding quality. Tu and Miyamoto investigated deep penetration welding using a photodiode array with optical filters, using a 20 kW CO_2 laser [12]. They studied the behaviors of the keyhole plasma located inside the materials and the plasma plume formed above the top surface of the target materials, for the purpose of monitoring the welding. This group concluded that the light emission in the green spectral region was the preferred target for the welding quality monitoring because of the low scattering of the plasma in that region. Kannatey-Asibu *et al.* presented an overview of several monitoring methods, in terms of features, benefits, and drawbacks [11, 33]. They then established a sensor fusion system consisting of IR, UV and AE sensors to diagnose full penetrations in 1018 cold rolled lap welding using a CO_2 laser. In order to correlate the measure signals with the full penetration welding, they used feature extraction methods such as singular value decomposition and class mean scatter. From the data analysis, they detected the full penetration of the weld in both laboratory and production successfully.

Although the OE method is popular for the defects detections in the laser welding of two pieces of single substrate, these methods have a limitation in the laser processing of muli-layer or multi-coated substrates. Recently, the laser processing of the multi-layer or multi-coated substrates has been receiving more attention to satisfy growing demands of customers, since various properties of coatings and layers give desired functions to the primary material. In the multi-coated substrates processing, the optical emission characteristics are quite different from those of single material processing because of the various properties of coatings and layers. These differences often induce inadequacy of the photodiode for defects detection since a specific constituent often causes the defects. In other words, one or multiple constituents contained in a coating or one layer cause the instability of the entire process. However, because of the different atomic properties of constituents in each layer, the emission lines of the different constituents are frequently too spatially close to distinguish, or are overlapped. Therefore the photodiode which converts the optical signal with broadband into one electrical signal is inappropriate in the multi-constituent analysis; the spatial resolution of the photodiode is too low to track the behavior of constituent of interest. Moreover, as described above, several photodiodes or one photodiode with customized optical filter were used for the quality monitoring because the experimental results showed that the use of one photodiode alone cannot guarantee the quality monitoring. These set-ups result in additional cost when the target materials are changed in the production lines. For these reasons, an alternative method is required to overcome this problem. Optical Emission Spectroscopy (OES) with spectrometers can overcome this limitation, since the spectrometer can resolve and distinguish each spectral line of the constituents of interest.

Several studies using the OES have been done for various purposes in the laser material processing. Rockstroh and Mazumder studied attenuation and refraction of the laser beam, when the beam passed through the plasma in CO_2 laser welding, using the OES [14]. Electron temperature and electron density of the plasma were calculated. These two parameters were used to estimate the Inver Bremsstrahlung absorption, which explains absorption of incident beam from the laser. Based on the result, they determined the transmitted energy from the laser to the target material. Mazumder and Lober used the OES to study the energy transfer of the plasma induced by a 10 kW CO_2 laser [18]. The absorption and the refraction of the CO_2 laser beam in the plasma were determined. The electron temperature distribution of the plasma was calculated. They reported that the electron temperature in the plasma core was in the range of 14000-15300 K, and 7.5-29 % of the incident laser power was absorbed by the plasma. Balzer *et al*. developed a method to characterize zinc coating thickness in zinc-coated steel [16]. A flash-lamp pumped Q-switched Nd:YAG laser was used for the experiments. A 200-780 nm spectrometer was used to obtain spectral information of the laser induced plasma. Two emission lines, Fe I 438.35 nm line and Zn I 472.22 nm line, were used to determine the coating thickness. They concluded that the spectral ratio of the Fe I line and the Zn I line could characterize the zinc coating thickness. Ancona *et al.* performed a spectroscopic study for weld defects detection, using CO_2 laser with AISI 304 stainless steel plates under bead-on-plate conditions [15]. Electron temperatures were calculated using the Fe I, Cr I, and Mn I emission lines existed inside the plasma. The temperatures were correlated with laser welding defects such as crater formation, lack of penetration, welding disruptions and seam oxidation using the mean value and the standard deviation of the temperature. Sibillano *et*

al. conducted research on AA5083 aluminum using the OES [17]. They found a correlation between spectral characteristics and oxidation layer formation in the CO_2 laser aluminum processing. They concluded that shielding gas conditions affected the loss of the magnesium, which caused the formation of oxidation layer on the sample.

As described above, many of the studies focus on the laser energy absorption by the laser induced plasma. A few studies have been conducted on quality monitoring. However, the results of those studies are limited in their applicability to realistic cases, because the experiments in other studies above have been conducted under the bead-on-plate conditions and on the joining of two pieces of single material. Additionally, the defect detection was mostly correlated with the evolution of the electron density and temperature estimation, both of which sometimes contain fitting errors, rather than focusing on the evolution of emission lines, which gives greater accuracy.

Hence, in this chapter, defect detection in overlapped joints of sheet metals, which is the preferred setup in realistic laser fusion welding, are investigated. Zinc coated steels were used for this study as a multi-coated material. The zinc coated steels are popular structure materials, due to their excellent corrosion resistance by the zinc layer. However, when the zinc coated steels are welded using lasers, the zinc vapor is entrapped inside the liquid iron because of the difference between the boiling temperature of zinc (1180K) and the melting point of iron (1811K). The entrapped zinc vapor sometimes leads to the unstable process or the welding defects, resulting in a significant number of scrapped parts [17, 19]. In order to solve this problem, the sensitive gap control (below 0.1mm) between the zinc coated steels is required in the lap welding because the entrapped zinc vapor needs to be partially ventilated through the gap. However, if the gap is too large, the several

welding defects, leading to the scrapped parts, are generated. Therefore, sound quality monitoring is required to reduce the manufacturing cost. The temporal evolution of a zinc emission line is monitored using a UV spectrometer to detect welding defects, since the behavior of the zinc vapor inside the weld zone plays an important role in defects formation. Several detrimental defects, specifically as bead separation, underfill burn-through, and pin-hole, all of which are frequently observed in the realistic production line (Toyota), are detected.

2.2. Experimental Set-up

A schematic of the experimental set up consists of a laser, target materials, and a spectrometer connected with a computer, as shown in Figure **2-1**. A Trumpf TLF 5000 6 kW CO_2 laser was connected with an Allen Bradley PLC controller. This laser had a concentric nozzle for the laser beam delivery. The beam mode was TEM_{00}. The spot size of the laser beam was 0.5 mm at the top surface of the material. Helium gas was used as a shielding gas, since it can reduce degree of ionization, due to the high ionization potential. The optimal conditions for the zinc coated steel welding were 2.9 kW (laser power), 65 ipm (welding speed), 40 SCFH (shielding gas flow rate).

A spectrometer manufactured by Ocean Optics was used to monitor spectral signals from the CO_2 laser induced plasma. An optical fiber with 50 μm diameter was used to deliver the spectral signal to the 10 μm entry slit of the spectrometer. The detectable spectral range of the spectrometer was between 268 nm and 488 nm. It has 0.14 nm spectral resolutions. The collimating lens was located off the co-axis. The sampling time was 1 ms.

The materials used in this study were zinc coated sheet plates with lap joint configurations. The dimensions of the material were 5mm in width, 0.83 mm in thickness and 10 mm in length. Zinc was coated with 7 µm thickness on both sides. In order to simulate the defects which are frequently occurred in the manufacturing environment (Toyota, Japan), the spacers between 0.1 mm thick and 0.5 mm thick were used to generate various gap conditions between lap joints. The spacers were inserted at both ends along with longitudinal direction. During the experiments, the process parameters such as shielding gas flow rate, laser power, and welding speed were fixed. The spectral signals in each experiment were recorded under the fixed sampling time described above. For burn-through defect, one of the simulated defects, the higher laser power (4 kW) was set because it generates the excessive heat input that causes the burn-through defect.

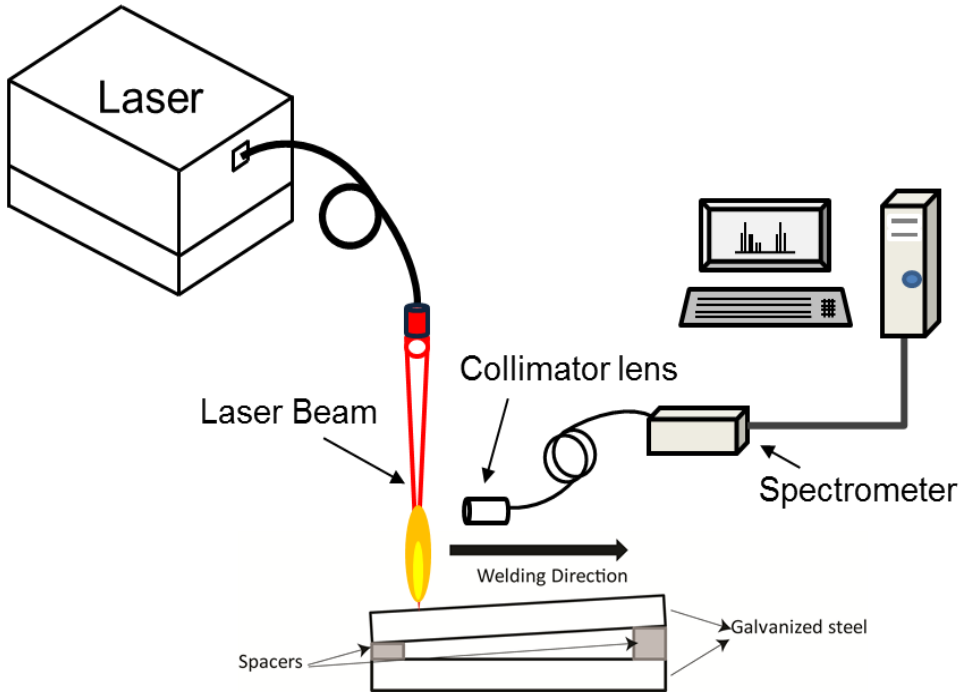

Figure 2-1 A schematic diagram of experimental set up

2.3. Results

2.3.1. Spectra Measurements

Prior to the defect detections, the spectrum of the plasma induced by CO_2 laser was measured in the laser welding of the zinc coated steels welding, as shown in Figure 2-2. Most of the emission lines are identified to Fe I lines: 373.5 nm, 375.8 nm, 376.67 nm, 380.17 nm, 382.18 nm etc. As shown in Figure 2-2, in the observed spectra, six emission lines with relatively high intensities were observed. The six lines are found to be Zn I lines: 328.2 nm, 330.3 nm, 334.5 nm, 468 nm, 472.2 nm, and 481.1 nm. The emission lines are identified using the National Institute of Standards and Technology (NIST) and the Harvard-Smithsonian Center for Astrophysics (CFA) data bases [28, 29].

One noticeable feature was observed during the process; while the Fe emission lines sometimes disappeared in the certain sampling time, the six zinc lines were continuously observed. This difference results from the difference of the spectroscopic properties between the Zn and Fe emission lines. As described in Table **2-1** the transition probabilities of Zn I lines are overall higher than those of the Fe I lines (1.41×10^6, 1.39×10^6, 9.66×10^6, 6.59×10^6 and 7.77×10^6). The values are almost one order higher than those of Zn I lines. Physically, this difference indicates that the transition of the electron between the excited level and ground level in the Zn I emissions is more easily generated than that in the Fe I emissions. For this reason, the zinc emission lines were continuously observed during the experiments.

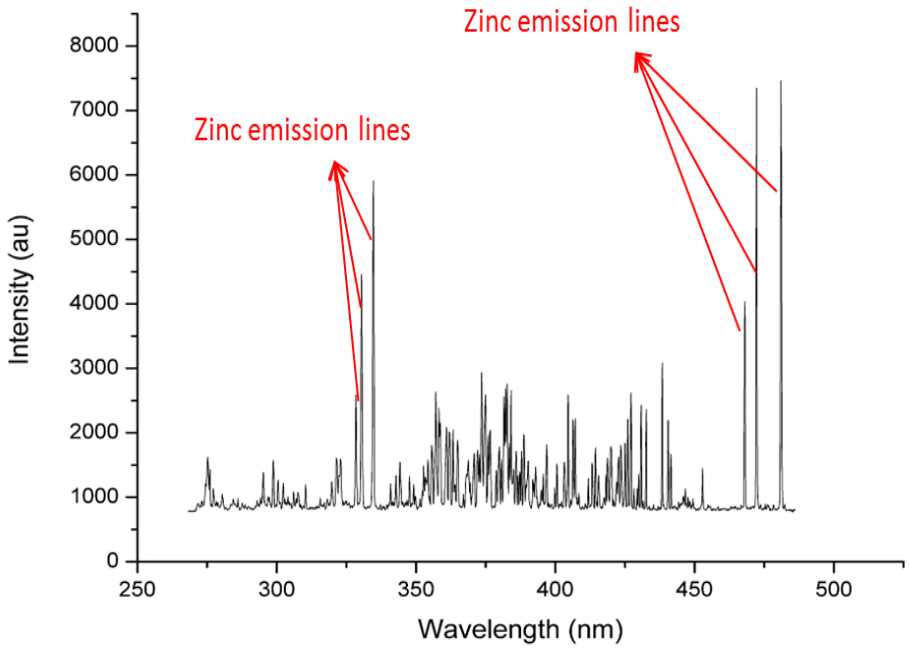

Figure 2-2. Spectra acquired from the plasma in the zinc coated steel welding

Fundamentally, the emission spectrum is described by the following equation [34]:

$$I_{mn} = N_m A_{mn} h \nu_{mn} \tag{2.1}$$

where I_{mn} is the relative spectral intensity, N_m is the upper (excited) state population, A_{mn} is the transition probability between two quantized energy levels (m,n), h is Planck's constant and ν_{mn} is frequency. As shown in the equation, the transition probability is the dominant factor that produces the high-intensity of the Zn I emission lines, compared with those of the Fe I lines, since the line broadening between the Zn I and Fe I emission lines does not show a big difference. That is, other terms of the equation (2-1) on the right hand side, do not exhibit much difference between the Fe I and Zn I emission lines because the 3rd term

and 4^{th} term are the Plank's constant and the frequencies observed above. The 1^{st} term is the upper state population, which can be estimated from the broaden emission line. However, the emission line widths do not show much difference between the Fe I and Zn I emission lines. Therefore, the dominant term is the transition probability, which shows one order difference between the Zn I and Fe I emission lines, as explained above. For this reason, the Zn I emission lines show higher intensity than the Fe I emission lines. The details of line broadening will be discussed in Chapter V.

Table 2-1 Spectroscopic properties of the Zn I emission lines

Wavelength λ (nm)	Transition Probability A (s^{-1})	Statistical Weight		Energy Level (cm^{-1})	
		g_n	g_m	E_n	E_m
328.2	8.66×10^7	3	1	32311.35	62 768.77
330.3	1.07×10^7	5	3	32501.42	62 772.00
334.5	3.75×10^7	7	5	32890.35	62 776.95
468	1.55×10^7	3	1	32311.35	53 672.24
472.2	4.58×10^7	3	3	32501.42	53 672.24
481.1	7.0×10^7	5	3	32890.35	53 672.24

2.3.2. Defect Detections

As described above, tracking the behaviors of the specific constituent which induce the defects is proposed as a novel way to monitor the process. In the laser welding of the

zinc coated steels, the entrapped zinc vapor inside the liquid iron mainly causes the instability of the process. Therefore, our interest is to monitor the zinc behavior for the defect detections. Several detrimental defects frequently observed in the production lines are tried to observe.

2.3.2.1. Bead Separation

Bead separation indicates the failure of joining two materials. The bead separation induced by the existence of the sufficient gap between the overlapped plates is a serious problem in the sheet metal welding. In order to simulate the bead separation, several welding experiments were conducted under the various gap conditions from 0.1 mm to 0.5 mm. As shown in Figure **2-1**, spacers with different thickness were inserted at both ends of the samples.

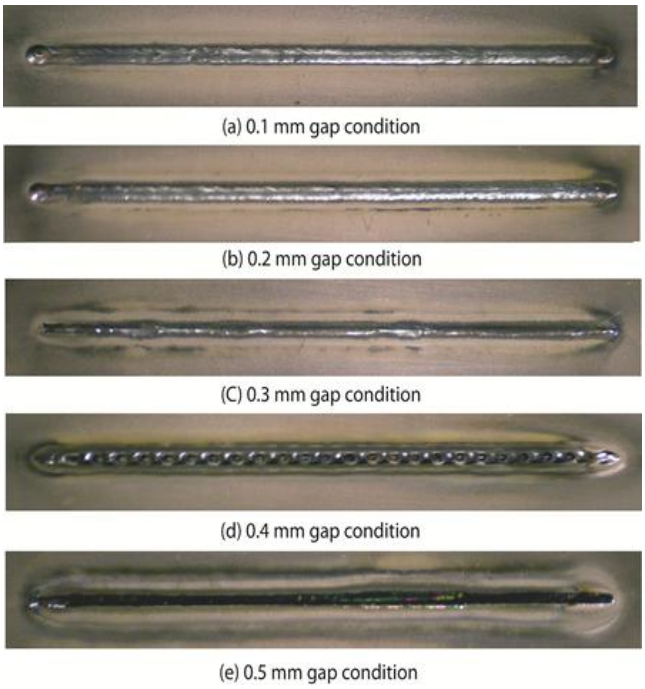

Figure 2-3 Top views of the welded sample in each gap condition from 0.1mm to 0.5 mm

Figure **2-3** shows the top views of the welded samples in each gap condition from 0.1mm to 0.5 mm. The top picture (a) is the result of the 0.1mm case. The bottom picture (e) is the result of the 0.5 mm gap. Through the 0.2 mm gap, the shapes of the weld seams were uniform. However, from 0.3 mm gap to 0.5mm gap, the shapes become non-uniform and the seams are partially separated into two parts. In other words, the welds have partially failed and the bead separations have occurred. Especially, for the 0.5 mm case, only the upper plate is melted because of the large gaps compared with the material thickness.

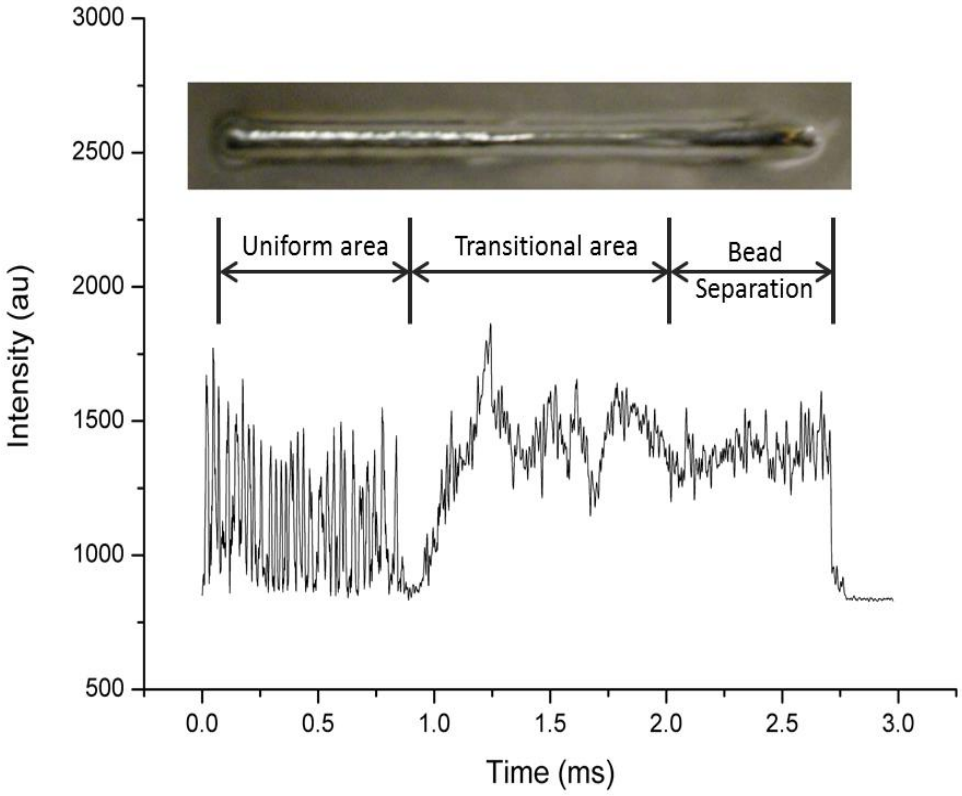

Figure 2-4 Characteristic of the transitional behavior between the 0.2mm gap and 0.5mm gap, correlated with of the Zn I line (481.1nm)

In order to detect the transition in which the bead separation occurs, experiments with different gap at both ends (0.2mm gap and 0.5mm gap, respectively) are performed. A temporal evolution of the Zn I 481.1nm was correlated with the welds result.

Figure **2-4** shows the transitional behavior of the experimental results between the 0.2 mm and 0.5 mm gap, correlated with the temporal evolution of the Zn I emission line (481.1 nm). The spectral intensity of the Zn I line shows a sudden change near 0.8 sec. The standard deviation of the spectral intensity up to 0.8 sec is ~304, and the mean value of the spectral intensity is 1129. In the transitional area, between 0.8 sec and 2.0 sec, the intensity is sharply increased. In this region, the standard deviation begins to decrease. After the bead separation occurs, the standard deviation of the spectral intensity becomes ~94, one-third of the standard deviation before the bead separation. Moreover, the mean of the intensity is increased to 1432. Physically, the standard deviation and mean value of the spectral intensity indicate the fluctuation of the zinc vapor that is entrapped inside the laser material interaction zone. That is, the reduced standard deviation explains that the zinc vapor escapes through the gaps that produce the bead separation. Once the gap is sufficient to generate the bead separation, when the gap is ~37.5 % of the thickness of the material, the laser welding fails. In other words, the generation of the keyhole, which is the cavity formed in the laser-material interaction-zone, fails in the lower sheet metal. Inside this cavity called the keyhole, the photon energy of the laser beam is absorbed through the multiple reflection of the laser beam. Therefore, most of the zinc vapor is generated from only the upper plate, since the keyhole generation fails in the lower plate. Consequently, in the range of 0.1 mm and 0.2 mm gap conditions, the zinc vapor is entrapped and oscillates inside the cavity, since the entrapped vaporized zinc is mainly generated from the

overlapped zinc coating located between the upper plate and lower plate. However, if the gap is larger, the vaporized zinc can escape through the gap located between the two plates.

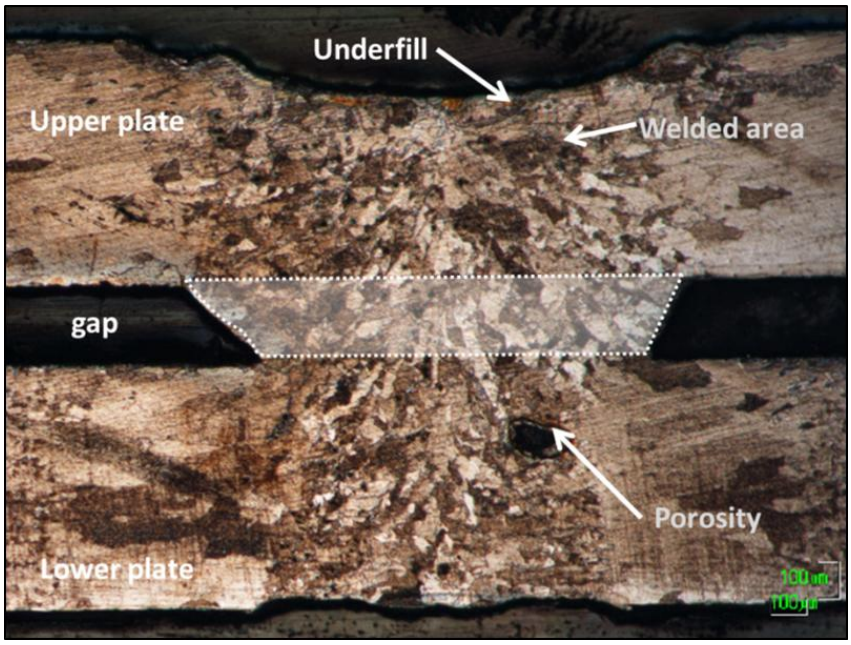

Figure 2-5 An optical microscopic picture of the welded zone in case (a) of Figure 2-3

2.3.2.2. Underfill

The second defect monitored is underfill, which results from a small gap compared to the gap that produces the bead separation. This underfill is mainly caused by two reasons: existing small gaps in the lap joints of the materials and dropped material filling up the gap created by the melting of the upper plate. This defect is one of the serious problems in the laser welding because it weakens joining strength. The cases (a) and (b) in Figure **2-3** are underfill defects. Specifically, Figure **2-5** illustrates the optical microscopic picture of the underfill defect generated from the case (a) of Figure 2-3. The shaded area surrounded by

the white dotted line, between the upper and lower metal plates, is almost identical with the amount of the dropped material which forms underfill at the top plate. Physically, this is reasonable because the amount of the mass lost by evaporation is small in the laser welding, because the energy density and interaction time in the laser welding is optimized just for melting of the materials.

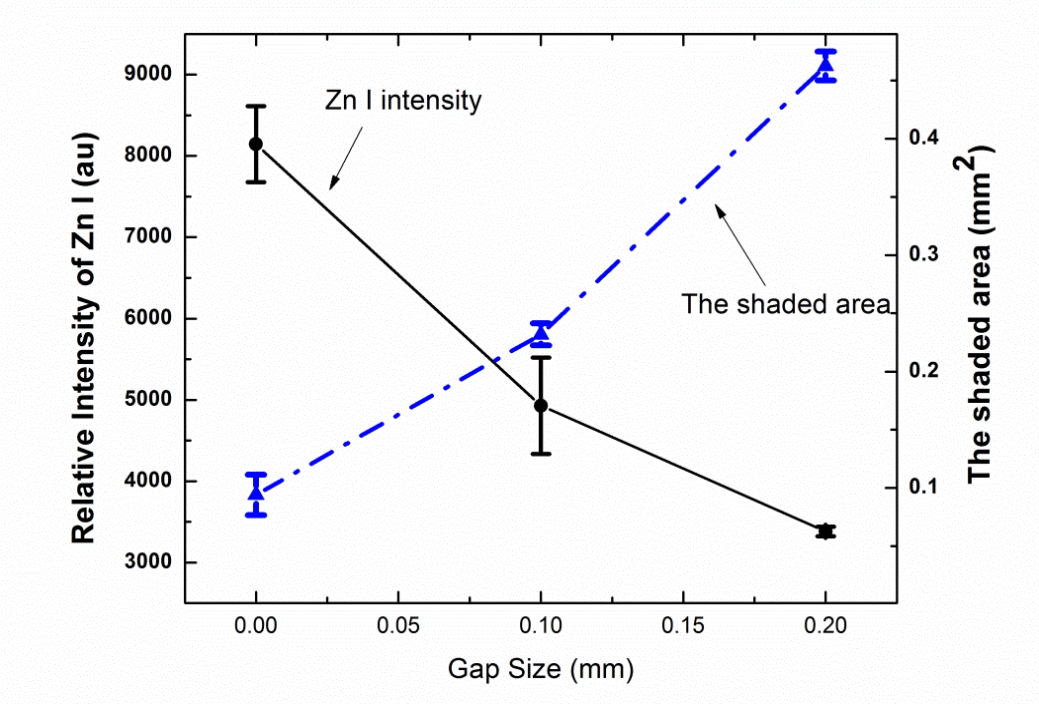

Figure 2-6 Correlation between the intensity of the zinc emission line (481.1nm) and the underfill defect.

Figure **2-6** depicts a correlation between the intensity of the zinc emission line (481.1nm) and the underfill defect. In order to quantify the amount of the underfill, the area of the dropped material is calculated in no-gap, 0.1 mm gap and 0.2 mm gap conditions, respectively, because the dropped material is identical to the amount of the underfill as described above. As the gap between the zinc coated steel sheets increased, the amount of

the underfill almost linearly increased. However, in the corresponding positions, the mean of spectral intensity is inversely decreased. In the cases of no-gap and 0.1 mm gap, the variation of the Zn I intensity is quite large compared with the 0.2 mm gap case, as shown in the error bars of the graph. This indicates that the fluctuation of the vaporized zinc increased in the large gap conditions. That is, as described above the vapor phase of the zinc explosively oscillates inside the liquid iron. Therefore, the small gap opens a pathway for ventilation of the zinc vapor. As a result, in the 0.2 mm gap, the more vaporized zinc can escape away from the zone than that in lower gaps. Additionally, this phenomenon is related to the keyhole plasma location. In the range of the 0.1 mm and 0.2 mm gap, the core part of the plasma is located in a different region because of the different gap conditions. Therefore, the monitoring location of the plasma, which has different densities spatially, is changed, since the collimating lens that detects the plasma is fixed. For this reason, the intensity decreases as the gap increases.

2.3.2.3. Burn-through

Burn-through is studied as the third defect. In principle, excessive heat input causes burn-through, which indicates the removal of the over-melted material generated before the solidification of the molten material. Therefore, this type of defect is observed because of irregular or higher laser power during the process, compared with that of the optimized conditions. Thus, the high power condition and low laser scanning speed provided by Toyota were used to simulate the burn-through in no-gap condition. Figure **2-7** shows the generated burn-through combined with the evolution of the spectral line. The standard deviation of the Zn I line is sharply reduced in the area of the burn-through. The standard

deviation is 511 in the hole 1, corresponding to the first burn-through. In contrast, the standard deviation of the Zn I line is increased up to 1238 between the hole 1 and the hole 2. This result is similar with the features in the bead separation case because the entrapped zinc vapor can escape away through the holes. The only difference between two defects is the range of the mean value in the evolution of the Zn I intensity.

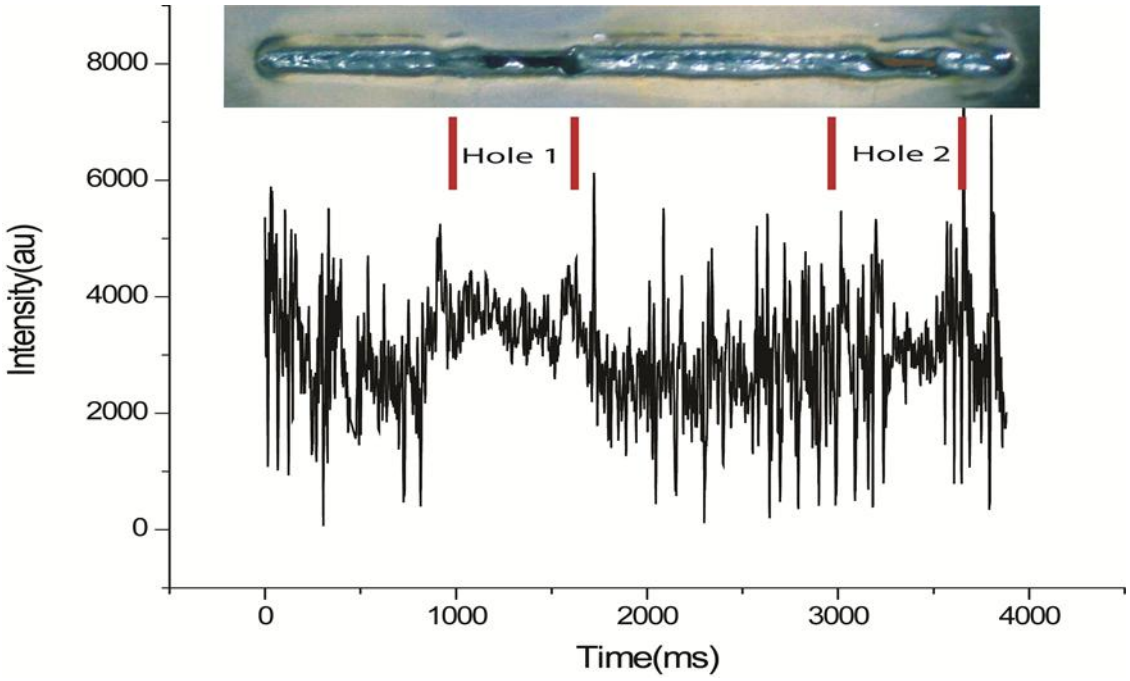

Figure 2-7 Correlation the weld quality with the spectral signal in burn-through defect

2.3.2.4. Electron Temperature Calculation

In the burn-through case, however, the electron temperature of the laser induced plasma shows a dissimilar feature, unlike that of previous defects, because the excessive heat input during the process causes burn-through. In order to calculate the electron

temperature, the Boltzmann plot rather than the Boltzmann two line method is selected for improving accuracy because this plot calculates the temperature from the fitting of the multiple emission lines of the observed species rather than only two lines [35, 36]. The electron temperature calculated from the Zn I lines is used to monitor the burn-through. The Boltzmann plot method is expressed as follows [37]:

$$\ln\frac{I_{mn}\lambda_{mn}}{A_{mn}g_m} = \ln\left(\frac{Nhc}{Z}\right) - \frac{E}{kT} \quad (2.2)$$

where m is excited level, n is lower state level, λ_{mn} is wavelength, A_{mn} is transition probability, and g_m is degeneracy of the excited level. Z, E_m, k, T, and h are the partition function, upper state energy level, the Boltzmann constant, excited temperature, and the Planck's constant, respectively. The spectroscopic parameters of the Zn I emission lines are used for the calculation, as shown in Table **2-1**.

As shown in Figure 2-8, the calculated electron temperature in the burn-through case is much higher than those of the normal condition. In the burn-through case, the electron temperature is ~9400 K. This is a 1700K differnece from the latter case. This indicates that the irregular or excessive heat input significantly induces variation of the electron temperature. Therefore, the temperature can be the guideline for monitoring the burn-through defects. Consequently, the burn-through defects using two features, the evolution of the Zn I intensity and the electron temperature, are detected.

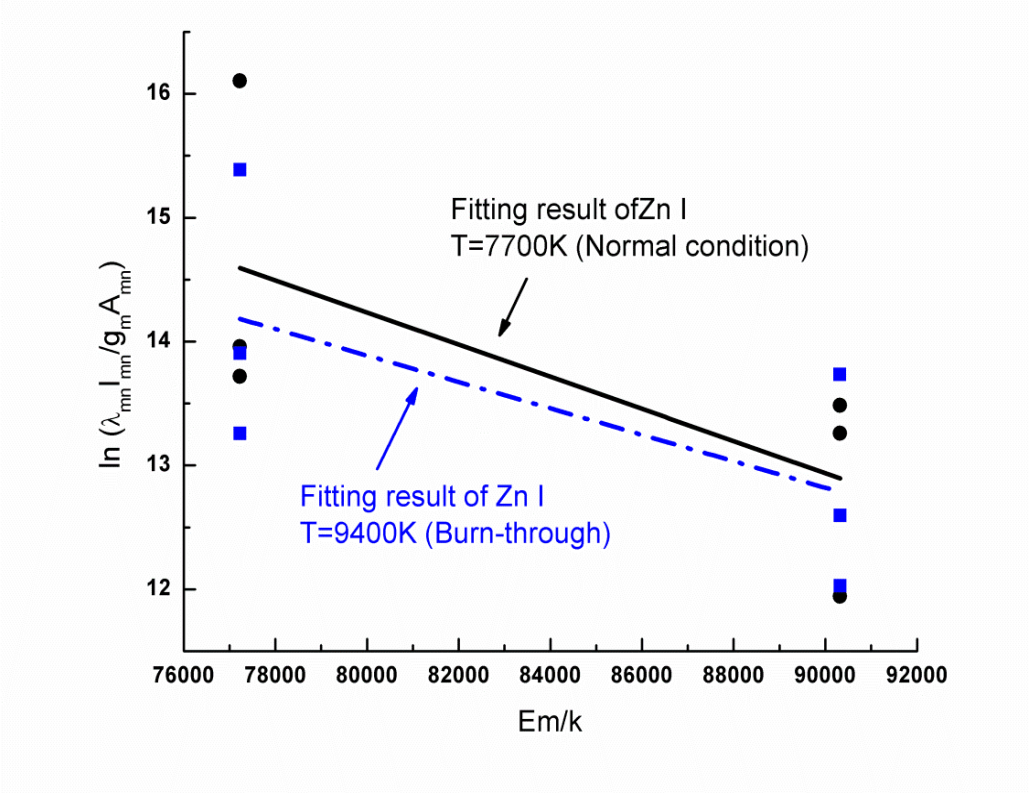

Figure 2-8. Boltzmann plot for the electron temperature estimation based on zinc emission lines.

2.3.2.5. Pin-hole

The contour formed by the Zn I emission line is used to detect the pin-hole defects which result in the difficulty of appearance processing and the weakness of joining strength. These pin-hole defects are small holes or grooves, located in the surface of the welded seam. These defects are related with spatters induced by the liquid metal, resulting from the high velocity of the molten pool, because the spatters indicate the loss of the molten pool that have to be re-solidified to form the seam.

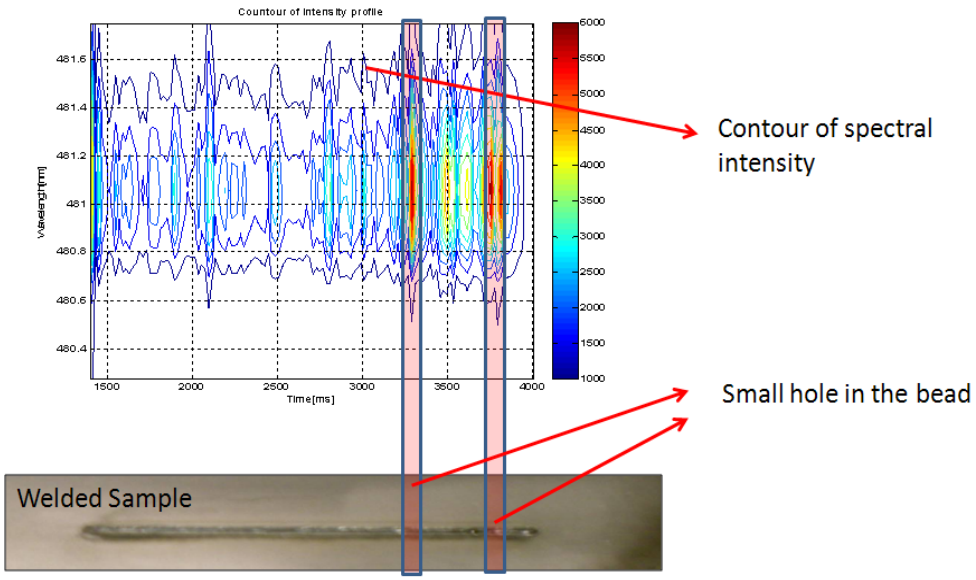

Figure 2-9 Pin-hole defects correlated with the contour formed by the Zn I line (481.1nm)

Figure **2-9** shows the pin-hole defects correlated with the contour formed by the Zn I emission line (481.1nm). These contours are formed by the broadened emission lines in the range of ~481.08 nm to ~481.6 nm. As shown Figure **2-9**, in the ~3.25 sec and ~3.75 sec, the pin-hole defects exist. In the corresponding positions, the spectral intensities are higher than those in other time steps during the process. Additionally, the broadened line widths in the positions are much higher (~1 nm full width at minimum) than those (~0.6 nm full width at minimum) in other temporal evolution. These indicate that when the pin-holes are formed, the spatters are simultaneously formed. The spatters result from the high velocities of the molten flow accelerated by the zinc vaporization. Therefore, when the spatters are jumped out of the molten pool, the behavior of the particles in the plasma is affected. Consequently, the widths of the line emissions are changed by this reason.

2.4. Conclusion

The important findings of this study are summarized below.

1. Several weld defects that frequently occur in realistic production lines (Toyota) were successfully monitored using the optical emission spectroscopy. For the first time, the defects generated in the lap joint welding of multi-zinc coated steels were detected using the OES. Due to the difference of the atomic properties such as the transition probability, the zinc emission lines were clearly observed during the welding process. Because of the relative high transition probability and intensity of the zinc emission lines, the Zn I line (481.1nm) was selected as a monitoring target. The evolution of the Zn I line was correlated with the weld defects, specifically, bead separation, underfill, burn-through, and pin-hote.

2. The bead separation defect, which is one of the most serious defects, was successfully detected in the sheet metal welding. The bead separation began to occur between 0.3 mm and 0.5 mm gap conditions, which were ~35% of the thickness of the steel plate. The standard deviation of the zinc line was sharply reduced from 304 to 94 near the failure point. The standard deviation was the most evident feature in determining the bead separation defect.

3. The underfill defect was detected. In the underfill defect, as the amount of underfill increased, the intensity of the Zn I line decreased. The core region of the plasma was found to be located in a different region because of the different gap conditions. As a result, the

mean of the Zn I intensity changed since the collimating lens that detected the plasma was fixed. For this reason, the intensity decreased as the gap increased.

4. The burn-through defect was detected. The electron temperature was calculated to measure the variation of the heat input controlled by the laser power and the scanning speed. The electron temperature in the condition for simulating the burn-through defect was found to be 9400K. Additionally, the decreased standard deviation of the Zn I intensity was an additional factor in monitoring of the burn-through defect.

5. The pin-hole defects were detected. These defects were related with the spatters of the liquid metal, resulting from the high velocity of the molten pool. The contour formed by the zinc emission line was used to detect the defects. When the spatters were jumped out of the molten pool, the behavior of the particles in the plasma was affected. Consequently, the widths of the contour formed by the emission line were found to be changed from ~0.6 nm to ~1 nm by this reason.

6. As a result, the observation of the zinc emission lines using the OES was found to be efficient for monitoring and understanding the phenomena generated in the zinc coated steel welding, compared with the use of photodiodes.

CHAPTER 3

DEFECT DETECTIONS IN THE DISK LASER MATERIAL PROCESSING USING SUPPORT VECTOR MACHINE

As described in the previous chapter, using the OES, the emission line of the specific constituent has been successfully used for the defect detection in the CO_2 laser welding. In this chapter, the defect detection in disk laser welding will be discussed.

3.1. Introduction

In the disk laser welding of the zinc coated steel, there is an issue in defect detection compared with the previous case. The spectral line of our interest, which was used for the quality monitoring, has not been observed in the disk laser induced plasma. Specifically, the Zn I emission lines induced by the CO_2 laser were not observed in the disk laser induced plasma. This difference results from different energy absorptions, since the different energy absorption by the laser induced plasma causes different optical emission profiles on the same target materials. Fundamentally, the absorption mechanism is governed by different Inverse Bremsstrahlung (IB) absorption, which is related with the laser beam wavelengths: 10.6 μm for the CO_2 laser and 1.03 μm for the disk laser [35, 36, 38]. This IB absorption will be discussed in Chapter 5 later and omitted here. As a result,

the difference of the laser beam wavelengths between the CO_2 laser and disk laser causes the different optical emission profiles on the same target materials. For this reason, the zinc emission line used for detect detections in the CO_2 welding was missing in the disk laser induced plasma. Therefore, an alternative way is required to overcome this limitation for the defect detection in the disk laser welding processes.

A statistical approach is combined with the OES method to solve the problem, since the spectral information, the acquired signals by the spectrometer, is rich enough to employ the statistical approach. The richness of available data is a major benefit in the use of the optical emission spectroscopy for the quality monitoring of the laser welding, compared with the use of photodiode. In other words, while the photodiode converts the certain band of the optical emission induced by the plasma into one electrical voltage or current, the spectrometer keeps the information of the several emission lines generated within the optical band. This difference indicates that the spectral features of the defect-present case in the OES method are more discriminative than those in the conventional quality monitoring method. Therefore, the rich input data enable better performances for the defect detection. The performances will be discussed later.

In this chapter, the reason of the different spectra between the disk laser and the CO_2 laser are investigated through the electron temperature calculations. Next, the welding defects generated in the disk laser welding are detected and classified by using a Support Vector Machine (SVM), a machine learning algorithm. Theses classifications give useful information to operators in production lines, because they can recognize the existing problems depending on the type of defects and further the recognition can directly lead to

feedback control of the defects in the production lines. All defects are simulated with the realistic experimental conditions requested by Toyota.

3.2. Experimental Set-up

Figure **3-1** shows a schematic of the experimental set up, consisting of a disk laser, target materials, and a spectrometer. A disk laser (HLD 4002) manufactured by Trumph is used to perform welding experiments. This laser is connected with Anorad motion controller. A concentric nozzle with focal length of 20 mm is connected with a optical fiber which delivers laser beam. Beam mode is top hat mode and the beam diameter is 280 μm at the focal position. The position of the laser was fixed and the motion stage was moved for the welding. The experimental conditions are 1.2 kW (laser power), 60 inch per min (welding speed), 40 standard cubic foot per hour (shielding gas flow rate). Argon gas is used for shielding welding zone.

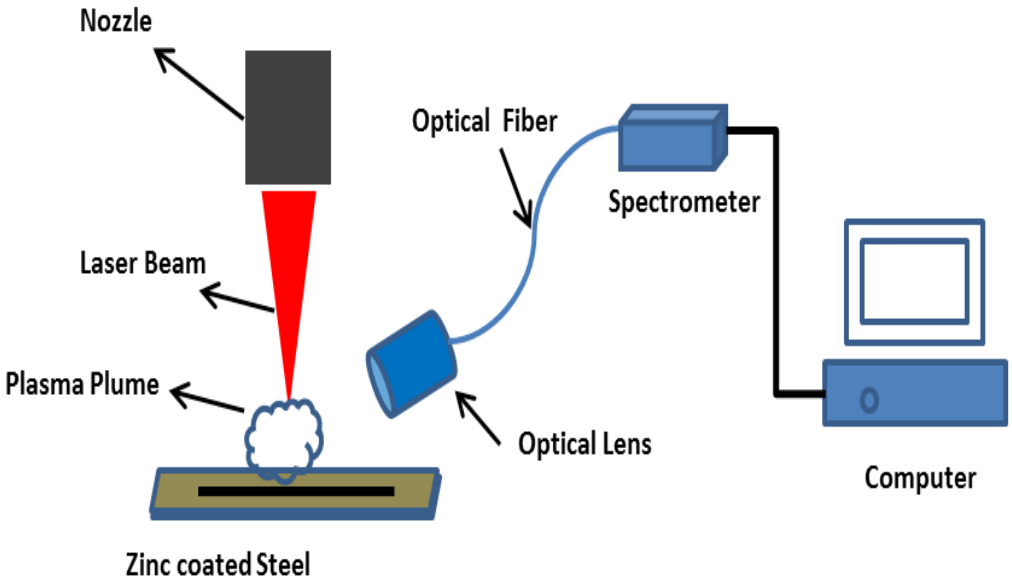

Figure 3-1 A schematic of experimental set up

Spectral signal of the plasma induced by the disk laser is collected by a spectrometer (Ocean-optics HR2000+). The resolution of the spectrometer was 0.1 nm. As shown in Figure **3-1**, the emission lights are collected by a collimating lens and then delivered through optical fibers of 50 μm and 1 mm diameter. The 1 mm optical fiber was used to magnify the optical signals because the disk-laser induced-plasma generated weak emission lines, compared with those of the CO_2 laser induced plasma that was collected by the 50 μm fiber. A detectable spectral range is from 339.03 nm to 434.1 nm. The collimating lens was placed transversely to the welding direction.

Zinc coated steels which were supplied by Toyota were used for this study. The dimension of these sheet metals is 0.8 mm thick, 0.5 cm wide and 1 cm long. Two sheet metals are overlapped and clamped by a holding jig. In order to simulate the defects specified by Toyota, different thickness spacers from 0. 1 mm to 0.5 mm have been inserted at both ends in longitudinal direction. The focal position was set to the top surface of the upper zinc coated steel.

3.3. Spectra in the Disk Laser Welding

As an initial step, the optical emission spectrum of the plasma was measured during the disk laser welding on the zinc-coated steels. Because of the short wavelength of this disk laser (1.03 μm), compared to that of the CO_2 laser (10.6 μm), the emission spectrum profile was quite different, as shown in Figure **3-2** [39].

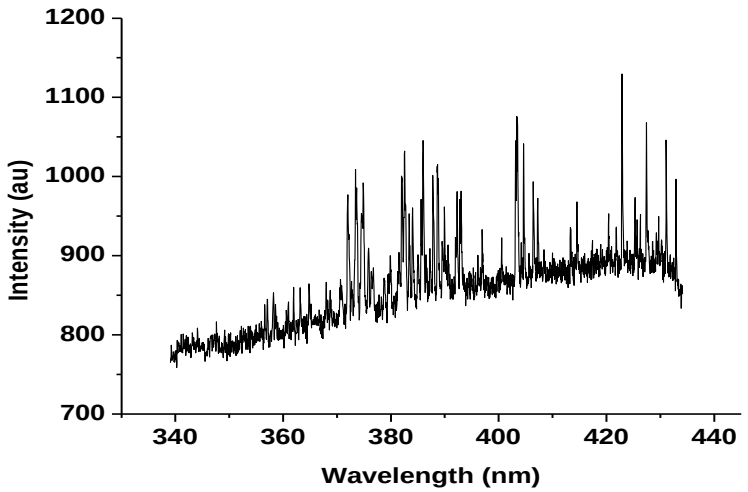

Figure 3-2 Spectrum acquired from the plasma induced by the disk laser welding on the zinc coated steel

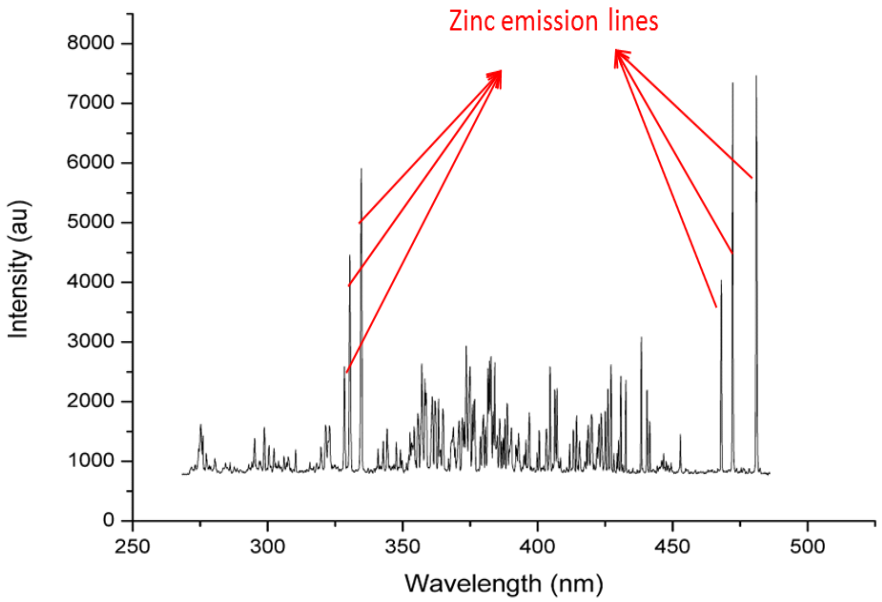

Figure 3-3 Spectrum acquired from the plasma induced by the CO_2 laser welding on the zinc coated steel

As shown in Figure 3-3, the emission spectrum generated in the CO_2 laser welding on the zinc coated steels was depicted to compare that in disk laser. When the broadband spectrometer with a low resolution was adopted, the observed spectrum in the disk laser welding was weak, compared with that in the CO_2 laser welding. For the clear observation of the spectra, the high resolution spectrometer described in the experimental section was used with the 1 mm optical fiber for the spectra.

As shown in Figure 3-2, few atomic emission lines were observed, compared with those in Figure 3-3. Moreover, the observed zinc emission lines, evident in the CO_2 laser welding, were not observed in the disk laser welding case. This different profile results from the different absorption of laser beam energy by the plasma. Fundamentally, the energy absorption by the plasma is mainly induced by absorption mechanisms: either Inverse Bremsstrahlung (IB) absorption or Photo-Ionization (PI) process [35]. Because the effect of the PI process is negligible in infra-red lasers including the two lasers (10.6 μm and 1.03 μm) used in this study, the IB absorption plays a dominant role in the energy absorption of laser [35]. This IB absorption is proportional to $\boldsymbol{\lambda^3}$, where λ is the laser wavelength [40, 41]. In order to compare the amounts of absorptions between two plasmas, the electron temperatures which show the degree of the absorption were calculated in the two cases.

Prior to the electron temperature calculations, the spectroscopic properties of the emission lines were identified using NIST atomic and CFA data base [28, 29]. The emission lines in Figure 3-2 are found to be mostly Fe I lines. The properties of the Fe I lines are summarized in Table 3-1. For the electron temperature calculation, the Boltzmann plot method is employed [37]:

$$\ln\left(\frac{I_{mn}\lambda_{mn}}{A_{mn}g_m}\right) = \ln\left(\frac{Nhc}{Z}\right) - \frac{E_m}{kT} \quad (3.\ 1)$$

where m is the excited state level, n is the lower state level, λ_{mn} is the wavelength, A_{mn} is the transition probability, and g_m is the degeneracy of the excited level. Z, E_m, k, T, and h are the partition function, upper state energy level, Boltzmann constant, excited temperature, and Planck's constant, respectively. Figure **3-4** shows the fitting result for the temperature calculation. As a result, the electron temperature of the plasma induced by the disk laser is ~4400 K. In contrast, the electron temperature in the CO_2 laser welding case is ~7700 K as depicted in Figure 2-8 . These temperatures explain the different profiles of two spectra. Fundamentally, the emission line arises from energy gap between the excited and the ground levels in the transition for a two-level atom. The energy gap required for the transition is induced by the kinetic energy of the electron, $\frac{1}{2}mv^2$. The calculated temperatures above explain the amount of the kinetic energy generated by the energy absorption of the plasma. Therefore, the different electron temperatures induce the different energy distribution between the collisional particles. For this reason, the spectrum shows dissimilar profile.

Table 3-1.Spectroscopic properties of Fe I lines found in the plasma induced by the disk laser

Wavelength[nm]	Transition Probability[s^{-1}]	Lower Energy Level [cm^{-1}]	Upper Energy Level [cm^{-1}]
372.0	1.62×10^{7}	0	26875
374.6	1.15×10^{7}	704	27395
375.8	6.34×10^{7}	7728	34329
382.0	6.68×10^{7}	6928	33096
388.6	5.30×10^{6}	416	26140
403.0	2.90×10^{5}	17727	42533
403.1	1.60×10^{5}	24336	49135
406.4	6.80×10^{7}	12561	37163
407.2	7.65×10^{7}	12969	37521

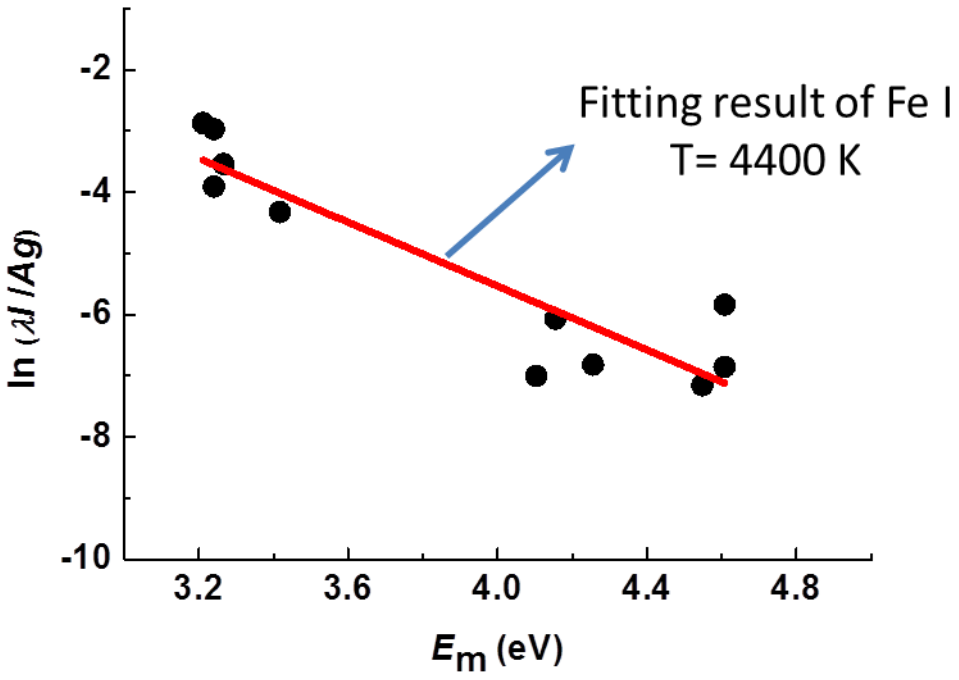

Figure 3-4 Boltzmann plot for the electron temperature estimation based on Fe I emission lines observed in the disk laser welding.

3.4. Classification of Defects using Support Vector Machine

In the Chapter II, for the quality monitoring of the zinc coated steel welding, the Zn I emission line was used to detect defects by tracking the zinc behavior in the laser-material interaction-zone. As discussed in the previous section, however, the spectral line of our interest, which was used for the quality monitoring, has not been observed in the disk laser induced plasma. That is, the Zn I emission lines induced by the CO_2 laser were not observed in the disk laser induced plasma.

To overcome this limitation, a statistical approach is combined with the OES method, since the spectral information acquired by the spectrometer is enough rich to employ the statistical approach. The richness of the available data is a major benefit in the use of the optical emission spectroscopy for the quality monitoring of the laser welding, compared with the use of the conventional monitoring methods.

3.4.1. Support Vector Machine (SVM)

Machine learning is one of the branches in artificial intelligence. The machine algorithms learn features which exist in empirical data or acquired signals from experiments. Then, the algorithms convert the learned features into values which will be used to predict or classify new data sets [42, 43]. Figure 3-5 shows basic classification scheme, which consists of three steps, sampling, feature extraction and classification [24]. In these three steps, the feature extraction is a core part in the classification process, since the evident features of the data sets determine the performance of these statistical approaches. Therefore, if the features are well-extracted from the training data sets, these

algorithms can detect or classify incoming new signals for real-time control of the processes.

Figure 3-5 Basic classification scheme [24]

Among several machine learning algorithms, the Support Vector Machine (SVM) is selected for this study due to its many advantages. For example, this SVM is proper for the classification of detects because it was originally invented to generate maximal margin between separable data sets [44, 45]. Furthermore, in the SVM, parameter tunings can be easily performed for a fast and efficient process. This SVM also has good generalization ability, because the SVM maximizes the distance between the boundary of the each class as shown in Figure 3-6 [44, 46, 47] .

The SVM aims to find the separating hyperplane which splits the input data into several regions corresponding to the classes [44]. The classification of each class are performed based on the equations below [44]:

$$\mathbf{w}^t\mathbf{x}_j + \mathbf{b} \geq \mathbf{1}, \mathbf{if}\ y_j = +\mathbf{1} \tag{3. 2}$$

$$\mathbf{w}^t\mathbf{x}_j + \mathbf{b} \leq -\mathbf{1}, \mathbf{if}\ y_j = -\mathbf{1}$$

where $\mathbf{x}_j$ is the column vector representing the training data (spectral data in this study), j is the number of the training data, t indicate transpose of the vector, and y_j indicates the class label. As shown in Figure 3-6, if the trained models, **w** and b, which satisfy the above two equations, exist, the training data is said to *be linearly separable* by the hyperplane $\mathbf{w}^t\mathbf{x}_j + \mathbf{b} = \mathbf{0}$ [44]**.** These two equations can be expressed as one inequality:

$$[y_i(\mathbf{w}^t\mathbf{x}_j + \mathbf{b}) - \mathbf{1}] \geq \mathbf{0} \qquad (3.\ 3)$$

Therefore, the margin between the classes can be expressed 2/ ‖ **w** ‖. The maximal margin is generated when the norm ‖ **w** ‖ is minimized along satisfying the equation 3.3.

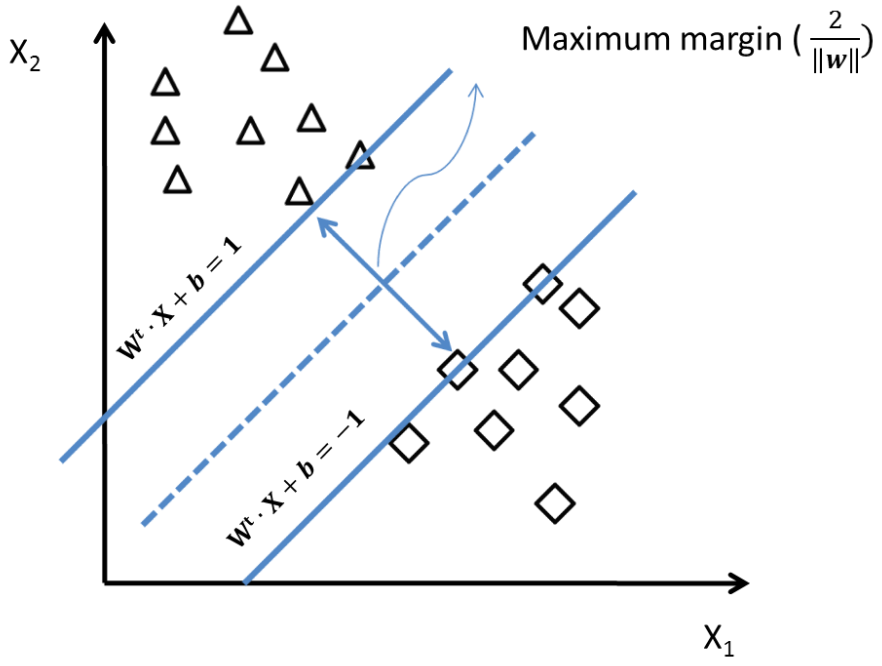

Figure 3-6 Schematic showing the concept of binary classification in Support Vector Machine

As a result form , the C-support vector machine, a standard form of SVM, is expressed as follows [46]:

$$\underset{w,b,\zeta}{\text{Min}} \ \frac{1}{2}\mathbf{w}^{T}\mathbf{w} + \ \mathbf{C}\sum_{i=1}^{l}\boldsymbol{\xi}_{i}$$

$$\text{Subject to } \ \boldsymbol{y}_{i}(\mathbf{w}^{T}\boldsymbol{\phi}(\mathbf{x}_{i}) + \boldsymbol{b}) \geq \mathbf{1} - \boldsymbol{\xi}_{i} \qquad (3.4)$$

$$\boldsymbol{\xi}_{i} \geq \mathbf{0}, \boldsymbol{i} = \mathbf{1}, \ldots\ldots, \boldsymbol{l}.$$

where, ξ_i is slack variable, C is a balancing factor and $\phi(\mathbf{x}_i)$ is the feature function which maps the training vector $\mathbf{x}_i$ into higher dimension. In this study, the linear kernel function is used because the use of the linear kernel produce high classification rate.

3.4.2. Feature Extraction in Each Defect

In this section, welding defects are detected and classified using the SVM. As explained above, this algorithm first learns the features of the spectral data that are correlated with the weld defects. Then, the SVM generates support vectors which are used to define the maximum margin between classes, as shown in Figure 3-6. Based on the learning results, when there are new spectral data, the SVM classifies the data sets into several desired classes such as no-gap condition, underfill defect and bead separation defects. Therefore, the features of the experimental data are important to classify the defects.

As a first step, the features of the spectral data recorded in the defect- present cases are extracted. Even though the Zn I emission lines are not observed in the plasma of the disk laser welding, the effects of the vaporized zinc, which is similar in the CO_2 laser

welding of the zinc coated steels, still remains inside the welding zone. In order to extract these features, similar experiments for the simulation of the defects were repeated.

As described in the previous Chapter II, the bead separation defects occurred from the 0.3 mm gap condition, and the underfill defects were generated in the range of 0.1 mm - 0.2 mm gap. The 0.2 mm spacers and 0.3 mm spacers were put at both ends to confirm whether the spectral signal behavior shows the same trend in the defect-present conditions. As shown in Figure **3-7**, the transitional behavior generated between the bead separation and underfill defect is correlated with the Fe I emission lines. The Fe I 375.8 nm is selected, because the emission line shows clear variation during the experiments. This evident variation is owing to its high transition probability compared with those of other Fe I emission lines found in the plasma induced by the disk laser. In the transition zone between underfill and bead separation, the average spectral intensity changes from 800 to 777, and the standard deviation changes from 12 to 8. This result is consistent with the result of the CO_2 laser welding because the standard deviation is larger in lower gap conditions due to the severe fluctuations. The only difference between the CO_2 laser welding and the disk laser welding is the sensitivity of the signal. The amount of the change in the Fe emission lines is not as much as that of the Zn emission lines observed in the CO_2 laser welding.

Even though the sensitivity of the signal observed in the disk laser welding is not as large as the CO_2 laser welding, some features are still apparent in the transitional behaviors. Our purpose is to find the features which the spectral data in each defect case display. Several experiments individually have been performed to find the features in each condition. The experiments are divided into three classes such as no-gap condition,

underfill, and bead separation, since those defects are realistic concerns for the production lines.

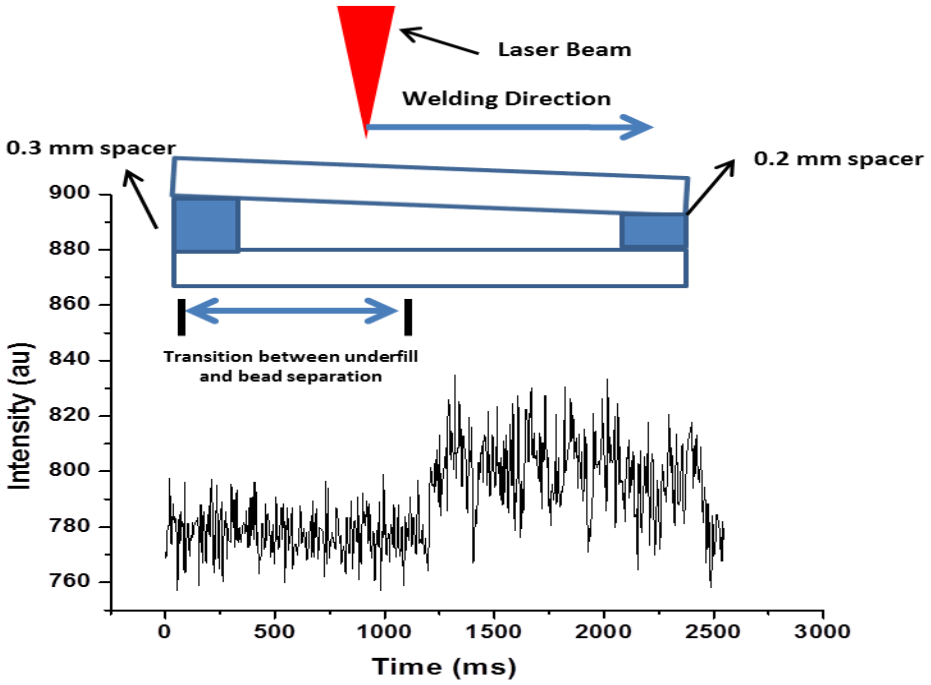

Figure 3-7 Temporal evolution of the Fe I emission line between the underfill defect and the bead separation defect

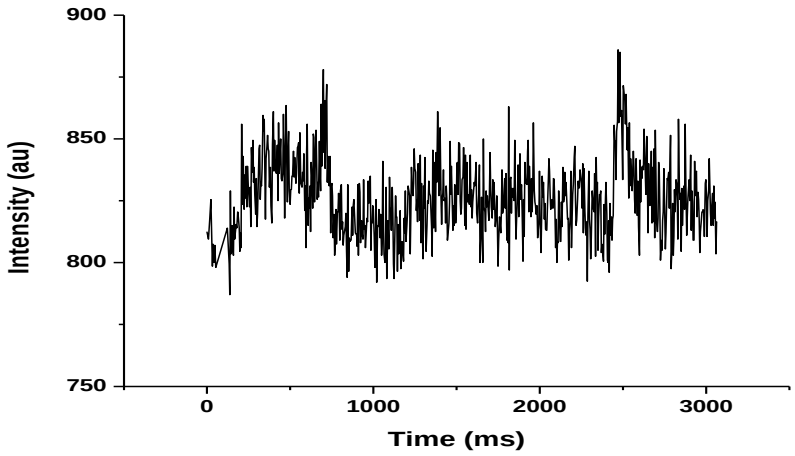

Figure 3-8 Temporal evolution of the iron emission line, 375.8 nm in the no-gap condition

For the no-gap case, as shown in Figure **3-8**, the temporal evolution of the Fe I 375.8 nm is unstable. As described in the Chapter II, the signal in no-gap case was randomly fluctuated, since the vaporized zinc was oscillated inside the laser-material interaction-zone. In the disk laser welding, similar behavior exists in the laser-material interaction-zone. In other words, the vaporized zinc induces similar behavior for the Fe particles that forms the plasma, since the particles of Zn and Fe stay together inside the plasma. Note that the absence of the Zn emission lines does not indicate the absence of the Zn particles inside the plasma. However, not all Fe emission lines clearly show this behavior. Few Fe spectral lines show similar behavior. As a result, in the disk laser welding, the average intensity of the line is 815 and the standard deviation of the line is 24.

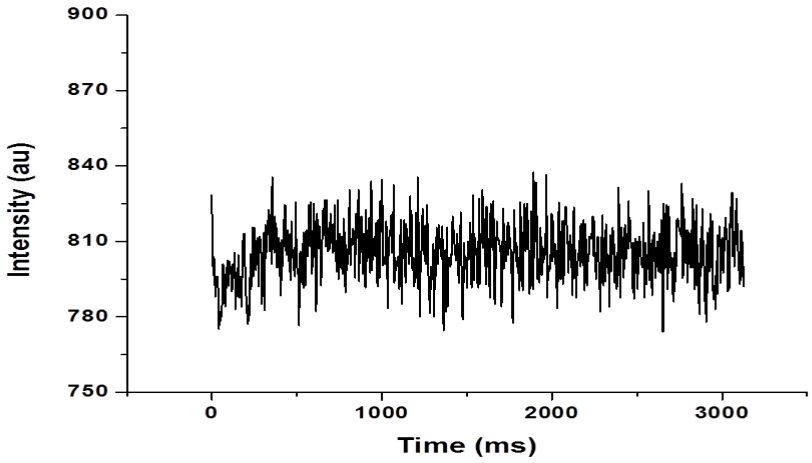

Figure 3-9. Temporal evolution of the iron emission line, 375.8nm in underfill condition

As illustrated in Figure **3-9**, the Fe I line shows a relatively stable evolution profile for the underfill defect in the case of 0.1 mm spacer. The Fe I line has weaker intensity, 806, than the intensity of the no-gap case. The standard deviation is decreased to 11.5, compared with that of the no-gap case. This explains that the vaporized zinc, which causes instability

in welding zone, escapes away through the gap. In such a way, the features, the average intensity and standard deviation of the Fe I emission lines are collected in each condition.

3.4.3. Spectra Data Reduction and Formation of Training Sets

As described above, two features, the average intensity and the standard deviation of the Fe I emission lines, are extracted through the series of the experiments conducted on the same experimental conditions in each defect case. Our purpose is to find the hyperplane that separates the input data into the desired classes, using these features. One advantage in the use of the OES for the quality monitoring is that the input features are rich compared with the conventional OE method, because the OES can resolve the constituents of the target material. Therefore, several emission lines of the specific constituent can be used to form training sets. As explained by equation (3.3), the **w** and b are calculated to define the hyperplane using the training sets.

Figure **3-10** shows the structure of the raw spectra data (left) and the extracted spectra data (right) which contain features in each defect. The raw data consist of 2048 spectra in each sampling time. The 2048 spectra are too huge to use for the analysis. Moreover, only a few spectra are useful among the whole spectra, since each spectrum generation depends on several factors, such as target material constituents and laser types. Therefore, the reduction of the data size should be accompanied by spectrum analysis. As illustrated in the figure, each $\mathbf{x}_i$ is a column vector that includes the extracted features in each class of our interests, such as no-gap, underfill, and bead separation. Among the whole spectra, nine emission lines are extracted for the analysis. These emission lines have relatively high intensity and transition probability. All these lines are Fe I lines. Therefore,

the each $\mathbf{x}_i$ is a column vector with nine dimensions. Using these training sets consisting of the column vectors, the **w** and b are calculated.

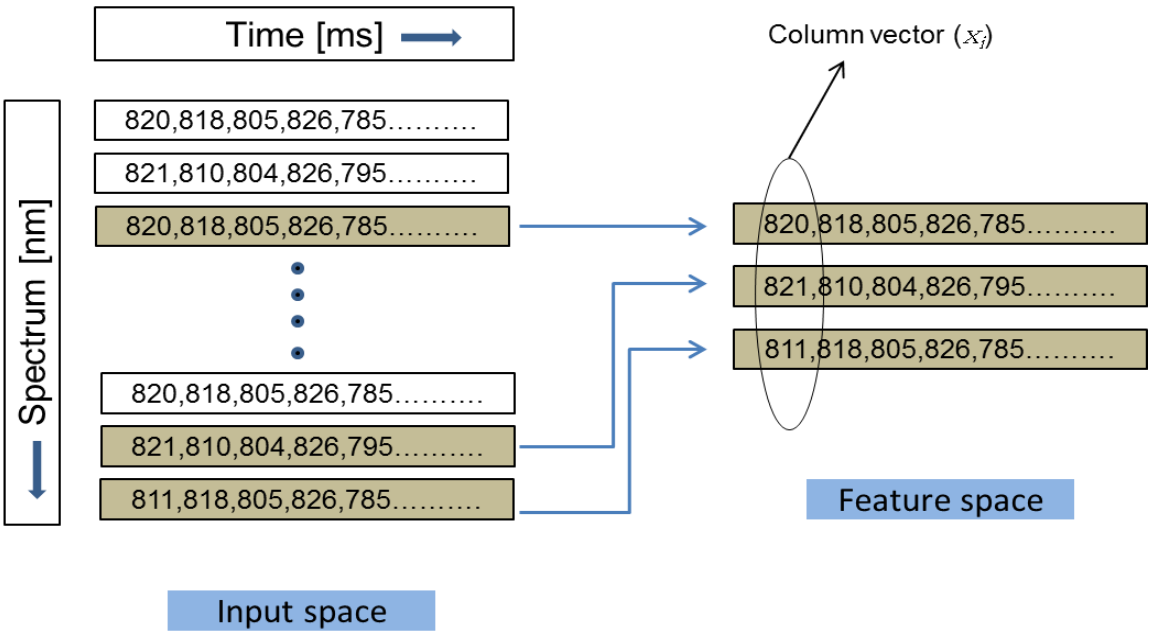

Figure 3-10. The structures of the raw spectral data (left) and the extracted spectral data (right) which have features in each defect.

The experimental results in the disk laser welding show that the spectra data observed in each defect have previously-identified specific range of the average intensities and the standard deviations. Each column vector consists of nine Fe I emission lines. The training sets are generated from the 16 experiments and each training set has 10000 sampling points. As shown in Figure 3-11, the sampling points were extracted in the middle of the welding experiments for the consistency. For this reason, the total sampling points are divided into subsets using a certain size of the time windows, since each sampling point cannot be used individually as training sets, due to the noise and the

uncertainty. In each window, then, the mean of the intensity and the standard deviation of the intensity, are calculated. Therefore, these calculated values can represent the characteristics of the training data sets.

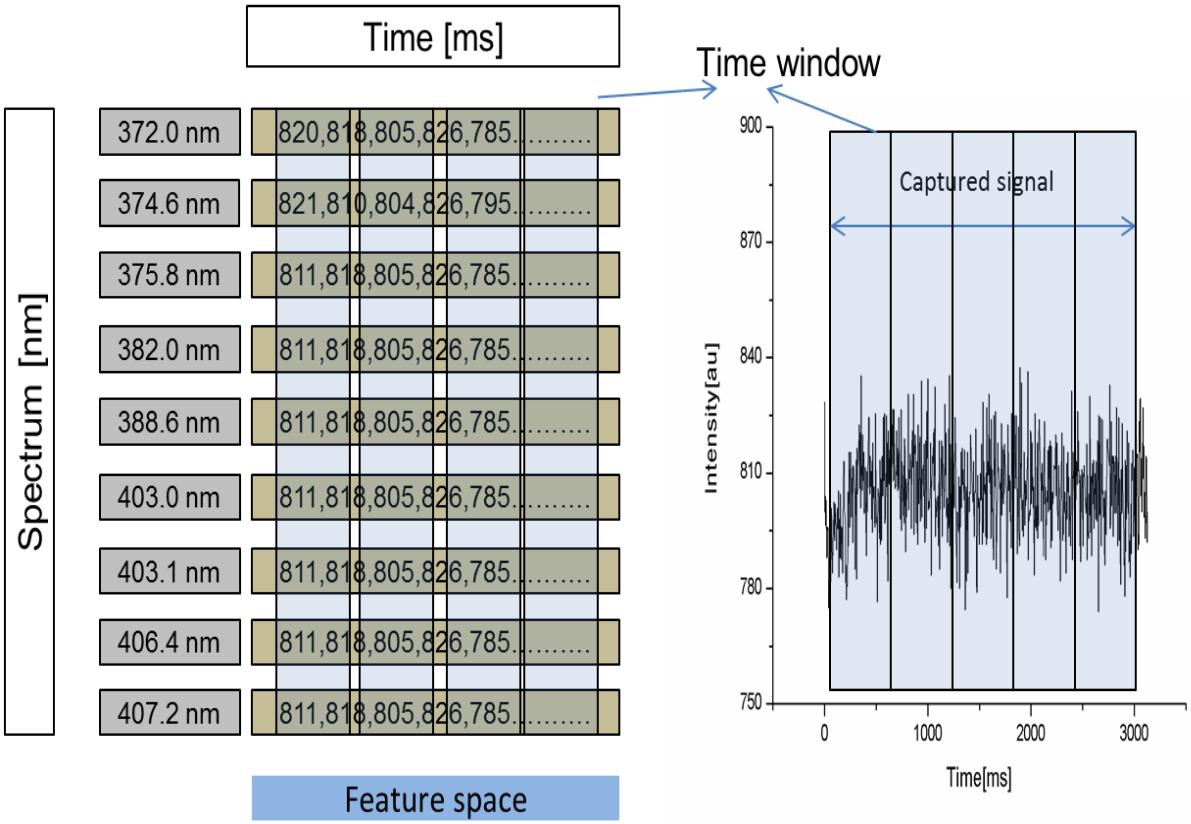

Figure 3-11. A schematic of the data structure of the training data set

3.4.4. Classification Results

For the training of the data, the C-SVM is used because of its easy parameter tuning. The easy tuning reduces the computational cost for the real time monitoring. The SVM was originally invented for the purpose of the binary classification [47]. However,

our purpose is to classify the data into three classes, bead separation, underfill, and no-gap conditions. For the multi-classification problem, one-against-one method is applied to generate larger support vectors that produces better classification performance [47]. Therefore, the binary classifications are performed repeatedly based on the combination between the classes.

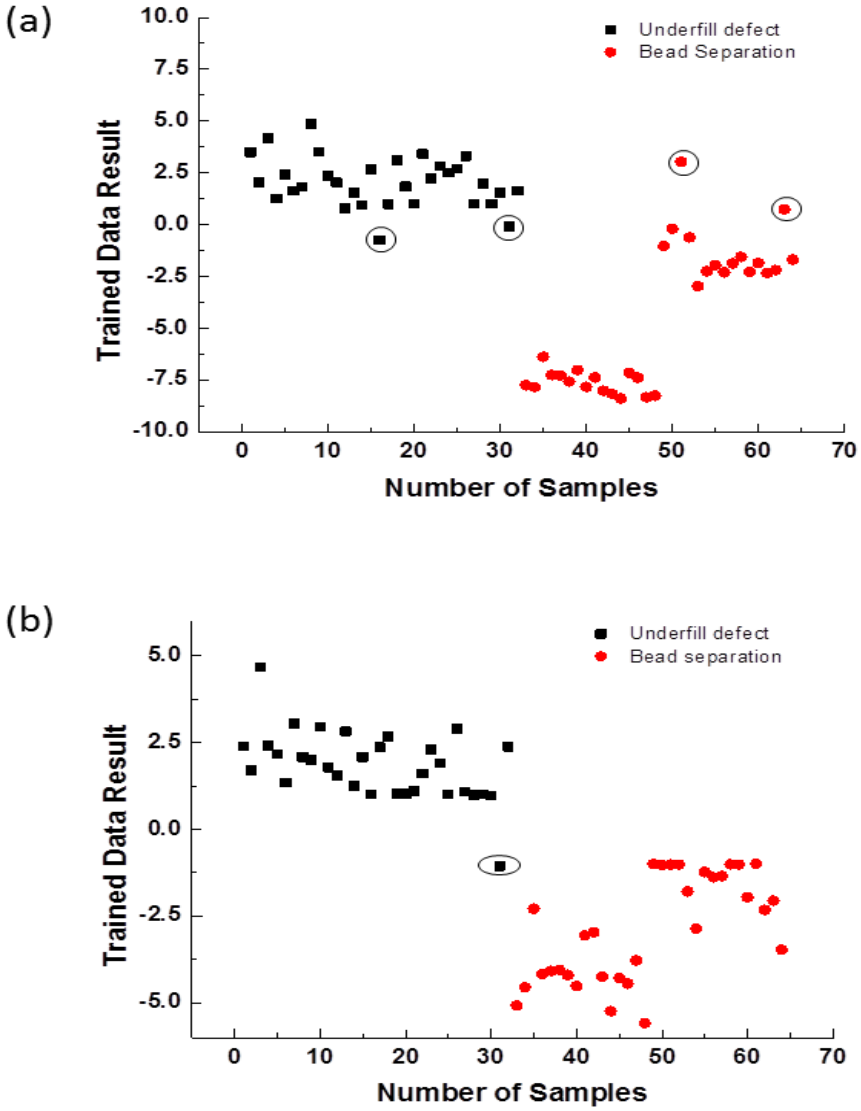

Figure 3-12 The classification results by the hyperplane, $\mathbf{w}^t\mathbf{x}$-b=0, which is defined by the trained values, **w** and b: one dimensional data sets, (a), and nine dimensional data sets, (b).

First, a comparison of the training results between the nine-dimension and the one-dimension training sets is conducted. This comparative study confirms the advantage of the OES for the quality monitoring. As discussed in the previous Chapter II, the described conventional techniques for the quality monitoring are dependent on one dimensional output such as electrical voltage or current. Therefore, even though this SVM could be applied to the acquired signals from the photodiode, one-dimensional training set would be the maximum available training data. Furthermore, the one-dimensional output is insufficient to capture the features in these defect detections. For these reason, this comparative study is performed to show the advantage of the OES indirectly.

Figure **3-12** shows the classification results using the hyperplane, $\mathbf{w}^t\mathbf{x}$-b=0, which is defined by the trained model such as **w** and b: the classification results of the training sets consisting of one-dimensional column vectors, (a), containing the extracted features and nine dimensional column vectors, (b), containing the extracted features. This boundary classifies the defects into two classes, underfill and bead separation. The spectral data of the underfill defect are expressed by the black squares, and the spectral data of the bead separation are expressed by the red circles. Both data sets are classified by the hyperplane by $\mathbf{w}^t\mathbf{x}$-b=0. For this reason, each data set is located above the margin defined at $\mathbf{w}^t\mathbf{x}$-b=1 and below the margin defined at $\mathbf{w}^t\mathbf{x}$-b= -1, respectively. Here, 1 and -1 are the boundary values of the trained data, as expressed in the y-axis. That is, the data sets are classified by the hyperplane, $\mathbf{w}^t\mathbf{x}$-b=0, and the maximum margin is defined between 1 and -1. The case (a) indicates the classification results of the conventional monitoring methods, which indicate one-dimensional data. As shown in the case (a), when the one-dimensional signal is used for the classification, although the hyperplane is reasonably defined, the four data

that circled in black color, fail to be classified. Specifically, the two squares in the underfill data set, which have to be positive values, show negative values, because the underfill defects are classified above the hyperplane defined by $\mathbf{w}^t\mathbf{x}$-b=1. In contrast, as shown in the case (b), when nine-dimensional training sets, only one fails to be classified into the proper class. This difference indicates that the calculated **w** and b in the case (b) are better for generalizing new signals than those in the case (a). In other words, the classifications of the new data are performed by the calculated values, **w** and b, which result from the training sets. Therefore, the well-trained values have better generalization abilities for the classification of the new data sets. Note that the scatter of data within each class does not reduce the classification performance, because the SVM considers only the maximum margin rather than reducing the distance between data points within each class. The overall classification rate will be discussed later.

Figure **3-13** shows the binary classification results of the combination between the classes. As described above, the combinations of the binary classification are required for the multi-classification. Therefore, in each binary classification, several **w** and b are calculated to define the hyperplane. For this reason, three results are plotted: (a) binary classification between no-gap condition (class 1) and underfill defect (class 2), (b) binary classification between underfill defect (class 2) and bead separation (class 3), and (c) binary classification between underfill defect (class 2) and bead separation (class 3). Except for one data point in the case of (c), all **w** and b are well defined from the training sets for each classification. The data points in each class consist of 32 points. Note that this number of data points does not indicate the individual sampling points; each data point is defined from the calculated mean values and standard deviations in the properly defined time window.

Therefore, the number of the data points is sufficient to represent the characteristics of each of features, which were defined earlier.

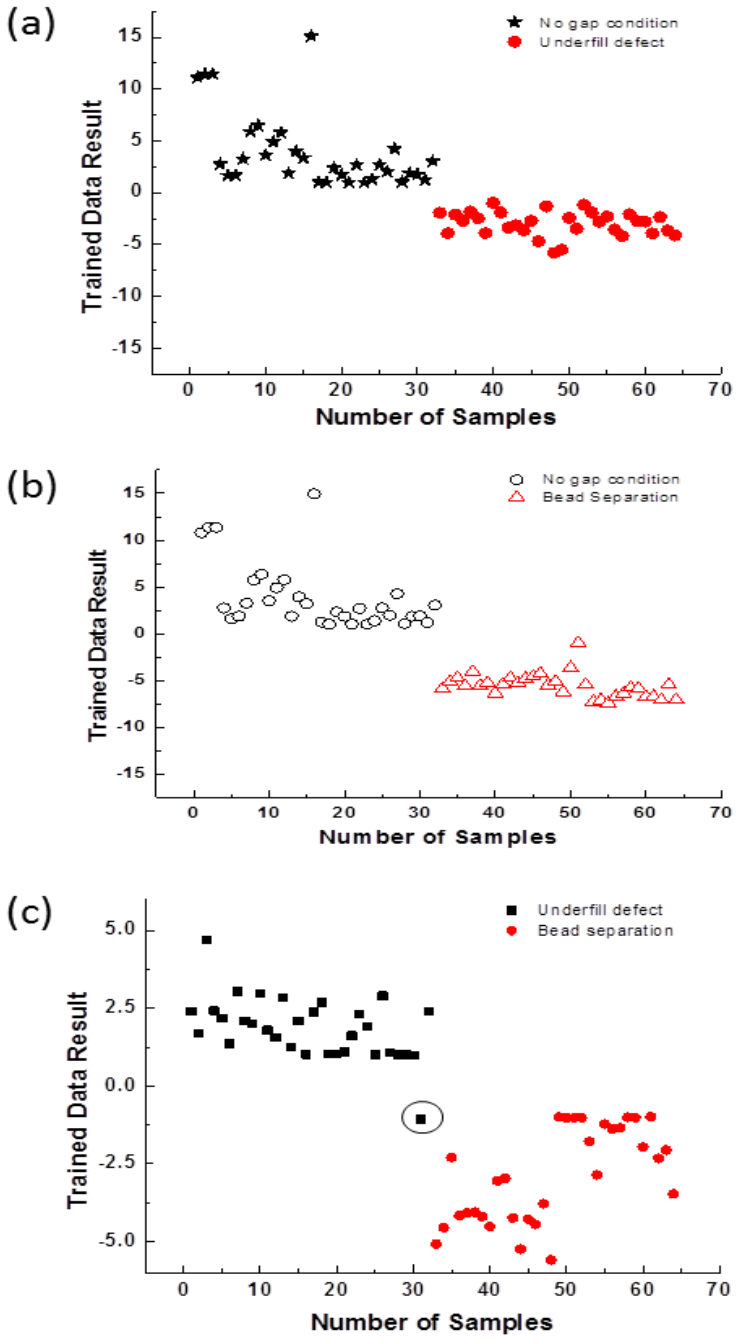

Figure 3-13 Trained results for finding hyperplane $\mathbf{w}^t\mathbf{x}$-b=0 (a) binary classification between no-gap condition (class 1) and underfill defect (class 2), (b) binary classification between underfill defect (class 2) and bead separation (class 3), (c) binary classification between underfill defect (class 2) and bead separation (class 3)

Table 3-2 The confusion matrix for the SVM with two feature subset for three classes multi-classifications.

		Predicted class		
		No Gap	*Underfill*	*Bead Separation*
Actual class	*No Gap*	100 %	0%	0%
	Underfill	0 %	94%	6%
	Bead Separation	0%	9%	91%

Based on the training results above, performance tests of multi-classification are conducted. V-fold cross validation has been used for the tests, since the computational cost is less expensive than that of ordinary cross-validation methods[48]. In the V-fold cross validation, each training data set must be tested after training procedures sequentially to prevent biased results. The trained results are summarized in the confusion matrix, as shown in Table 3-2. The overall classification rate is about 95%. In the table, the actual class indicates the true case of the data set. In the prediction of the no-gap conditions, the classification rate is 100%. The error rates for the defect defections between the class 2 and

3 are higher than others. These errors result from the fact that, in the bead separation area, the signal characteristics are sometimes similar with that of the underfill cases in the certain range. These similar characteristics arise from that the welded seams were randomly joined and separated in the bead separation defects, due to the change of the gap size during the process. In general, the distortion of the sheet metal, induced by the high heat energy from the lasers, sometimes leads to the variation of the gap size. These changes cause partial underfill to be formed in the middle of the welded seam in the lap welding conditions. Therefore, some signals acquired in the bead separation area have range similar to that the acquired signals of the underfill defects have.

Additionally, as compared in Figure **3-12**, the overall classification rate in the use of the one dimensional data is ~90%. This indirectly indicates that the use of the spectral data for the quality monitoring is very efficient compared to the use of one-dimensional feature, since the OES can resolve the material constituents, unlike the conventional monitoring methods.

3.5. Conclusion

In this chapter, the Support Vector Machine, a machine learning algorithm, was applied to overcome the previously-described problem and further to detect the welding defects. In addition, the classification of the several classes, such as no-gap condition, bead separations and underfill defects, was performed to give useful information to the operators in the production line for feedback controls. The important results are summarized as below.

The optical emission of the plasma was measured during the disk laser welding on the zinc-coated steels. Because of the shorter wavelength of this disk laser compared to the

CO_2 laser, the emission spectra profile was quite different. Especially, the observed zinc emission lines in the CO_2 laser welding case were not observed in the disk laser welding case. This difference arises from the different absorptivity of the plasma governed by Inverse Bremsstrahlung (IB) absorption, since the laser wavelength of the CO_2 laser (10.6 μm) and the disk laser (1.03 μm) are different, respectively. As a result, the electron temperature in the CO_2 laser welding and the disk laser welding cases were ~4400 K and ~7700 K, respectively. Consequently, these different kinetic energy distributions of the particles inside the two plasmas are different. For this reason, the characteristics of the spectra change showed dissimilar results.

In the previous chapter, in the laser welding of the zinc coated steels, the Zn emission lines were used for the purpose of the quality monitoring. However, even though the Zn I emission lines were not observed in the plasma of the disk laser welding, the temporal evolution of the Fe emission lines (Fe I lines) in defects-present welding shows similar features to those of the Zn I emission lines. The reason for the similarity arises from the fact that the particles of Zn and Fe stay together inside the plasma. These features were found to be the average of the relative intensity and the standard deviation of the relative intensity in the Fe I lines, despite that the features of the Fe I lines were relatively weak, compared to those of the Zn I lines. Based on the extracted features from experimental results, SVM was used to detect the defects and, further, to classify the defects using the trained model, $\mathbf{w}$ and b. These values successfully generated the hyperplanes with maximal margin in all combinations of the classes.

From the trained values, $\mathbf{w}$ and b, the trained data was classified by the hyperplane which was defined by $\mathbf{w}^t\mathbf{x}+b=0$. Two different data sets were used to compare

the performance. The two data sets are one dimensional training sets (one emission line of Fe I) and nine dimensional training sets (nine emission lines of Fe I), respectively. V-fold cross validation has been used for performance tests, since the computational cost is less expensive than that of ordinary cross-validation methods. The V-fold cross validation was performed to prevent the biased results between the training sets and the test sets. As a result, the overall predicted results are ~90 % and ~95 %. Consequently, muli-classification of the several defects was well performed. Additionally, this indirectly indicates that the use of the spectral data for the quality monitoring is very efficient compared with the use of one-dimensional data, since the OES can resolve the material constituents, unlike the conventional monitoring methods.

CHAPTER 4

THE ROLE OF ZINC COATING TO THE LIQUID VAPOR INTERFACE IN MULTILAYER SUBSTRATE OF THE LASER MATERIAL PROCESSING

In Chapter II and III, the detections and classifications of the defects in the laser material processing were discussed. In this Chapter, the mechanism of the defect formation in laser processing of the multi-coated material will be discussed by investigating the effects of the coating material to the liquid / vapor interface.

Recently, laser material processing of multi-coated substrates has been receiving more attention to satisfy growing interest in laser material interaction. In the laser material processing, characteristics of interfacial phenomena induced by phase changes, due to photon energy absorption of laser beam, play a critical role to determine energy transfer pattern from the laser beam to the target material. The interfacial characteristics in the laser material processing of the multi-coated materials are quite different from those in the processing of single material, owing to different physical properties between the base material and the coated materials. This Chapter, specifically, addresses roles of coating layer to the entire liquid/vapor interfacial phenomena which are observed in the laser material processing of zinc-coated steel. Level set method is adopted to track evolution of liquid/vapor interface, self-consistently. Several interfacial phenomena such as recoil

pressure, capillary force and thermo capillary force are estimated through a 3D simulation study. Reflective topography is employed to validate the numerical study results and to help comprehensive understanding of the interface evolution in the laser processing of the multi-coated materials.

4.1. Introduction

Lasers have comprehensively been used to process various materials, such as metals, polymers, ceramics and semiconductor. In laser material processing, phase changes of materials, such as solid/liquid (S/L) and liquid/vapor (L/V), frequently occurs, depending on laser power, since the intensive photon energy of the laser beam is transferred to the material [22]. These phase changes play a significant role in the determination of the processed material quality, since complex time-varying interfacial phenomena determine the resulting energy transfer pattern [23, 24]. Especially, the L/V interface is important in high-density laser material processing between 10^9 and10^{12} W/m^2. In this range of the energy density, several pressures, such as recoil pressure and surface tension, are mainly induced by vaporization of materials. The balance of the pressures forms the L/V interface profile which determines the energy transfer pattern [22]. For this reason, several fundamental studies related with the evolution of the interface have been performed to understand the behavior of the laser- material interaction-zone [49-51].

For single-layer material processing, various experimental studies and mathematical modeling have been extensively conducted and relatively well understood. However, recently, the laser processes of the multi-layer or multi-coated substrates are

receiving more attention to satisfy growing demands since various properties of coatings and layers give desired-functions to the primary material. The characteristics of the interfacial phenomena in the laser processing of the multi-layer or multi-coated substrates are quite different from those in the processing of the single-layer material.

Even though the understanding of the interfacial phenomena is important for the efficient energy transfer, little research has been done in this field. The little research related with this issue is summarized here. Zhang *et al.* [52] developed a transient thermal model to describe the formation of the microvia using a CO_2 laser on a multilayer substrate which consists of an embedded copper pad and both-sides covered with polymer layers. They studied volumetric heating which creates the phase transformation of the polymeric layer. The volumetric heating arises from the different absorption length of the laser beam in the polymer layer, compared with that in the metal surface. In this study, the Stefan condition was used for the analysis of the interfacial phenomena generated in the solid-vapor (S/V) interface, since the liquid layer was assumed to be thin. From the model, an overheated region was found to exist inside the polymer. Zhang *et al.* [53] expanded this modeling work into the analysis of the microvia formed by a Nd:Yag laser on the multilayer substrate, combining experimental studies. They investigated the thermal stress induced by the volumetric heating to explain the free surface evolution generated in the multi-layer substrate; however, the analysis was limited to the evolution of the only top polymer layer.

Fabbro *et al.* [54, 55] studied the behavior of the cavity formed by the L/V interface on multi-coated material which consisted of zinc coating layers and irons in the high-density laser joining processing. The zinc coating has a lower boiling point, 1180 K

than a melting point of iron, 1811 K; thus the vaporized zinc is entrapped inside the liquid iron, which leads to the instability of the entire L/V interface in the laser material processing. This group studied the spatial and temporal evolution of the cavity on single mild steel using a Nd: Yag laser with top hat mode beam. A simplified jet theory was used to model the vaporized zinc pressure. Based on the results of experimental and simulation study, they suggested that the zinc vapor needs to be induced downward for efficient process. Pan *et al.* [56] investigated the L/V interface behavior on the zinc coated steels, depending on zinc coating thicknesses, 7 µm and 20 µm. They found that the 20µm coating case generated higher vaporized pressure than that of 7 µm coating case, and it led to the more elongated cavity than that of the 7µm case. Consequently, they claimed that the process quality was improved in the thicker coating case, since the elongation of the vapor-filled cavity was helpful for ventilation of the vaporized zinc causing the decreased joining quality. A simple analytical model based on pressure balance was developed to estimate the size of the elongated cavity formed by the L/V interface. The jet theory was employed to explain the vaporized zinc pressure which mainly affects the L/V interface profile. However, all these work described above did not consider the effects by the hydrodynamics of the melt pool for the analysis of the interfacial phenomena generated in the laser processing of the multi-coated materials.

Dasgupta *et al.*[19] developed a mathematical model to explain the effects of the zinc coating on the entire evolution of the laser-material interaction-zone in a CO_2 laser material processing of zinc coated steels. This model was basically developed from the former studies conducted by [23, 30]. In this model, the authors converted the vaporization of the zinc layer into a boundary condition at the L/V interface using law of partial pressure.

This model employed a mathematical technique called level set method to track the L/V interface self-consistently by solving the Navier's stokes equation, continuity equation and energy equation. They investigated overall features of the laser-material interaction-zone, such as melt pool fluctuation and temperature distribution; however, this work has limitations to explain the effects of the zinc coating to the interfacial phenomena when the laser beam is penetrating layer by layer, since the properties of zinc were applied from the initial time step of the simulation study in the entire grids.

To the best of the author's knowledge, no research has been done regarding the role of the coating material to the evolution of the physical properties which form the L/V interface, determining energy absorption patterns. Hence, this chapter focuses on the role of the coating layer to the transition of the interfacial physics, such as capillary force, thermo-capillary force and recoil pressure, considering hydrodynamic force driven by the flow of the liquid and gas phase. As a specific case of multi-coated cases, the role of the zinc coating to the interfacial phenomena is studied in the high-density laser joining process of the zinc coated steels. At the same time, an optimized reflective topography is used as a way of experimental validation. Laser-material interaction-zone covered by bright laser induced plasma is clearly visualized by controlling the reflective beam from the interface zone. Based on the visualization of the zone, the velocity of the flow is measured. This result can be a guideline for the processing of the multi-layer substrates.

4.2. Experimental Details

The reflective topography was used to visualize the evolution of the molten pool. Figure **4-1** shows the experimental set up which consists of two lasers, target materials, high speed camera. A laser used as a heat source was a disk laser manufactured by Trumpf. This laser has 1.03 μm wavelength delivered through a 200 μm fiber with focused beam diameter of 280 μm. Beam profiles were measured by the Focus Monitor manufactured by the Primes. A focal position was set to the surface of target materials. The laser power was set to 3 kW and scanning speed was 42.3 mm per sec.

The target materials were zinc coated steels and bare steels without zinc coating. The zinc was coated at both sides of a steel plate (8.3 mm) with 7 μm and two sheets were overlapped. Hence, three zinc layers consisting of, a top, an overlapped and a bottom layers existed as depicted in Figure 4-2. The position of the material was controlled by the Anorad motion controller. The properties of the iron and the zinc were referred in [19].

A diode laser operating at 532 nm manufactured by Coherent was used to illuminate the laser-material interaction-zone for the reflective topography. The beam was delivered to the zone through an optical fiber. The optical fiber was fixed using a holder which had a convex lens focusing the divergent green light from the fiber. A diffuser plate with 1500 grid was attached at the end of the holder. This plate is essential to obtain high quality image by diffusing the light uniformly to the zone. The reflective beam by the zone was adjusted to have a direction mainly toward lens of the high speed camera using the Snell's law. In front of the camera lens, an optical band-pass filter with 532 ± 0.72 nm was put for capturing the reflective green light. A teleconverter was attached with the lens to magnify the image of the molten pool. A high speed camera manufactured by Photron was

used to monitor the evolution of the zone in the range between 1000 and 15000 frames per second.

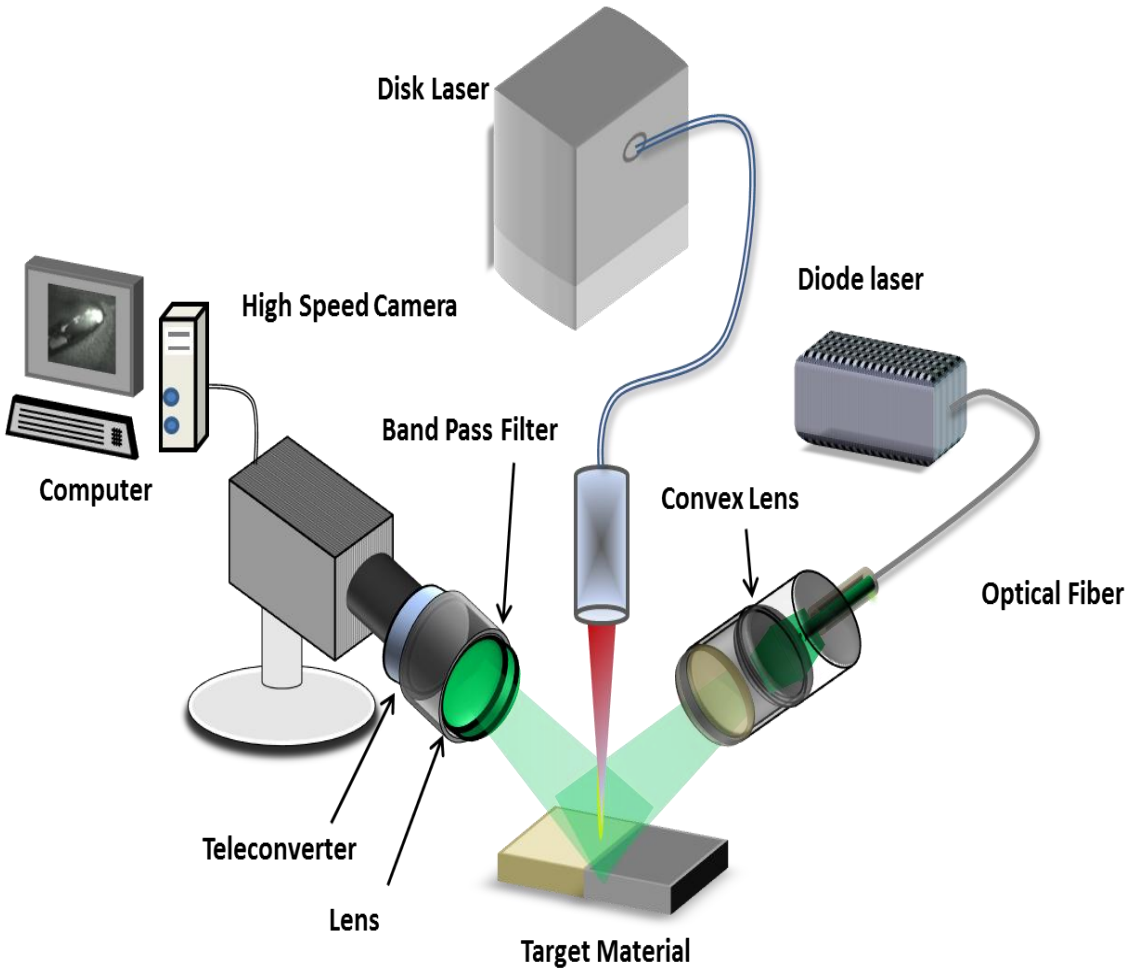

Figure 4-1 A schematic diagram of experimental setup for reflective topography to visualize liquid/vapor interface

4.3. Mathematical Model

In order to investigate the effects of the zinc coating to the L/V interfacial behavior, the previous mathematical model built in the group [19, 23, 30] was further developed. Main features of this model were briefly summarized here. The best benefit of this model is that the model is self-consistently capable of simulating the L/V interface and the S/L interface simultaneously. The level set method developed by Osher and Sethian [57] was adopted to track the L/V interface. This mathematical technique introduces a function $\phi(x,y,z,t)=d$ to assign specific values over an entire numerical domain to define certain surfaces of interest. Specifically, the target surface is the L/V interface in this study. In this equation, the d is the actual distance from the L/V interface where d is defined zero as shown in Figure 4-2. The positive and negative values of the interface indicate the surfaces above and below the L/V interface, respectively. A technique called narrow band level-set was used to implement all physics by forming a tiny band with certain distance away from the zero level [23, 58].

On the other hand, this level set method is inappropriate to model the S/L interface since the interface is morphologically complex and hence has no discrete phase change unlike the L/V interface [23]. The S/L interface forms mush zone which causes the difficulty of the use of the level method. Hence, instead of the level set method, this mush zone was modeled as a porous material using a method developed by Bennon and Incropera [59].

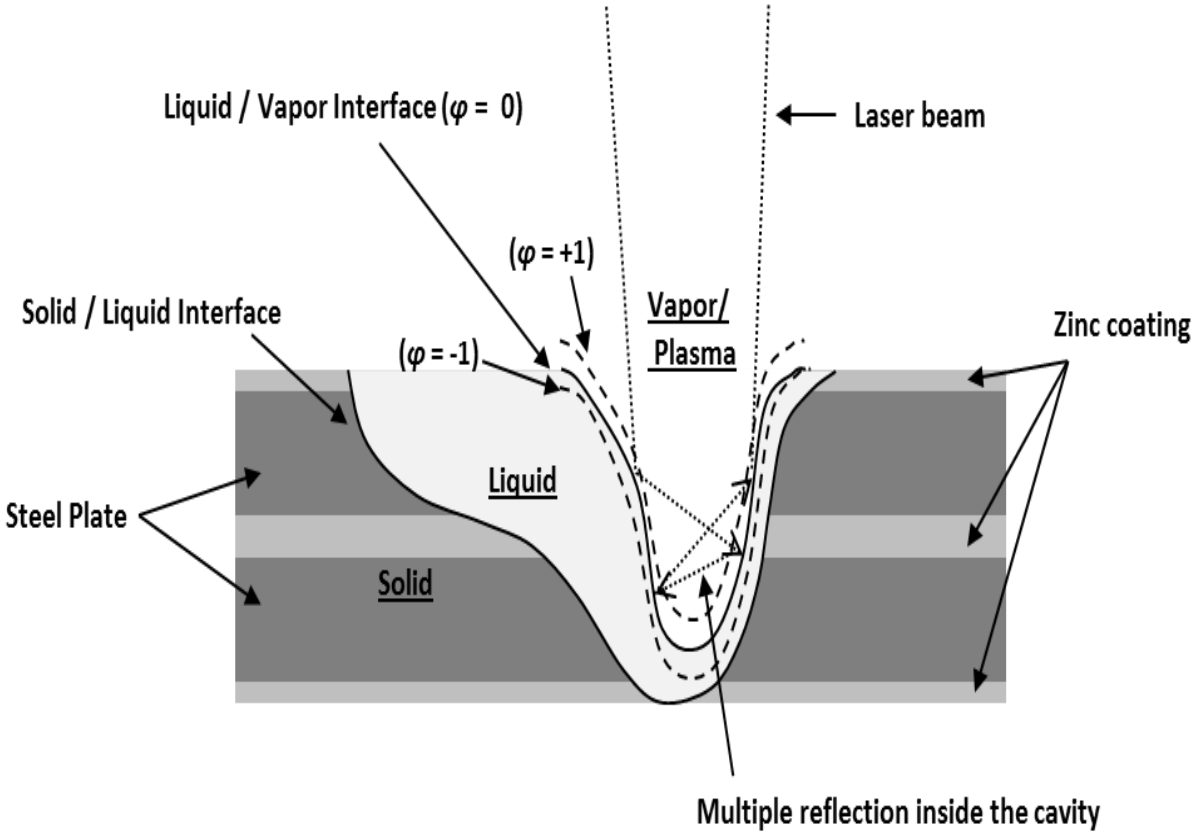

Figure 4-2 A schematic diagram of high-density laser material processing of zinc multi-coated steel illustrating liquid/vapor interface and solid/liquid interface, combined the level set method to track the liquid vapor interface.

The model proposed by Ki *et al.* was further developed in this paper [23, 30]. Additionally, the zinc vaporization physics suggested by Dasgupta *et al.* was adopted and modified at the L/V interface as a boundary condition using the law of the partial pressure[19]. From the above description of the model, the governing equations were as follows [19, 23];

Continuity equations:

$$\frac{\partial \rho}{\partial t} + \nabla(\rho \mathbf{u}) = 0 \quad \text{, with jump condition} \tag{4. 1}$$

Momentum equations:

$$\frac{\partial(\rho u)}{\partial t} + \nabla \cdot (\rho \mathbf{u} u) = \nabla \cdot \left(\mu_l \frac{\rho}{\rho_l} \nabla u \right) - \frac{\mu_l}{K} \frac{\rho}{\rho_l} u - \frac{\partial p}{\partial x} - \mathbf{e}_x \cdot \left(\sigma \mathbf{n} \kappa - \nabla_s T \frac{d\sigma}{dT} \sigma - m_{\mathrm{Zn}} p^{\circ}_{\mathrm{Zn}} A \right) \delta(\phi) \tag{4. 2}$$

$$\frac{\partial(\rho v)}{\partial t} + \nabla \cdot (\rho \mathbf{u} v) = \nabla \cdot \left(\mu_l \frac{\rho}{\rho_l} \nabla v \right) - \frac{\mu_l}{K} \frac{\rho}{\rho_l} v - \frac{\partial p}{\partial y} - \mathbf{e}_y \cdot \left(\sigma \mathbf{n} \kappa - \nabla_s T \frac{d\sigma}{dT} \sigma - m_{\mathrm{Zn}} p^{\circ}_{\mathrm{Zn}} A \right) \delta(\phi) \tag{4. 3}$$

$$\frac{\partial(\rho w)}{\partial t} + \nabla \cdot (\rho \mathbf{u} w) = \nabla \cdot \left(\mu_l \frac{\rho}{\rho_l} \nabla w \right) - \frac{\mu_l}{K} \frac{\rho}{\rho_l} w - \frac{\partial p}{\partial z} - \mathbf{e}_z \cdot \left(\sigma \mathbf{n} \kappa - \nabla_s T \frac{d\sigma}{dT} \sigma - m_{\mathrm{Zn}} p^{\circ}_{\mathrm{Zn}} A \right) \delta(\phi) \tag{4. 4}$$

Energy equation:

$$\frac{\partial\left(\rho \overline{C_{pl}} T\right)}{\partial t} + \mathbf{u} \cdot \nabla\left(\rho \overline{C_{pl}} T\right) = \nabla \cdot (k \nabla T) + \frac{\partial\left(\rho f_l L\right)}{\partial t} + \frac{\partial\left(\rho f_s \Delta \overline{C_p} T\right)}{\partial t} + (q''_{L/V} - \rho_l L_v F_{evap} - \sigma \varepsilon (T^4 - T_\infty^4) \delta(\phi) \tag{4.5}$$

where, **u** is velocity vector and ρ is density. *u, v, w* are the velocities and $\mathbf{e}_x$, $\mathbf{e}_y$, $\mathbf{e}_z$ are unit vectors in x, y, z directions, respectively. μ is viscosity, σ is surface tension, κ is curvature, and **n** is the normal vector along moving L/V interface. The subscripts, *s*, *l* and *v*, indicate solid, liquid and vapor, respectively. *f* is mass fraction and ∇_s is surface nabla. $q''_{L/V}$ is the spatial laser-beam distribution, *K* is the isotropic permeability, and $\overline{C_p}$ is the average mixture specific heat. L_v is latent heat of vaporization and a constant *A* is the grid area [19, 23]. m_{zn} and P_{zn}^{0} are mole fraction and partial pressure of the zinc vapor calculated using law of partial pressure, among the mixture of iron and zinc. The specific properties were referred in the [19, 23]. $\delta(\phi)$ is the Dirac delta function which has value 1 at the interface (ϕ=0) and 0 except the interface as illustrated in Figure 4-2.

The jump condition was used to compensate the mathematical discontinuity which exists in the Knudsen layer of several mean free paths [60]. This thin layer is formed just outside the L/V interface when the evaporation starts to occur. Across this layer, the continuum hypothesis is not valid and sudden properties changes of density, pressure, temperature exist. Jump condition with back pressure is adopted and the details are omitted here [51].

Some assumptions and contributions are made to develop this model further in this chapter. The assumptions are listed as follows:

a. As shown in the Figure 4-2, a top zinc coating among three zinc coatings was assumed as a free surface because the coating layer is vaporized before the melting of the base material, iron. Therefore, its effects on the behavior of the L/V interface are negligible. However, the bottom layer was not assumed as a free surface, since the vaporized zinc pressure induced by the bottom zinc layer can cause the flow change and the instability of the L/V interface when the zinc vapor move upward through the L/V interface.
b. In order to investigate the role of the zinc coating to the interfacial phenomena layer by layer, the evolution of the L/V interface moving along *z* direction (laser penetration direction) is required. Therefore, a new computational module regarding the zinc layers was established and was selectively applied for a comparative study between a zinc coated case and a zinc absent case. Hence, the zinc present case and the zinc absent case were compared simultaneously under the same process parameters, such as laser power and scanning speed.

c. A recently developed model of the recoil pressure was adopted to calculate the kinetic energy exchange at the Knudsen layer. The detail equation, (4.6) is explained later.
d. When this model solves the governing equations, the zinc layer properties are embedded at the position where the coating layers are located.
e. Surface tension of zinc is negligible since the zinc coating thickness is small compared with that of the steel.
f. The re-condensation effect of the vapor mixture is not considered.
g. Gas phase flow is assumed to be incompressible.
h. Due to the huge difference of the material properties between liquid and vapor, the properties are smoothed.
i. The effect by the laser induced plasma is ignored.

In the Knudsen layer, as described above, the physical properties such as temperature, density and pressure are discontinuous. As a result, the recoil pressure induced by evaporating mass flux and back scattering flux is important to form the L/V interface. In this model, an approximated equation by kinetic energy exchanges between the two fluxes was adopted as follows [61]:

$$P_{rec} \cong \frac{\rho_e u_e^2 + \rho_b u_b^2}{2\rho_e u_e^2} P_{sat}(T_s) \qquad (4.6)$$

where P_{rec} is recoil pressure, T_s is saturation temperature, $P_{sat}(T_s)$ is saturation pressure at the temperature, u_f and u_b are velocity of backward mass flux and forward mass flux,

respectively, ρ_f and ρ_b are density of the backward mass flux and forward mass flux, respectively. Those properties are obtained based on the reference [62].

In this chapter, the disk laser operating at 1.03 μm was used for the simulation. The corresponding absorptivity to the material was assigned to 0.4 [24]. Top hat mode was selected as a beam mode for this simulation. Non-uniform mesh was used in this numerical study to reduce the computational cost and to observe the entire behavior of the L/V interface over the domain. A stagger grid was used to prevent numerical error of the pressure field and the CFL condition was considered for the stable convergence of the numerical simulation. [63].

4.4. Results and Discussion

4.4.1. Simulation Results

In the high-density laser material processing between 10^9 and10^{12} W/m^2, the L/V interface plays a dominant role to determine the processed quality, since most of the laser energy is absorbed at the L/V interface. As shown in Figure 4-2, at the L/V interface, laser energy absorption through the multiple reflections generates a concave cavity, due to the evaporation and ejection of the molten metal, induced by the energy absorption. The L/V interface cavity is formed by complicated interfacial phenomena, such as recoil pressure and capillary force and thermo-capillary force.

In order to study the role of the zinc coating to the interfacial phenomena, comprehensive analyses including a numerical study and experimental observations were conducted. Computational modules related with zinc coating were selectively turned on for

a comparative study between a zinc coated case and a zinc absent case. Hence, the zinc coated (ZC) case and the zinc absent (ZA) case were compared simultaneously, as plotted in Figure 4-3. This figure shows the evolution of the physical terms at the L/V interface. The ZC case and the ZA case are expressed by blue and light magenta (color online). A dotted vertical line across the figure indicates a border between a zone (i) and a zone (ii). The zone (i) represents the evolution of the L/V interface in both cases, until the L/V interface of the ZC case reaches the middle zinc layer for the first time, as shown in Figure 4-2. Note that the top zinc layer was assumed to be free surface and the middle zinc layer is thicker than other zinc layers since the zinc layer is overlapped as described above. Therefore, the zone (i) is expressed as one color since both the ZC and ZA cases have the same behavior.

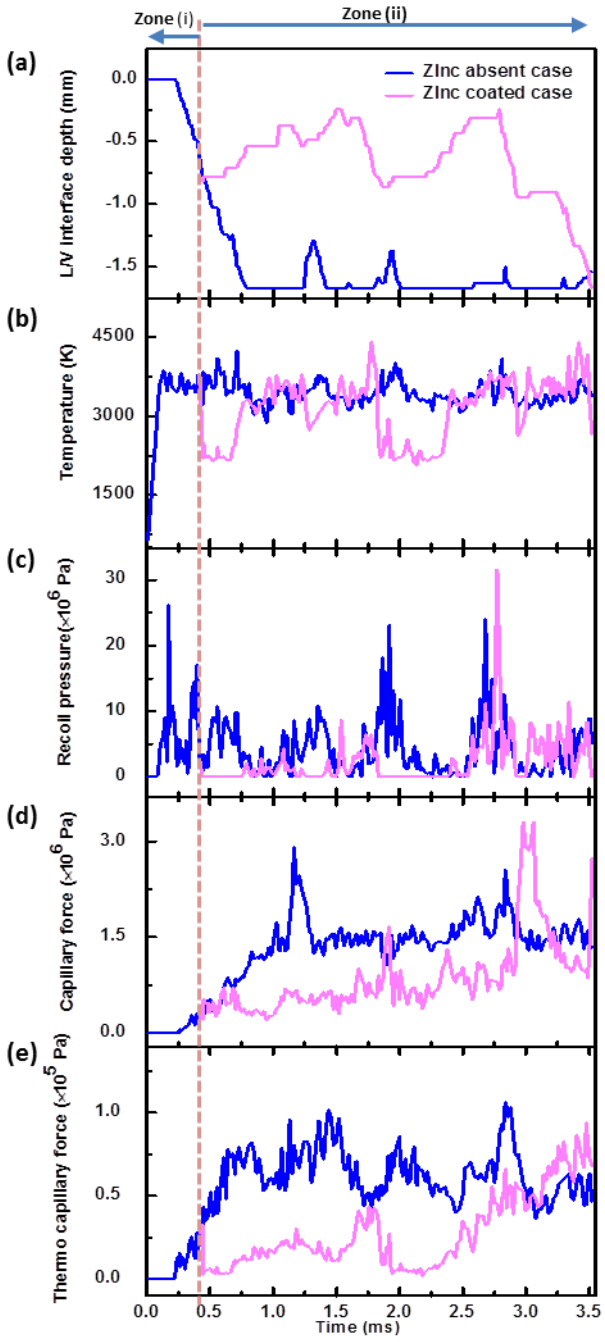

Figure 4-3 Temporal evolution of physical properties at the entire liquid vapor interface (a) depth of cavity formed by the liquid/vapor interface, (b) Temperature, (c) recoil pressure, (d) capillary force and (e) thermo-capillary force. The zinc coated case and the zinc absent case are expressed by blue and light magenta (color online). The dotted vertical line across the figures indicates the border between the zone (i) and the zone (ii). The zone (i) indicates the

evolution of liquid/vapor interface until the interface reach the middle zinc layer since the top layer is assumed to be free surface. Therefore the zone (i) is expressed only one color since the zinc coated and zinc absent case have the same behavior.

Figure 4-3(a) qualitatively shows the depth evolution of the cavity formed by the L/V interface of the both cases. These interfaces are moving downward due to the evaporation and the ejection of the molten material by absorbing the energy from the laser beam. Both ZA and ZC cases reveal the same physical behavior up to 0.45 ms. After the 0.45 ms, in the ZA case, the cavity is continuously penetrating downward across the steel plates. On the other hand, in the ZC case, as the L/V interface reaches the overlapped zinc coating layer located 0.82 mm downward from the top surface of the material, the cavity temporary does not penetrate through the coating layer. After 0.45 ms, the cavity depth is entirely fluctuated until ~3.2 ms. Specifically, when the cavity formed by the L/V interface reaches the coating at the 0.45 ms and 1.85 ms, the L/V interface is transitory moving upward. Physically, this indicates that the pressure balance forming the cavity is disrupted at the bottom of the cavity, as the interface contact the coating layer, due to the abruptly increased pressure induced by zinc layer vaporization. Basically, this phenomena results from the difference between the zinc boiling temperature, 1180 K, and the melting temperature of the iron, 1811 K, since the vaporized zinc cause the instability of the L/V interface behavior. Therefore, the vaporized pressure resists the recoil pressure which pushes the cavity downward. At the same time, the molten metal is explosively ejected by the increased pressure. As a result, the L/V interface is temporary moving upward until the interface obtains the enough force which presses the L/V interface downward again. In regard to the recoil pressure, detail explanations will be discussed in Figure 4-3 (c). After

3.24 ms, the interface begins to penetrate across the coating layer, overcoming the increased pressure by the zinc vaporization. This phenomena results from that the momentum induced by the vaporized zinc is absorbed by the developed melt pool with the density of 6518 kg/m^3 like a damper. Consequently, it takes more time, 3.5 ms for the full penetration due to the existence of the zinc coating, compared with 0.75 ms in the ZA case.

As depicted in Figure 4-3(b), in the ZA case, while the temperature mostly varies near the boiling temperature of the iron (3133 K), there are two remarkable areas which have huge temperature drop up to ~2200 K in the ZC case. The temperature is decreased around ~0.45ms and ~1.85ms where the L/V interface contacts the zinc coating, as shown in Figure 4-3(a). The temperature drop is owing to the increased convective heat transfer induced by the zinc layer vaporization. That is, this vaporization accelerates the flow velocity of the gas and liquid phases inside molten pool, and it leads to the ejection of the liquid not by the recoil pressure. Consequently, the convective heat transfer causes causing temperature drop. In the entire temperature variation, three more spots exist for momentary temperature drop up to ~2700 K around ~1.27 ms, ~3.0 ms and 3.5 ms. The decreased temperature is owing to the relatively reduced flow velocity by the remaining momentum inside the cavity and the less damping effect by the immature molten pool. That is why the restoring of the temperature drop occur without the significantly change of the L/V interface depth, and the temperature drop is not huge as much as the previous two zones. Latent heat of the zinc vaporization is negligible for the decreased temperature since the coating thickness (7 μm) is very small compared with amount of the molten steel (8.2 mm) to generate such huge temperature drop.

Pressure balance is important to form the stable L/V interface evolution during the laser material processing. As described earlier, the L/V interface shapes the concave cavity

by the multiple reflections. Therefore, the L/V interface forming the cavity is established by several kinds of pressures, such as recoil pressure, radiation pressure, hydrodynamic pressure, hydrostatic pressure, and surface tension consisting of capillary force and thermo capillary force [56]. Among the pressures, the dominant pressures are recoil pressure, capillary force, and thermo capillary force [56, 64]. In the most of the other researches, these terms were usually obtained without considering the geometrical change of the L/V interface. Especially, in order to analyze the momentum induced by the zinc layer vaporization, the hydrodynamic effect driven by the flow has to be explained. However, in the studies, simple analytical models were used to estimate the pressures. Therefore the results were limited to predict realistic estimations of the physical behavior. Hence, the dominant forces considering the time-varying geometry induced by the hydrodynamic force are estimated and plotted as shown in Figure 4-3(c), (d), and (e). Each pressure was expressed as a summation of the existing pressure at the entire grid forming the L/V interface, since the interfacial evolution has to be shown at each time step.

Figure 4-3(c) shows the evolution of the recoil pressure which changes sensitively because the L/V interface is oscillated by the time-varying pressure, due to the steep change of the physical properties at the Knudsen layer. For this reason, the recoil pressure is very sensitive in time to time. The evaporation in the ZA case continuously takes place during the process. On the other hand, in the zone (ii), the recoil pressure of the ZC case sometimes has zero in from ~0.45 ms to ~0.75 ms and from ~1.85 ms to ~2.38 ms. Additionally, these phenomena occur around 1.265 ms, 2.94 ms and 3.52 ms. All these are the corresponding positions where the temperature drops occur. This physically indicates that evaporation temporary does not generate due to the temperature drop below the boiling point (3134 K) of the primary material, iron. In principle, the recoil pressure is induced by

momentum change between the evaporating mass flux and the condensing backscattering fluxes, as shown in (6) [61]. As a result, the hydrodynamic force induced by the zinc vaporization disrupts the recoil pressure which suppresses the molten pool, since the evaporation does not generated because of the temperature drop below the boiling point.

As shown in Figure 4-3(d), the capillary force in the ZC case becomes larger than that of the ZA case, in the zone (ii). This arises from the geometrical change of the interface, as explained in the momentum equations, (2), (3), and (4) as expressed above. In the equations, the capillary force is expressed as $\sigma \mathbf{n} \kappa \delta(\phi)$. This mathematical form represents that the force exerts on the normal direction depending on the curvature of the interface. In order to explain the difference of the capillary force, the 3-D shapes of the L/V interface in both cases are illustrated in Figure 4-4. In the ZA case, the L/V interface forms the cavity with high aspect ratio compared with that of the ZC case. That is to say, the shallow and elongated molten pool due to the vaporized pressure has smaller restoring capillary force which decrease the concavity of the cavity compared with the ZA case. Figure 4-3(d) shows relatively few high peaks exist among the entire evolution: A peak in the ZC case around 1.25 ms and a peak in the ZA case around 3.1 ms. It is found that these peaks are because of non-linearity leading to the time-varying geometrical change of the interface, driven by the sensitive change of the pressure and the flow patterns. The peak of the capillary force in the ZA case is related with the change of the L/V interface depth at the corresponding time, as shown in Figure 4-3(a). In other words, the cavity depth variation indicates the geometrical change of the L/V interface shape. Hence, this change causes the variation of the radius curvature and the normal direction where the capillary force exerts at the corresponding time step. For this reason, the geometrical change of the interface can lead the fluctuation of the capillary force. The peak in the ZC case results from the similar

reason since the L/V interface at the 3.1 ms starts to form the high concavity of the interface.

Figure 4-3(e) shows the characteristics of the thermo capillary force at the interface. This force results from the spatial temperature gradient of the molten flow. This force exerts to the opposite direction of the restoring force, the capillary force. Right after the zone (i), while the thermo capillary force is continuously growing in the ZA case, the thermo capillary force begins to decrease from ~0.45 ms in the ZC case. Then, the force is gradually increased up to ~1.85 ms. After ~1.85 ms, the force is decreased again. The decrease of the force take places at the corresponding positions where the cavity contact to the zinc coating, as displayed in Figure 4-3(a). In other words, the liquid ejection reduces the thickness of the developed liquid layer, which induces the temperature gradient causing the thermo capillary force. Note that the temperature drop as described earlier does not develop the increased temperature gradient inside the molten pool. In order to check this result, the shapes of the L/V interface in the ZA and ZC cases, generated at ~3.1 ms, are illustrated in Figure 4-4. In the ZC case (right-side), the increased pressure from the zinc vaporization generates the more ejection of the molten metal rather than forming the high concave cavity which induce the deep molten pool. As a consequence, the explosive liquid ejection and the increased gas flow by the zinc vaporization prevents to develop the deep molten pool which has enough temperature gradient causing the thermo capillary force.

4.4.2. Experimental Validation

The reflective topography is used to investigate of the evolution of the L/V interface. Unlike the sole use of the high speed camera, this technique enables the visualization of the laser material interaction zone, regardless of the bright laser induced plasma. The velocity of the molten flow and the evolution of the explosive L/V interface were estimated to validate the simulation results and to help the comprehensive understanding of the interfacial evolution.

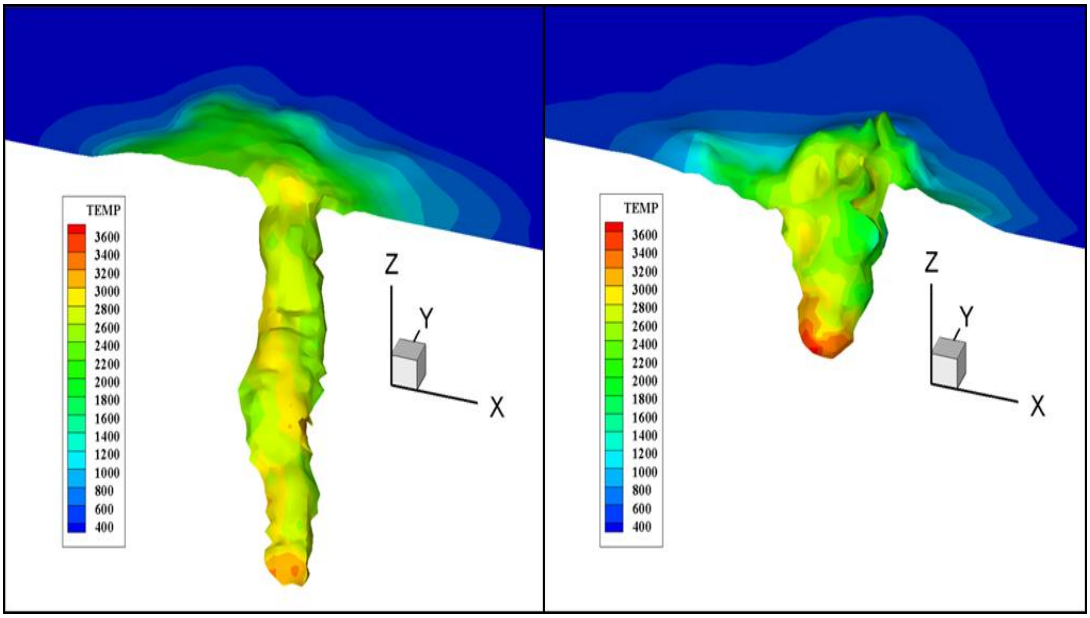

Figure 4-4 The shape of the cavity formed by the liquid/vapor interface in the zinc absent case (left) and the zinc coated case (right).

Figure 4-5 shows captured images recorded with 1000 frames per sec to investigate the entire characteristics of the molten flow during the processes. In the ZA case (a), the profile of the molten pool is uniform. In contrast, in case (b), the profile is very uneven.

This arises from the complicated flow pattern induced by the zinc layers vaporizations. Especially in the ZC case, when the laser beam is irradiated on the top zinc coating, the layer is free surface, and therefore it is vaporized immediately. However, as the laser beam energy is becoming absorbed, the molten liquid is developed above 1811 K, which exceeds the vaporization temperature of the zinc. Consequently, solid zinc coating located around the edge of the molten pool exerts as a shear force to accelerate the melting flow in the tail of the molten pool. This phenomenon is combined with the complicated flow pattern induced by the vaporization of the zinc layer, and leads to the uneven contour.

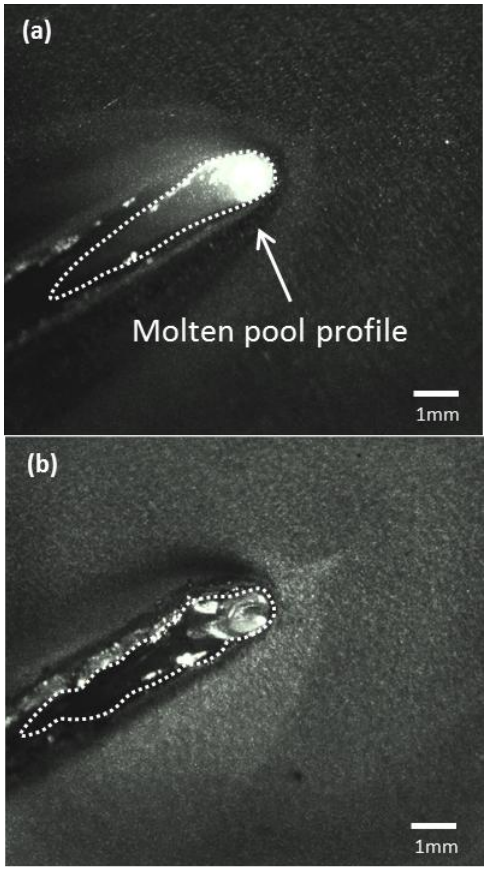

Figure 4-5 Characteristics of the molten pool profile at the top surface in (a) the zinc absent case and (b) the zinc coated case.

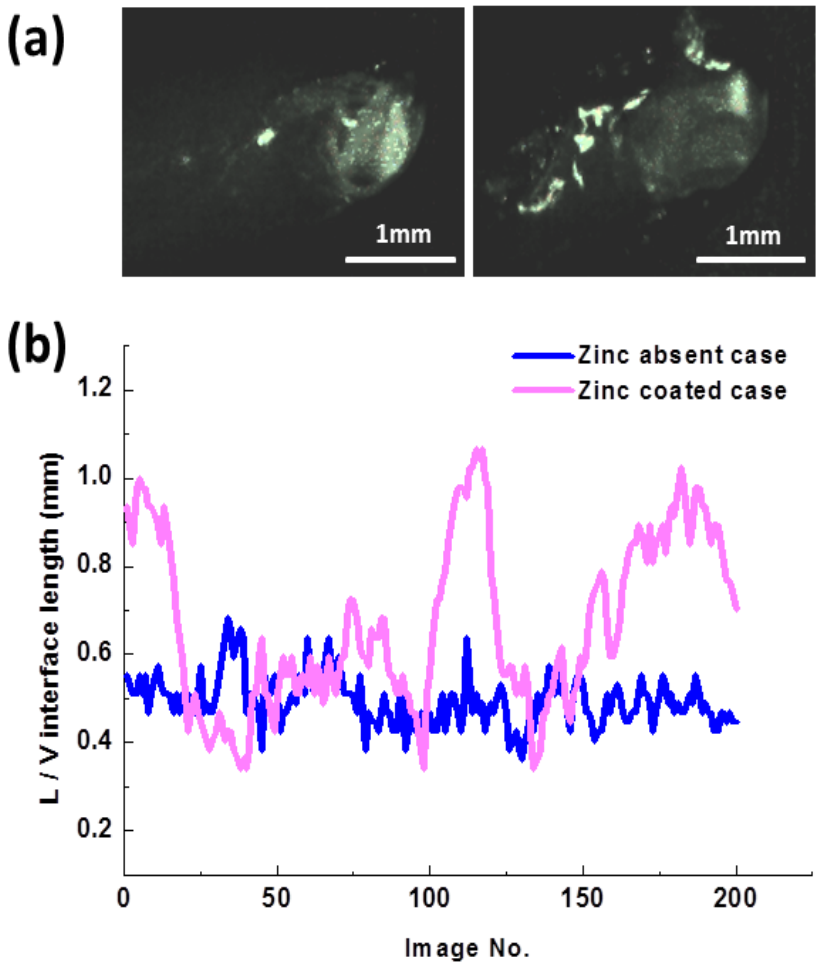

Figure 4-6 (a) Characteristic of the liquid/vapor interface zone in the zinc absent case (left) and in the zinc coated case (right). (b) The length variation of the liquid/vapor interface from the successive 200 images, recorded with 15000 frames per second by the high speed camera.

The ZC case has additional feature, showing that the L/V interface is extended toward both front and rear in the laser-material interaction zone. For the detail visualization of the zone, the aperture size and the frame rate of the high speed camera are optimized depending on the power of the diode laser, because laser induced plasma is usually too

bright to visualize the inside of the laser-material interaction zone. That is to say, the amount of the beam from the diode laser has to become larger than the plasma for observing the details inside the zone.

Figure 4-6 shows the captured images recorded with 15000 frames per second and the calculated length of the L/V interface from the successive 200 pictures. For the ZA case shown in the left side of Figure 4-6 (a), the front-downside wall of the cavity formed by the L/V interface is brighter than that of the ZC case (right). In the reflective topography, the degree of the brightness represents the topography of inside the cavity, since the surface profile determines the reflection angle causing the degree of the brightness, following the Snell's law. Therefore, the difference of the brightness explains that the vaporized zinc, filling inside the cavity, presses the thin liquid layer. Therefore, the dimly bright area in the corresponding position of the ZC case explains the elongation of the L/V interface downward. Additionally, the longitudinal length variation, acquired from the 200 pictures in the ZC case, shows the elongation and shrink of the entrance concave cavity, repeatedly, compared with that of the ZA case, as shown in the Figure 4-6(b). This fluctuation is related with the L/V interface depth change as shown in Figure 4-3(a). That is, the depth change arises from the fluctuation of the recoil pressure which presses the L/V interface. These changes of the recoil pressure result from the hydrodynamic force induced by the zinc layer vaporization. This entrapped zinc vapor inside the cavity push the molten liquid out when the vaporized zinc has enough momentum up to the certain level. As a result, after the vaporized zinc escapes away from the cavity, the length of the cavity entrance is reduced due to the release of the pressure from the vapor-filled cavity. As shown in the Figure 4-6(b), the length of the interface in the ZC case varies from 1.06 mm to 0.34 mm.

On the other hand, the ZA case changes from 0.36 mm to 0.68 mm, respectively. The length confirms the calculated L/V interface from the simulation results as shown in Figure 4-4. The lengths of the L/V interface entrance following the x-direction is 0.35 mm in the ZA case and 0.94 mm in the ZC case, respectively. The ranges of the simulation results are quite reasonable with the experimental observations.

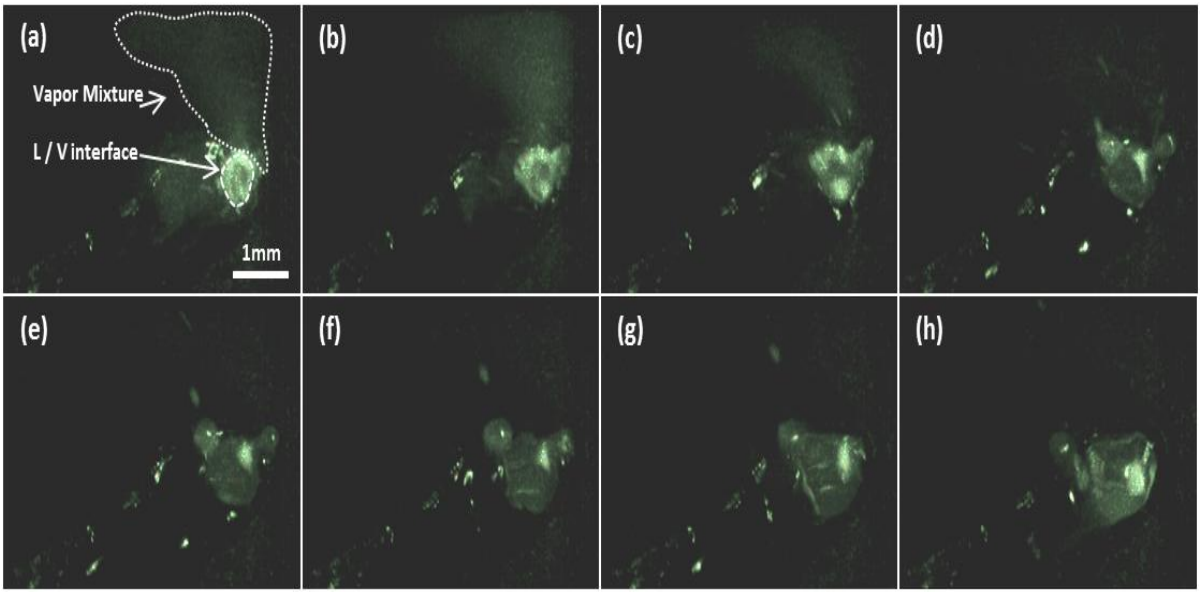

Figure 4-7 The transition of the molten pool and the vapor mixture in the zinc coated case, sequentially observed for 1.06ms

The transition of the molten pool and the vapor mixture in the ZC case are sequentially observed for 1.06 ms as depicted in Figure 4-7. The vapor mixture illustrated in (a) is pushed out of the cavity entrance. When the intensive mixture escapes away from the cavity, the corresponding entrance size of the cavity is enlarged and the density of the mixture is diminished as displayed Figure 4-7(a)-(h). In other words, once the zinc-induced momentum is enough, the momentum enlarges the entrance of the cavity. This lead to the

ejected melt wave which forms bubbles observed at the front and the rear side of the cavity entrance as shown in the Figure 4-7(c)-(e). The ejected melt wave is generated from the middle zinc coating, since the surface of the molten pool just behind the cavity is swelling just before the formation of the bubble. Several spatters generating near the cavity wall are observed. The flow speed is measured using the image software and the reference grid which is similar way with [30] . For, the tiny spatter observed flying out of the cavity has a speed of 4.5 m/s. For the flow near the front wall of the cavity, the velocity range from 1.5 to 1.9 m/s in the ZC case. On the other hand, in the ZA case, the velocity varies from 0.6 m/s to 0.8 m/s. These velocities are consistent with the simulation results.

Figure 4-8 illustrates the L/V interface profile inducing having a porosity defect induced by the zinc vaporization and an optical microscope picture of the joined sample which has the defects. In order to obtain the image, the processed samples by the disk laser are cut and etched using 2.4 % nitric acid and 97.6 % ethylene. As shown in Figure 4-8(a), in the position where the overlapped zinc layer is located, the interface is pushed toward $-x$ direction, opposite to the direction of the laser scanning direction. This is caused by the increased pressure from the front wall of the cavity by the zinc vaporization. The pressure is partially propagated into the rear wall and partially vaporized upward through the open cavity. This induces the some direction change of the flow to backward in the position where the overlapped zinc layer is located, as depicted in the Figure 4-8(a). Arrows indicates velocity vectors. In addition, the evaporation of the bottom zinc layer pushes the L/V interface upward due to increased momentum. Therefore, the relatively thick molten zone is formed below the cavity due to the reduced recoil pressure as explained before. These mechanisms result in the porosities as shown in the Figure 4 8(b), because the

pushed vaporized zinc is entrapped inside the molten pool, and then solidified. There are two porosities found near the middle zinc layer. This explains that the simulation results are reasonable.

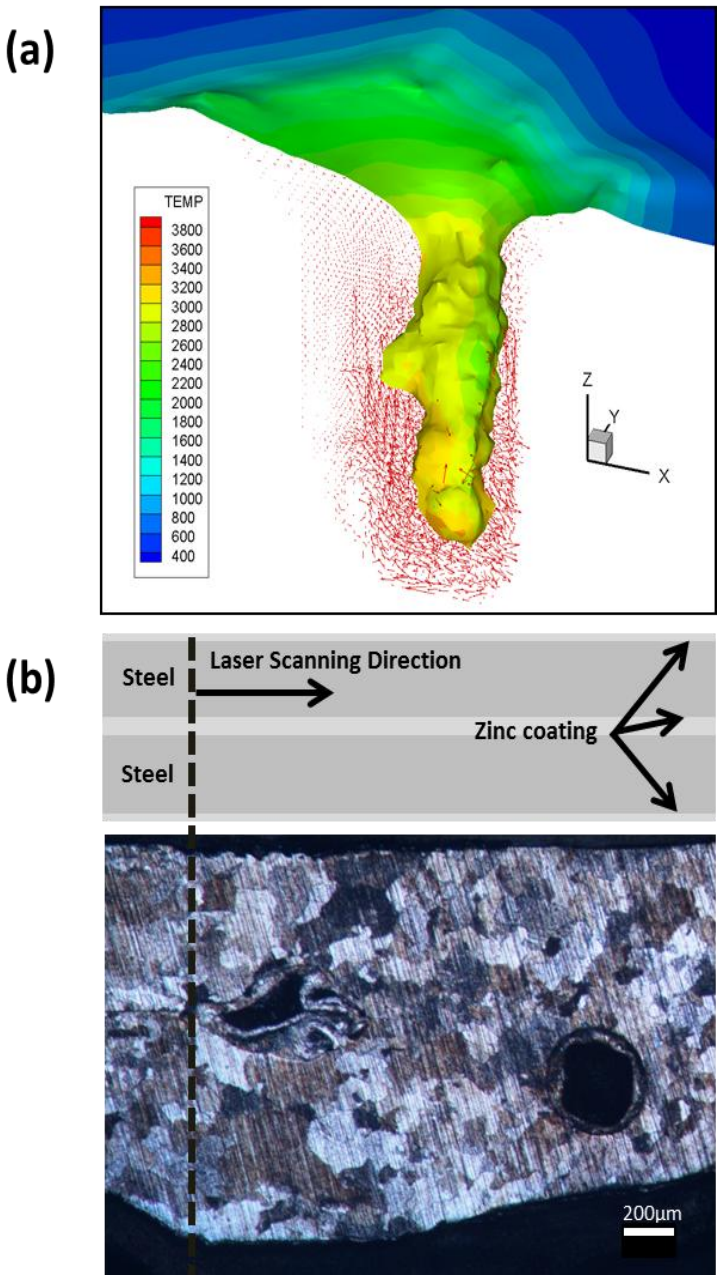

Figure 4-8 The L/V interface profile inducing a porosity defect induced by the zinc vaporization and an optical microscope picture of the joined sample which has the defects

4.5. Conclusion

In the chapter, the role of the coating material to the interfacial phenomena is explained in terms of the evolution of the physical properties well. The experimental observations are combined to validate the simulation results and to understand the evolution of the interfacial phenomena. The findings are summarized here.

- The vaporization of the zinc coating induce the increased hydrodynamic momentum which increase the flow velocity, and this leads to the ejection of the liquid metal and the temporary temperature drop which causes the reduced evaporation. The reduced recoil pressure leads to the temporal fluctuation of the L/V interface, since the cavity formed by the L/V interface move up and down depending on the recoil pressure.

- The capillary force in the ZC case is decreased compared with that of the ZA case, in the position where the vaporization of the zinc coating layer. This force is closely related with the radius curvature of the L/V interface shape from the Young's law. The less developed concavity of the L/V interface in ZC case results in the lower capillary force compared with that of in ZA case.

- The reflective topography is used to investigate of the evolution of the L/V interface. This technique can cover the visualization of the laser material interaction clearly depending on the amount of the reflective beam. From the clear observation results, the elongated L/V interface, the flow and spatter velocities are monitored. Due to

the momentum created by the zinc coating, the elongation and shrinkage of the cavity formed by the L/V interface are repeated. The velocity of the liquid metal at the side wall of the L/V interface cavity in ZC case is almost double to that of the ZA case.

- Because of the vaporization pressure in the middle zinc layer, the L/V interface is pushed backward, and hence it leads to the change of the molten flow at the position of the zinc layer. Additionally, the vaporized zinc from the bottom zinc coating, some portions of the zinc vapor is entrapped in the bottom area. To validate this phenomenon, the processed sample is cut long with the scanning direction. At the initial area of the laser irradiation, the existing porosity near the zinc layers confirms that the simulation result is reasonable.

CHAPTER 5

CHARACTERISTICS OF ENERGY TRANSFER IN A DISK LASER AND A FIBER LASER

In this chapter, spectroscopic studies are performed to investigate the characteristics of energy transfer in a disk and a fiber laser. As described in the Chapter I, newly developed lasers have been increasing the efficiency of the laser material processing. However, the selection of the proper laser is not easy for users because of high cost. For this reason, in this chapter, spectroscopic studies are conducted for evaluating energy absorption by laser induced plasma in the disk and fiber lasers to provide users with insight into which laser might be more suitable for a given application.

5.1. Introduction

Due to relatively small footprint and excellent wall plug efficiency, diode pumped solid state lasers (DPSS) have been utilized in the laser material processing field [22]. However, the DPSS has an inherent problem called thermal lensing caused by different thermal gradients of gain medium, causing a limitation in laser beam quality [25, 26]. To improve beam quality by overcoming this issue, a disk laser and a fiber laser have been developed as alternative solutions to conventional lasers [26, 27].

The disk laser uses a thin disk as an active medium, mounting on a heat sink to minimize thermal distortion; simultaneously, the face cooled by the heat sink is used as a folding or ending mirror of the resonator to achieve increased optical gain [27, 65]. On the other hand, the fiber laser employs a long double clad fiber to better dissipate heat and facilitate side pumping over the fiber length; each cladding has a different refractive index causing an internal reflection, which allows increasing optical gain by guiding the electromagnetic wave [25, 26, 66].

Even though the disk and fiber laser systems are promising solutions compared to conventional DPSS, laser-users need information regarding selections of the laser based on their specific need, particularly in terms of energy transfer. To assess the laser systems, two factors are considered: energy absorption by the laser induced plasma which is an inevitable phenomenon in laser material interactions, and the penetration features of the irradiated sample by the attenuated laser beam after absorption by the plasma. Using three spectrometers, the interaction of the fiber laser and aluminum solid target has been investigated in terms of plasma characterization and the generated crater [67]. The performance of the high power fiber laser has been evaluated from fusion zone geometry by changing spot sizes and scanning speeds [68]. A comparative study between a disk laser and a Nd:YAG laser has been conducted on the process parameter changes [69]. Despite a few studies, there are no reports that have been completed regarding systematic comparisons between these two recently developed laser systems.

In this chapter, spectroscopic studies are conducted for evaluating energy absorption by laser induced plasma in the disk and fiber lasers. Electron temperature and electron density are determined for the evaluation using emission spectra. Moreover, the

penetration characteristics are observed, since the penetration profiles caused by the re-solidification of the molten material result from the absorption of the laser beam.

5.2. Experimental Set-up

A schematic of the experimental set up consists of a laser, target materials, and a spectrometer connected with a computer, as shown in Figure **5-1**. The fiber laser used in this study has a 1070 nm wavelength and a 640 µm laser beam diameter. The laser beam is delivered through a 400 µm optical fiber, and the beam mode is Gaussian. In contrast, the disk laser used in this study has a 1030 nm wavelength. The beam of the disk laser is delivered through a 200 µm optical fiber. The beam diameter is 300 µm and the beam mode is top hat in the disk laser. The focal length of both laser systems is 200 mm. For the experiments of this study, the disk laser beam was defocused downward 3.6 mm from the focal position, based on the measured beam profile done by the FocusMonitor manufactured by the Primes, since two systems were to be compared under the same power densities. The beam profile is illustrated in Figure **5-2**.

A spectrometer HR-2000 manufactured by Ocean Optics is equipped to measure emission spectra in the range of 340 nm to 440 nm. To generate the emission spectra, spheroidal gray cast iron was irradiated by both lasers. The emission spectra were recorded using the spectrometer at the surface of the material. An optical fiber with 600 µm diameter was used to deliver the measured optical signal. The spectrometer has a 10 µm entrance slit and 2400 / mm groove density. The resolution of the spectrometer is 0.1 nm. A sampling time for the recording signal was set at 5 ms.

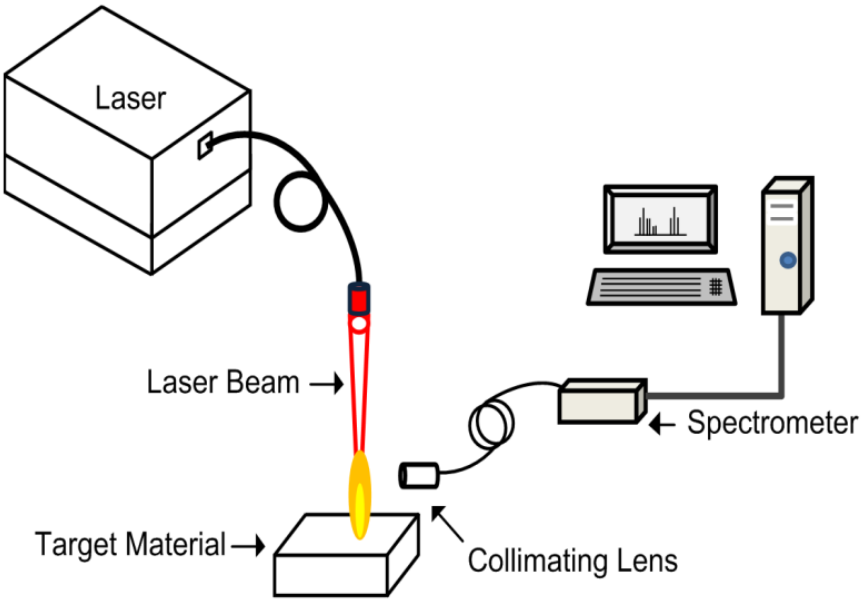

Figure 5-1 A schematic diagram of experimental set up in order to compare laser characteristics.

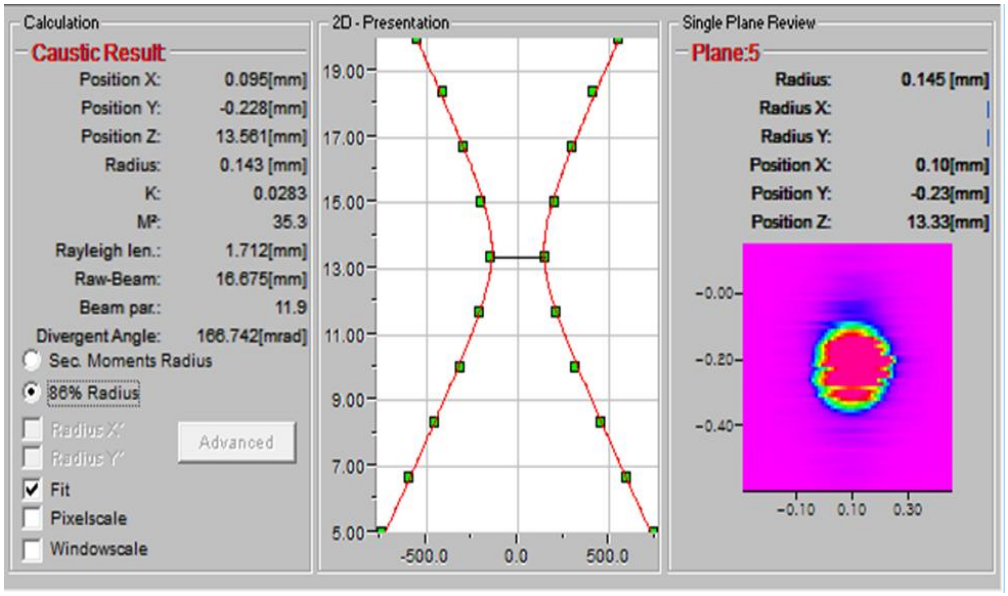

Figure 5-2 Beam profile measured using FocusMonitor

Experimental sets were divided into four groups to investigate penetration characteristics based on the change of laser power. The laser powers were 1 kW, 2 kW, 3 kW and 3.9 kW in each set. The 3.9 kW was used instead of 4 kW for the safety of the laser systems. Corresponding power densities were 3.1×10^9 W/m^2, 6.2×10^9 W/m^2, 9.3×10^9 W/m^2 and $12.^4 \times 10^9$ W/m^2, respectively. The latter condition was used for determining electron temperature and electron density. To investigate clean boundaries of the re-solidification area, 2.4 % nitric acid and 97.6 % ethylene was used for the chemical etching. All the experiments were conducted under bead-on-plate conditions in air. The laser scanning speed was 50 mm/s. Argon gas was used with 40 SCFH of flow rate as a shielding gas.

5.3. Results

5.3.1. Plasma Characteristics

Since laser induced plasma is responsible for significantly blocking the energy transferred from the laser beam to the solid target, the plasma absorption was characterized using electron temperature and density evaluated from the emission spectra generated by the irradiated samples. As an initial stage of the characterization, the emission spectra under the power density of 12.4×10^9 W/m^2 were measured at both systems as shown in Figure 5-3

Figure 5-3 reveals that the emission profiles are similar. The positions of the peaks are almost identical. There is a slight difference of the intensity between the two spectra,

which may result from the different experimental environments. Most of the peaks are found to be iron lines following identification of the emission line based on the atomic properties of the database of the National Institute of Standards and Technology (NIST) and the Harvard-Smithsonian Center for Astrophysics (CFA) [28, 29]. Background area of the emission spectra was subtracted for the analysis.

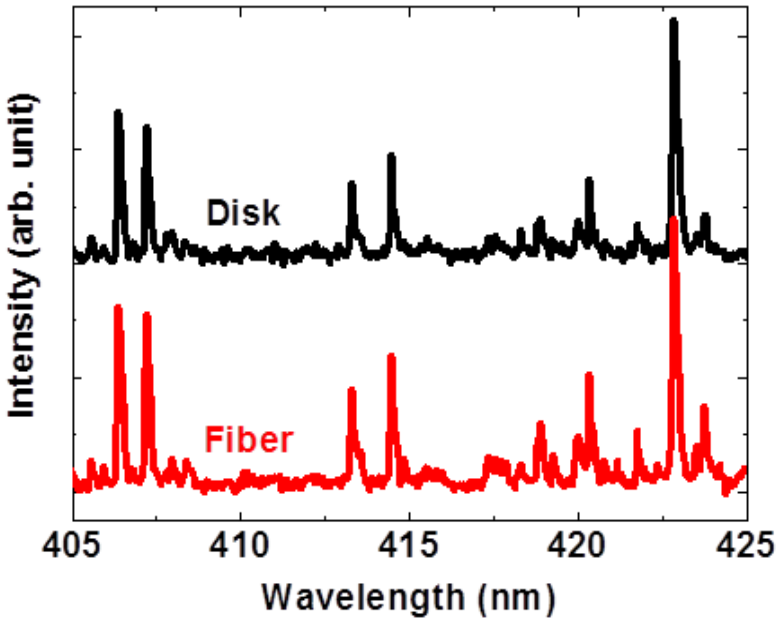

Figure 5-3 Emission spectra generated from the irradiated spheroidal graphite cast ion by the disk and fiber lasers

5.3.1.1. Determination of the electron temperature

In the case of the laser induced plasma, the electron temperature is obtained under an assumption of the local thermodynamic equilibrium (LTE). In this equilibrium, the collision process of the plasma particles is more important than the radiation process since

the radiation density of the plasma is below blackbody level. The collisional population and the velocity of particles is described by the Maxwell-Boltzmann distribution under the equilibrium [70]. Therefore, the electron temperature is derived from the Boltzmann distribution, which describes the population of the excited state.

There are two ways to determine electron temperature: the Boltzmann equation and the Saha-Boltzmann equation. The former method was used in this study since emission lines of successive ionization levels in the same species were not observed in the emission spectra [71]. A special type of the method, called the Boltzmann plot was selected for improving accuracy instead of the Boltzmann two line method because this plot calculates the temperature from the fitting of the multiple emission lines of the observed species rather than only two lines [35, 36]. The Boltzmann plot method is expressed as follows [36]:

$$\ln \frac{I_{mn}\lambda_{mn}}{A_{mn}g_m} = \ln\left(\frac{Nhc}{Z}\right) - \frac{E_m}{kT} \tag{5.1}$$

where m is excited level, n is lower state level, λ_{mn} is wavelength, A_{mn} is transition probability, and g_m is degeneracy of the excited level. Z, E_m, k, T, and h are the partition function, upper state energy level, Boltzmann constant, excited temperature, and Planck's constant, respectively. In this equation, I indicates the intensity of the emission line, given by the equation below assuming no self-absorption [36].

$$I_{mn} = \frac{1}{4\pi}\int n_m(x) g_m A_{mn} \frac{hc}{\lambda_{mn}} dx = \frac{1}{4\pi} N_m g_m A_{mn} \frac{hc}{\lambda_{mn}} \tag{5.1}$$

where the symbols are identical to those described in equation (5.1). Equation (5.2) is valid since the existence of the self-absorption has not been observed in the emission spectra based on the criteria [71, 72]. Spectroscopic parameters of the Fe I emission lines used to calculate the electron temperature are summarized in Table **5-1** [28].

Figure **5-4** shows the estimated electron temperature results, including an inset showing a fit using a Boltzmann plot from the neutral iron emission lines. The emission lines, which have considerable differences of the excitation energy level, are chosen because the temperature calculation using emission lines with the small gap of the excitation energy can cause significant fitting error in the Boltzmann plot [71]. It should be noted that the determination of the electron temperature can include ~15% uncertainty due to the transition probabilities and the measured line intensities used in the Boltzmann plot.

Table 5-1 Spectroscopic parameters of the Fe I emission lines used to calculate the electron temperature

Wavelength λ (nm)	Transition Probability A (s^{-1})	Statistical Weight		Transition Energy Level (cm^{-1})	
		g_n	g_m	E_n	E_m
383.4	4.5×10^7	7	5	7728.06	33801.57
384.0	4.7×10^7	5	3	7985.78	34017.10
385.6	4.6×10^6	7	5	415.93	26339.69
388.6	5.3×10^6	7	7	415.93	26140.18
389.6	9.4×10^6	3	1	888.13	26550.48
393.0	1.6×10^6	5	7	704.00	26140.18
396.9	2.3×10^7	9	7	11976.23	37162.74
400.5	2.0×10^7	7	5	12560.93	37521.16
407.2	7.7×10^7	5	5	12968.55	37521.16

As a result, the electron temperature of the disk laser system is estimated to be 6480 ± 14 K and that of the fiber laser system is 6350 ± 64 K. Since the temperature difference is so small compared to the absolute values, the electron temperature of both systems is considered to be similar. These similar temperatures are well correlated with the spectrum profile of the emission lines, shown in Figure 5-3, since the kinetic energy of the particles and its velocity distribution at the temperature causes the collisional transition, generating emission lines, which is in line with the reason for the electron temperature being equal to the electron kinetic temperature [71].

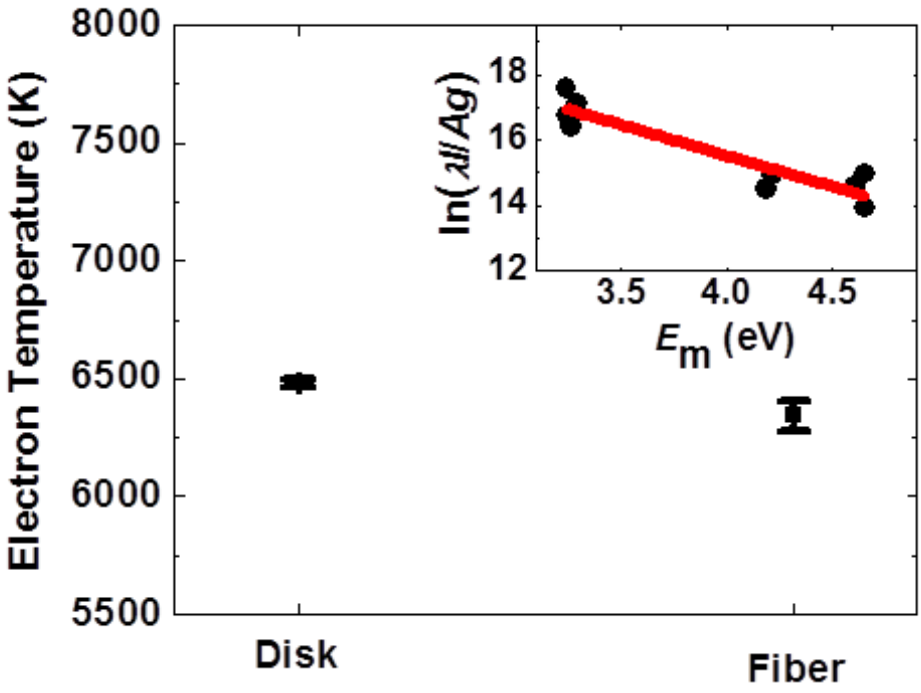

Figure 5-4 Electron temperatures of the plasma induced by the disk and fiber lasers, analyzed from neutral iron emission lines. Inset shows a fitting result using a Boltzmann plot of the spectral data induced by the fiber laser.

5.3.1.2. Determination of the electron number density

The 381.58 nm Fe I emission line was chosen to evaluate the electron density since it has considerable line broadening. In the case of laser induced plasma, Doppler broadening and Stark broadening are the underlying mechanisms responsible for the line broadening [41, 73]. The contribution of the Doppler broadening caused by random thermal motion is estimated using a relation provided by Gornushkin et al [74]. The estimated result, 0.0029 nm, indicates a negligible contribution to the broadening, which agrees with the results of other studies [35, 73]. Therefore, Stark broadening is the most dominant factor for the line broadening and is expressed by the following equation [75]:

$$\Delta\lambda_{1/2} = 2\omega\left(\frac{N_e}{10^{16}}\right) + 3.5A\left(\frac{N_e}{10^{16}}\right) \times \left[1 - 1.2{N_D}^{-1/3}\right] w\left(\frac{N_e}{10^{16}}\right) \quad (5.3)$$

where $\Delta\lambda_{1/2}$ is FWHM, ω is the electron impact width, A is the ion broadening parameter, N_e is the electron number density and N_D is the number of particles of in the Debye sphere. The first term of equation (5.3) represents the electron broadening effect, whereas the second term indicates the ion broadening effect. However, since the ion broadening effect is so small, its contribution can be neglected [35, 73, 76]. This allows equation (5.3) to be reduced to the form below:

$$\Delta\lambda_{1/2} = 2\omega\left(\frac{N_e}{10^{16}}\right) \quad (5.4)$$

Electron density was determined using this reduced form. The Stark coefficient ω was referred to the experimental results [77, 78]. The broadened line basically includes the instrumental width, 0.08 nm, which is considered in the fit of the broadened profile

achieved with the Lorenz functions [35, 79]. The electron density includes ~10% uncertainty for the width measurement and electron impact width.

Figure **5-5** reveals that the determined plasma electron densities of both systems are similar: The plasma electron density is $6.32 \pm 0.3 \times 10^{16}$ cm^{-3} in fiber laser system, and the plasma electron density is $6.11 \pm 0.4 \times 10^{16}$ cm^{-3} in the disk laser system. This is correlated with the estimated electron temperature and the observed spectrum profiles in the previous sections. Since the radiation density of the laser induced plasma is below the blackbody radiation, independent of the number density of the particles, the electron density determines the kinetic energy, which generates collisional transition [70].

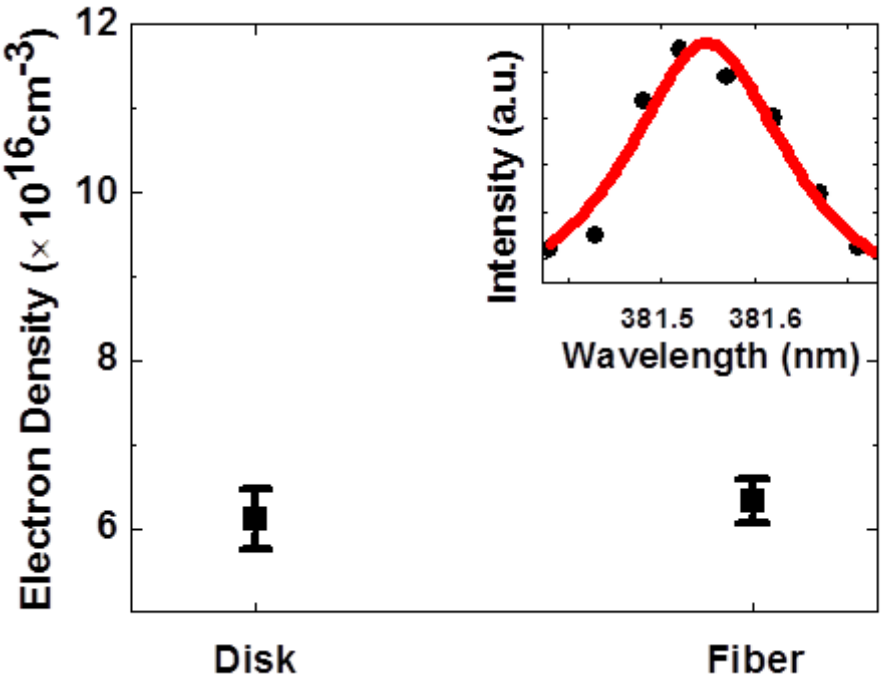

Figure 5-5 Electron density of the plasma induced by the disk and fiber lasers, analyzed from the 381.58 nm Fe I emission. Inset shows a fitting result using Lorentz function on the spectral data induced by the fiber laser.

5.3.1.3. LTE considerations

Characterizing the plasma in terms of electron temperature and density, we assumed the laser induced plasma is LTE, in which the collisional process dominates the radiation process. Therefore, the validity of the LTE must be satisfied with the McWhirter conditions below [70]:

$$N_e cm^{-3} \geq 1.6 \times 10^{12} T^{1/2} \Delta E^3 \quad (5.5)$$

where ΔE(eV) is the energy gap between transition, N_e is the electron density and T (K) is the electron temperature. Since the left of the equation indicates the lower limit, the ΔE, 3.23 eV, is selected from among the emission lines for the Boltzmann plot. Considering all values, it ensures the validity for both systems.

5.3.1.4. Energy absorption by the plasma

The energy absorption by the plasma is mainly caused by either Inverse Bremsstrahlung (IB) absorption or photo-ionization (PI) process [35]. In this study, the IB is considered to be the primary absorption mechanism since the effect of the PI is negligible in infra-red lasers and both lasers' wavelengths are 1030 nm and 1070 nm, respectively. In other words, the photon energy of the laser beam is too weak to have the considerable contribution that it has in an ultra violet laser [41, 80]. Additionally, the laser induced plasma via IB absorption typically has an electron density in the range of 10^{15} to 10^{17} cm^{-3} [2]. Indeed, as calculated in the previous section, the estimated electron number densities in both systems, 6.32×10^{16} cm^{-3} for the fiber laser and is 6.11×10^{16} cm^{-3} for the disk laser, are in line with the previous study [2].

The IB absorption consists of electron-neutral IB (e-n IB) and electron-ion IB (e-i IB). While the e-n IB forms initial plasma, once the air is ionized, despite a small fraction, the e-i IB mechanism plays an important role [35, 81]. Both mechanisms involve photon energy absorption by free electrons. The absorption coefficient via free electron is expressed as follows [35]:

$$\alpha_{\mathrm{IB}}(\mathrm{cm}^{-1}) = 1.37 \times 10^{-35} \lambda^{3} \mathrm{N}_{\mathrm{e}}^{2} \mathrm{T}_{\mathrm{e}}^{-1/2} \tag{5.6}$$

where λ(μm) is wavelength of the laser photon, N_e is the electron number density and T_e is the electron temperature [40, 41].

Using equation (5.6), the IB absorption was estimated in both systems. The coefficient in the fiber laser is ~7.52×10^{-4} cm^{-1}, whereas the coefficient in the disk laser is ~6.96×10^{-4} cm^{-1}. In equation (5.6), λ^3 and N_e^2 dependence determine the IB absorption coefficient. N_e^2, particularly, causes a slight difference of the coefficients as calculated in the previous section. However, considering all uncertainties of the electron temperature and the electron density, energy absorption by the plasma in both systems may not have much difference.

5.3.2. Penetration Characteristics

Penetration characteristics formed by re-solidification were investigated to study the role of the attenuated laser beam caused by plasma absorption. Figure 5 shows optical microscope images of the samples irradiated by the disk and fiber lasers. In power densities, comparisons of the samples, from 3.1×10^9 W/m^2 to 9.3×10^9 W/m^2, show that the overall

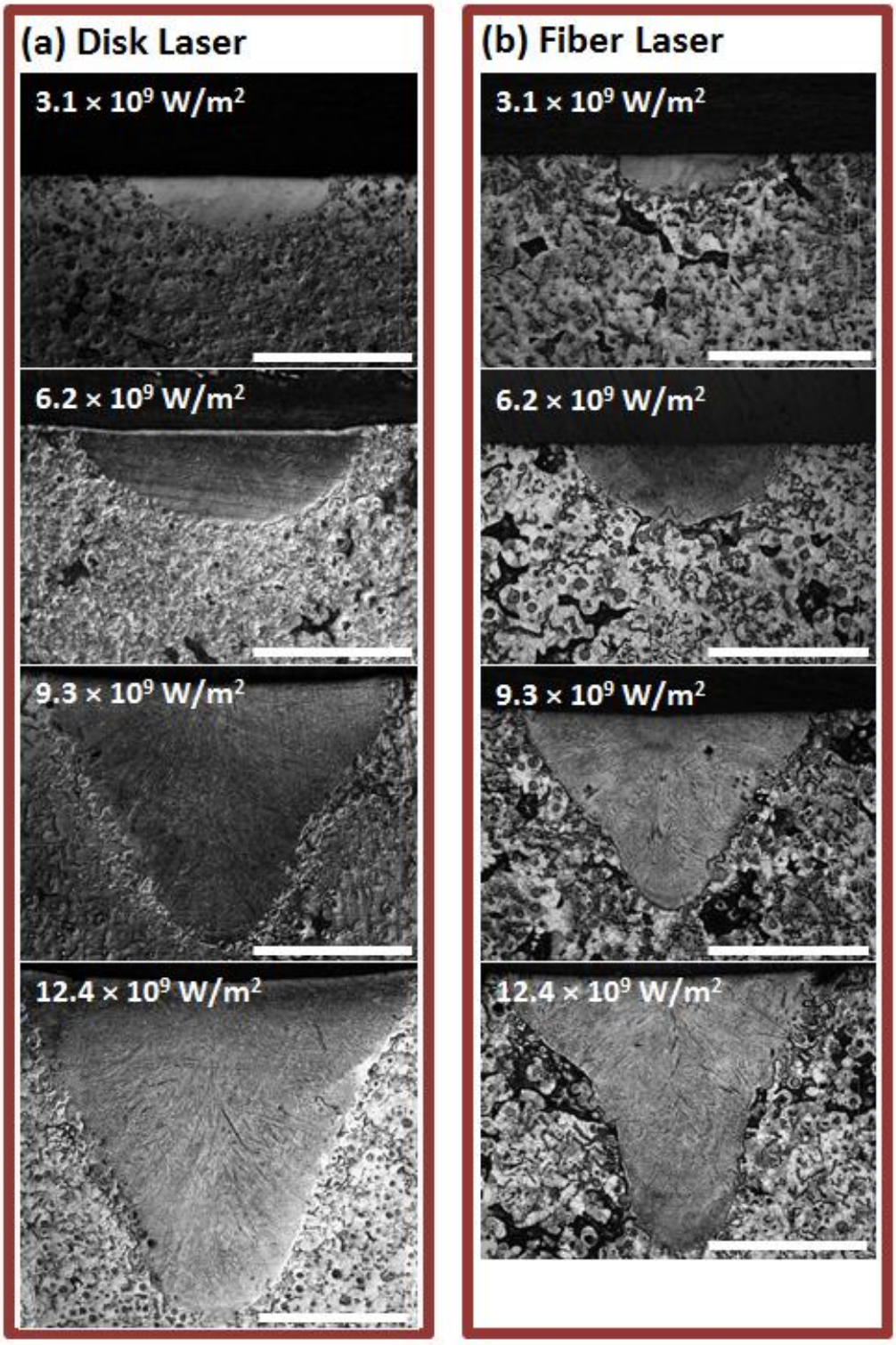
(a) Disk Laser
3.1 × 10⁹ W/m²
6.2 × 10⁹ W/m²
9.3 × 10⁹ W/m²
12.4 × 10⁹ W/m²
(b) Fiber Laser
3.1 × 10⁹ W/m²
6.2 × 10⁹ W/m²
9.3 × 10⁹ W/m²
12.4 × 10⁹ W/m²

Figure 5-6 Optical microscope images of the spheroidal graphite cast iron samples irradiated by the (a) disk and the (b) fiber lasers under the bead-on-plate conditions.

bead shapes caused by re-solidification from the molten pool is quite similar between the two systems. However, in the 12.4 × 10^9 W/m^2, the feature is somewhat different; the slope of the side wall changes abruptly in the case of the fiber laser. This may be due to the difference in the beam modes: Gaussian for the fiber laser and top hat for the disk laser. The Gaussian beam has higher intensity at the center position compared to the top hat mode. In other words, the energy contribution of the high peak can cause an abruptly narrow penetration zone since, due to the large beam diameter, effective power density is too low under the other three conditions to produce the feature.

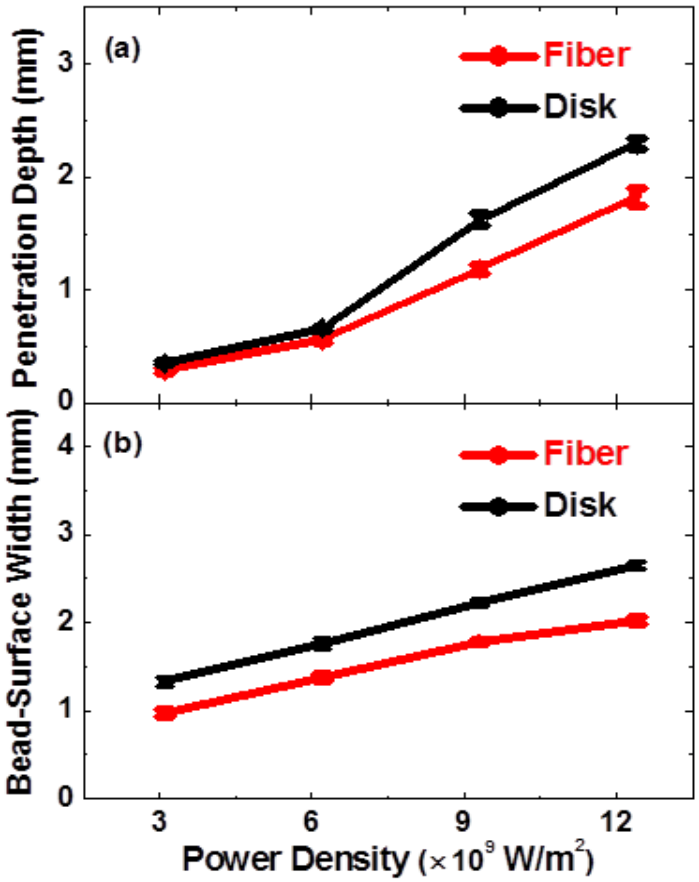

Figure 5-7 Measurements of the (a) penetration depth and (b) bead-surface width from the optical microscope images according to laser-power densities.

According to measurements of the penetration depth and bead-surface width from the optical microscope images, as shown in the Figure **5-7**, the penetration profiles have different features under conditions of high power densities. In Figure 6 (a), the difference of the penetration depth between the two laser systems in high power density conditions is larger than that of the low power density conditions. In Figure 6 (b), the difference in the bead-surface width between the two systems at the $12.4 \times 10^9\,W/m^2$ is the largest compared to those of the other three groups. Moreover, the bead surface width of the disk laser is slightly larger than that of the fiber laser across the entire conditions. The two possible reasons for this result are as follow. Firstly, the beam divergence angle of the fiber laser is 200 mrad, which is a little larger than that of the disk laser, 179 mrad. This leads to larger energy absorption from the disk laser to the material, and thus the transferred energy generates larger molten pool. Secondly, the efficient heat dissipation by the cavity design of the disk laser can affect high power conditions. Since the thin disk is mounted on the heat sink, heat dissipation into the heat sink is well maintained. This allows uniform radial temperature distribution across the pumped disk causing homogeneous beam propagation [27].

5.4. Conclusion

Characteristics of the energy transfer of the fiber laser and the disk laser are investigated to provide users with insight into which laser might be more suitable for a

given application. In both systems, IB absorption by the plasma is found to be comparable. To estimate this energy absorption, the electron temperature and electron density are estimated using the Boltzmann plot method and the Stark broadened Fe I 381.58 nm, respectively. The electron temperature in the disk laser and fiber laser are estimated to be ~6480 K and ~6350 K, respectively, whereas the electron densities are estimated to ~6.11 × 10^{16} cm^{-3} for the disk laser and ~6.32 × 10^{16} cm^{-3} for the fiber laser, respectively. The electron temperature and the electron density are thought to be similar, considering the uncertainties of the spectral data and the experimental errors. Two estimated plasma properties are correlated with the acquired spectrum profiles induced by the fiber and disk lasers. In other words, the peak positions were almost the same in the emission profile since the kinetic energy by the electron density at the equilibrium temperature causes the collisional transitions, which determine the emission profiles.

Penetration characteristics, examined at various power densities for each system, revealed that the disk laser produces a slight deeper penetration than the fiber laser in the higher power densities. This may results from the beam divergence and the homogenous thermal management by the cavity design. Additionally, the shape of the side walls in the 12.4 × 10^{9} W/m^{2} is dependent on the beam mode. Based on the observed features, the performance of the disk and fiber lasers, in terms of energy transfer, are comparable. However, in high power densities, the disk laser has slightly deeper penetration.

CHAPTER 6

CONTRIBUTIONS, LIMITATIONS AND FUTURE WORK

6.1. Contributions

This study offers contributions to the laser material processing, particularly focusing on 1) the detection and classification of the welding defects for the development of the quality monitoring system, 2) understanding of the defects formation mechanism, and 3) characterization of the energy transfer in the fiber and disk lasers, through the spectroscopic measurements of laser induced plasma. The most important contributions are listed below:

- ***Defect detections generated in the CO_2 laser material processing***: Several weld defects generated in laser processing of multi-coated material are successfully monitored using the optical emission spectroscopy. In the lap welding of sheet metals (a realistic set-up used in the Toyota production line), the small gap between the sheet metals induces several detrimental defects, specifically, bead separation, underfill, burn-through, and pin-hole. Those defects induced by the small gap are not detected using the conventional monitoring techniques. For the first time, the

defects generated in the lap joint welding of multi-zinc coated steels are detected using one experimental set-up, OES. In the zinc coated steels, zinc is the key element that induces the defects because of the difference between the boiling temperature of zinc (1180K) and the melting point of iron (1811K). Hence, the defects are detected by tracking the Zn emission lines. Prior to the monitoring of defects, the spectroscopic properties of emission lines in each constituent of the target material are investigated. Considering the transition probability and the relative intensity of the emission lines of each constituent, the Zn I line (481.1nm) is found to be suitable as a monitoring target. The temporal evolutions of the Zn I line show the evident features that are correlated with those weld defects. The defects are successfully detected using four features, the average of the Zn I relative intensity, the standard deviation of the Zn I relative intensity, the electron temperature and the line width of the emission lines.

- ***Investigations for the difference of spectra profiles:*** For the first time, a comparison of spectra characteristics in two plasmas induced by CO_2 laser and disk laser are performed using the zinc coated steel. Because of the short wavelength of this disk laser (1.03 μm), compared to that of the CO_2 laser (10.6 μm), the emission spectra show different profiles. Through the spectral analysis, the electron temperatures are calculated using Boltzmann plot method to explain these different profiles. The results by this method show the two different electron temperatures, ~4400 K and ~7700 K, respectively. These temperatures difference indicates the dissimilar characteristics of two spectra. Fundamentally, the emission line arises

from the energy gap between the excited level and the ground level in the transition for a two-level atom. The energy gap required for the transition is induced by the kinetic energy of the electron. The calculated temperatures above explain the amount of the kinetic energy induced by the energy absorption by the plasma. Therefore, the different electron temperatures indicate the different energy distribution between the collisional particles forming the plasma. For this reason, the spectra show dissimilar profiles.

- ***Defect classification using the Support Vector Machine***: As described above, the Zn line detection technique works for the CO_2 laser welding but not for the disk laser. In order to obtain promising results for both defect detection and defect classification in the disk laser welding, the SVM, a statistical approach, is used for the spectral data analysis using the richness of the spectra data. The richness is a major benefit in the use of the optical emission spectroscopy because the spectrometer can resolve and distinguish each spectral line of the constituents of target materials. Three classes are defined to classify the defects. Using the features extracted in the Fe I line, the spectra data sets are trained. Based on the trained values, the multi-classification tests are performed using the cross validation method. In order to prevent contamination of the data, training sets and test sets of the spectra are separated. Consequently, the overall classification rate is found to be ~95%.

- ***Investigation of the defect formation mechanism using the mathematical simulation***: For the first time, the mechanisms of defect formation in the laser material processing of the overlapped zinc coated steels are simulated using the 3-D self-consistent model. For the mechanism induced by the zinc coating, the zinc properties are embedded at the position where the coating is located. Kinetic theory based on the momentum change is implemented for the recoil pressure. The simulated results show that the vaporization of the zinc coating induces the increased hydrodynamic momentum, which increases the flow velocity. This increased velocity leads to the ejection of the liquid metal and the temporary temperature drops that cause the reduced recoil pressure. Consequently, the reduced recoil pressure leads to the temporal fluctuation of the L/V interface, since the cavity formed by the L/V interface moves up and down depending on the recoil pressure. Additionally, due to the vaporization pressure in the zinc layer, the L/V interface is found to be pushed backward, and hence this leads to the change of the molten flow at the position of the zinc layer.

- ***Experimental validations for confirming the simulation resutls:*** Several experimental validations are performed to confirm the simulation results. For the validation, the reflective topography is used to measure the flow velocity of the two cases. The velocity of the liquid metal at the side wall of the L/V interface cavity in the ZC case is found to be almost double that of the ZA case. Moreover, the processed sample is cut along the scanning direction to validate the pushed L/V interface. At the initial area of the laser irradiation, the existing porosity near the zinc layers confirms that the simulation result is reasonable.

- ***Characteristics of the energy transfer in the fiber laser and the disk laser:*** Characteristics of the energy transfer in the two different lasers are identified to provide users with insight into which laser might be more suitable for a given application. In both systems, IB absorption by the plasma is found to be comparable. To estimate this energy absorption, the electron temperature and electron density are estimated using the Boltzmann plot method and the Stark broadened Fe I 381.58 nm, respectively. The electron temperature in the disk laser and fiber laser are estimated to be ~6480 K and ~6350 K, respectively, and the electron densities are estimated to be ~6.11×10^{16} cm^{-3} for the disk laser and ~6.32×10^{16} cm^{-3} for the fiber laser, respectively. The electron temperature and the electron density are found to be similar, considering the uncertainties of the spectral data and the experimental errors.

- ***Investigation of penetration characteristics***: Penetration characteristics examined at various power densities for each system show that the disk laser produces a slightly deeper penetration than the fiber laser in the higher power densities. This may result from the beam divergence and the homogenous thermal management by the cavity design. Based on the observed features, the performance of the disk and fiber lasers, in terms of energy transfer, are comparable. However, in high power densities, the disk laser has slightly deeper penetration.

- ***Commercialization of this research:*** A *commercialization* process of this research has been achieved. Currently, much valuable research is ongoing within the community of the University of Michigan. A commercialization of the research was proposed as a means of stimulating the local economy through the valuable research. This commercialization process was initiated from the IUCRC project supported by NSF. The business plan was then built through the MBA course (FIN 629) offered in Ross School of Business. This plan covers the technology review and Intellectual Property (IP) review prior to the entry into the real market. In addition, the realistic market size was professionally estimated. Based on the reviews, a company strategy and a development plan were established. This business plan enableed the startup of SenSigma LLC. This entire process can be a guideline for engineers to broaden their insight into the realistic research.

6.2. Limitations and Future work

This works has some limitations. In the application of the machine learning algorithm, the classification rate needs to be increased. Currently, the overall classification rate is ~95%. However, for the quality assurance, the classification rate should reach 100%. Most of the errors result from the similarity of features between the classified classes because of the non-linearity of the defects. Therefore, more rigorous feature selections are

required. At the same time, the dimensions of the training sets need to be optimized. Currently, the emission lines of interest are selected based on physical properties such as relative intensity and transition probability. Even though the selections (feature extractions) are justified based on the physical reason, the dimension of the training sets need to be optimized using mathematical techniques such as class scatter mean for the efficient computational cost of real time monitoring.

In the simulation study, a limitation is that the plasma-laser interaction is not considered. The photon energy transfer is closely related with the plasma behavior because the energy of the laser beam is attenuated by the plasma. Therefore, the plasma blocks a considerable amount of energy transfer to the target material. Even though IB absorption coefficient can be estimated from the spectral line for the overall estimation of the absorbed by the plasma, only considering this coefficient cannot predict the realistic energy transfer caused by the plasma located inside the material. A model of plasma-laser interaction can estimate realistic energy transfer.

This OES has many potential applications in other laser material processes or in fusion welding methods including arc welding and hybrid welding because these processes generate plasma, which is the target of the OES. That is, in all the processes including plasma, this OES can be applicable. In the spectroscopic study, various applications must be explored further to realize the advantages of the OES. Since this novel method enables constituents analysis, other processes such as dissimilar materials welding and laser micro machining of multi-layer substrate can confirm its advantage.

APPENDIX A.
BUSINESS PLAN FOR RESEARCH COMMERCIALIZATION

This appendix presents a commercialization business plan. This business plan is established by a team of five people (Ben Glaze, Karan Goyal, Tejas J, Seung Hwan Lee, Marcus L. Pollack), who includes the author as a Project Investigator (Project Investigator: Jyoti Mazumder, Seung Hwan Lee), through the Financial 629 course (Professor: David Brophy) that is offered in the Ross business school. This plan covers the technology review and Intellectual Property (IP) review prior to entry into the real market. In addition, the realistic market size is professionally estimated. Based on the reviews, a company strategy and a development plan are built. This business plan has enabled the startup of SenSigma LLC. (www.sensigmallc.com), through the support of the Michigan government and the office of the Technology (University of Michigan).

A.1. Introduction

In the North American Automotive industry alone, scrap costs related to automotive body welding issues are estimated at $280M, and this is projected to grow to $340M in five years. Our company has a technology solution to enable a practical elimination of this waste and is further positioned to expand to other manufacturing industries and geographies facing similar challenges.

Various types of welding defects are serious problems concerning quality assurance in welding production lines. When welding components, a small defect in the weld can lead to scrapped parts, inferior quality and requirements to over-design welded joints to compensate for potential defects. Common design issues include use of additional sealants in the automotive industry and use of more numerous or larger welds than otherwise ought to be required. These factors result in increased manufacturing costs, lost product value and additional product weight.

A.2. Technology Review

The technology involved with the weld monitoring system enables use of moderately priced, standard equipment to be applied to on-line monitoring of weld quality. The current lab setup adds a spectrometer (readily available, moderately priced equipment) to a standard PC with the weld monitoring system's proprietary algorithm, which could be embedded in a software product, for interpreting the spectrometer signal. Therefore, quality inspection is transformed from a post-welding step with related cycle time and delays in information availability to an integrated process with the weld that eliminates cycle time and information delays.

Specifically, the monitoring system works using a spectrometer or photo diode to analyze the radiation spectrum emitted during the welding process. The optical characteristics are identified on each kind of defect, enabling the weld quality is monitored in real time. A key aspect of the technology comprises the way to analyze the measurement signals and a system which uses this data to identify welding defects to operators in production line. Using a spectrometer, it is possible to choose the radiation wavelengths of

interest and then compare the signal properties with those from various types of defects. For commercialization, it is anticipated that a much less expensive photo diode can be used in place of the spectrometer.

Feasibility has been demonstrated in a lab setting, as applied to a few sample materials and defects. Further development will expand the types of materials and types of defects which can be detected. Additional development will also be required to demonstrate feasibility in a manufacturing environment. Table A- 1 below shows the technical progress and plan.

There are three primary limitations to the technology. The first is that the technology applies only to weld processes with a plasma cloud surrounding the weld. This is a common feature for most welding methods, although the spot-welding processes, which are common to the automotive industry, do not have this feature. The second challenge is in the requirement for precise location of the spectrometer sensor relative to the weld. This requirement may be addressed by integrating the sensor with the welding equipment. The third limitation is that the software to identify quality issues will require some level of customization to specific weld processes based on materials used and defects of concern. This limitation may be addressed either by establishing a suitable database of common settings or by providing initial setup services along with installation of the system to ensure its correct function. Currently the technology has been developed for a limited number of defects, but with further research, a larger number of defects could be analyzed.

Table A- 1 Technical Progress and Plan

Type of Welding	Defect	Sept	Oct	Nov	Future
Laser welding	Under-fill				
	Burn-through				
	Bead separation				
	Small hole				
	Other				
MIG welding	Feasibility check test				
	Contamination				
	Under-fill				
	Burn-through				
	Bead separation				
		Done	**In-Process**	**Future**	

A.3. IP Review

The monitoring of fusion welding can be carried out by several methods such as acoustic emission and Optical Emission Spectroscopy (OES). Our topic is classified as a branch of OES. Within that area, the most important aspects are the position of the sensor, the spectral range of interest and the method of analyzing the spectral information. The company's patent (20080210674) is described in detail in Appendix 1.

A.3.1. Prior Art

Our group has conducted an informal patent search and found at least ten patents pertaining to laser welding monitoring. Some of the key patents include 5681490 by Dale Change, filed in 1995, which claims to use sensors to capture multiple aspects of the welding process including the light and heat claims in our patent and extending to sound,

gas, smoke, vapor and particles. Another similar patent was issued in 1999, which further describes how to interpret signals from a laser welding process (5961859). Patent 6998572, filed in 2002, clearly uses a much different detection process including mirrors to read light energy, but also claims to have the ability for software to alter the welding specifications during the process, which could interfere with our claim regarding the welding alteration process. The claims also indicate a different approach to analyzing the signals. This patent is assigned to Matsushita Electronics.

In addition to the patents, a competitive solution is currently available from Prometec, a German company. Although a prior art search did not uncover any relevant patents held by Prometec, the Principal Investigator found the technology somewhat dissimilar from publicly available information. Nonetheless, existence of a similar concept in the market could be a persuasive argument towards a claim that the present technology is "reasonably obvious".

A.3.2. Freedom to Operate

The patents described above are a sample of several in the field which were identified in an informal search. Patent 6998572 may limit freedom to operate as it covers the basic concept behind the current technology, but is not explicit about application methods. Patent 6339915 covers positioning of the sensor in a system similar to our technology, and hence may limit freedom to operate. Patent 6596961 covers a feedback control technology similar to our claim to be able to use the monitoring system input as part of a control system. Patent 6060685 may also impair freedom to operate since it mentions averaged-intensity, a similar concept to our signal analysis approach. It did not include factors like physical, statistical information, the ratio of the intensities or electron

temperature and it did not mention specific behavior of the signal, potentially limiting the impact of this patent.

The basic hardware and software required to implement the proposed weld monitoring technique includes a laser light source, a photo diode and a computer with basic data acquisition and analysis capabilities. All of these required items are commercially readily available and do not represent a significant freedom to operate limitation.

A.3.3. Ownership / Licensing Issues

There are currently two inventors on the relevant patents; Jyoti Mazumder and Seung-Hwan Lee and the patents will be clearly assigned to the University of Michigan. Toyota (NSF IUCRC) sponsored the research, although this sponsorship does not entitle Toyota to ownership of the intellectual property generated. We have not currently made any public disclosure, other than the filing of the patent, about our technology.

If there is a successful licensing effort, the University of Michigan would be able to claim the rights to the technology.

In addition to the patent issues discussed above, another intellectual property aspect of this technology is the know-how developed to translate the signals from the measurement system into useful data. This is currently embodied as a calculation algorithm that is modified based on the materials being welded and types of defects identified. Further development will build on this application-specific knowledge and offers another potential avenue for protecting and monetizing the intellectual property. Given the current patent situation, it would be risky to further disclose application-specific knowledge through

patents or other disclosures as these details offer potential to be used as trade secrets that enable monetization.

A.4. Market Review

Broadly speaking, the potential end-user market for the weld monitoring systems includes manufacturers in a wide variety of industries, such as automotive, ship building, construction equipment, aerospace, medical devices, and oil and gas equipment. Original Equipment Manufacturers are obviously potential end-users, but it should also be noted that the supply base is involved in many of the component and system level manufacturing processes, with OEMs often only responsible for final assembly and hence with limited use of welding processes at many of their assembly sites. The technology has been proven to work for laser welding and is in early stages of proof for MIG welding, but should be applicable to any form of welding with a plasma gas.

It will be possible to sell a weld monitoring system directly to end users, but these systems could also be sold to integrators, which are companies supplying welding equipment to these end users. Additionally, material suppliers are often in a position to advocate for improved fabrication technologies or to bundle fabrication methods with their materials. In some cases the material manufacturers extend their business to deliver simple components which may make a weld monitoring system relevant to their operations as well.

A.4.1. Segmentation

The total market space for laser welding can be sub-divided into two main segments based on the needs and priorities of the potential customers. The first segment comprises those which are primarily cost focused such as the automotive sector. The second segment focuses on high quality and dimensional accuracy. These include the

aerospace and medical equipment applications. While these are potentially more attractive and profitable areas to be working with, discussions revealed that they may not be the easiest to penetrate without significant proof of success elsewhere.

The market for Laser applications in general is experiencing a significant growth of about 9% year on year, according to data provided by *"Industrial Laser Solutions"*. From 1970 through 2006 the compound annual growth rate (CAGR) for industrial laser unit sales revenues is 19.9%. In 2006, industrial laser system sales surpassed the $4.7 billion level. This was estimated to further increase to $5.14 billion in 2007. Laser Welding, which is the target market for this technology accounts for 12% of the total Laser equipment sales. This is increasing at the same rate as the rest of the Laser market. As for the worldwide spread, Japan accounts for 31% of the worldwide market, with North America and Europe each accounting for 27%. Asia is a fast growing market but currently accounts for 10% of the worldwide market.

The primary target market for this technology is the automotive industry. These include the OEMs and Tier I suppliers. Based on past experiences with similar projects, it has been found that these firms are more than ready to implement the technology as long as they are convinced of immediately perceivable reductions in 'cost' and delivery time, with a low initial investment. After speaking with an engineer at a major US OEM, we learned that the welding monitoring process is still largely manual and relies on "destructive testing," offering a significant opportunity to enter into a "blue ocean market." Adoption in this market segment can be rapid, with many automotive suppliers preferring to replace traditional fasteners and rivets in permanent joints with Laser welding to reduce overall weight. There is a trend of switching from spot welding to laser welding in the welding

manufacturing process that will significantly benefit our technology, as it was developed for laser welding originally. Although one OEM said they currently only used laser welding on the roof of the automobile, there was significant discussion about using laser welding in other processes as it is faster and stronger if monitored correctly. Potential customers include US-based OEMs include Chrysler, Ford and General Motors. Foreign-based automotive OEMs with manufacturing in the USA include Toyota, Nissan, Hyundai, Honda, and BMW. Their supply base includes companies such as Gestamp which provide Body-In-White systems to OEMs.

Having proved the technology and its benefits in the automotive sector, the next step would be to aim at the aerospace or ship building industries. Since the aerospace industry takes a much more conservative approach to technology adaptation, it would be a lot easier to penetrate this market space once having proved results in other applications such as automotive.

A.4.2. Market Entry

The most significant pain point in the market currently is the welding of automotive sheet metal. Scrap rates for automotive "Body In White" (i.e. bare body structures) has been found to be as high as 1%, much of which is driven by quality concerns over laser welded joints. Additionally, significant tooling expenses are incurred to support spot welding, which requires a tool to touch both sides of the joint, whereas methods such as MIG or laser welding require tool accessibility from only one side. Since spot welding is considered more robust, it is often favored. The tool accessibility requirements can also significantly limit design flexibility, particularly in the face of conflicting requirements for stringent safety performance and reduced weight to maintain fuel economy. It also should

be noted that use of spot welding on certain exterior pieces also forces use of additional exterior trim pieces to cover the poor aesthetics of a spot welded joint. A visible example of this is the plastic trim pieces often running the length of the roof of a car on both sides.

Exasperating these challenges is the significant profit pressure on the industry due to declining demand and increasing quality expectations from customers. As a result, the industry is in desperate need to address key pain points to gain cost and quality advantages. The level of distress currently is such that the survival of certain OEMs is in question if they cannot make significant progress in the near term.

It can be noted that the team is currently pursuing discussions with Ford, General Motors, Chrysler, Arvin Meritor and Dura Automotive to better establish specific opportunities. Discussions with them have revealed that they are already 'actively' seeking Laser weld monitoring systems. They say many such monitoring systems have already been tried out but none of them worked to their satisfaction. These are encouraging results which could give us an indication that there is a definite pain in the market and companies are on the lookout for technologies to solve this problem.

A.4.3. Value Proposition

In summary, our value proposition is to reduce manufacturing costs, reduce liability from product default, and enable improvements to product quality, reductions to weight and increased fuel economy. The key component of our sales thesis will be convincing our customers that the switching costs and learning curve costs of implementing our product will be beneficial in the long run.

A.4.4. Blue Ocean Market Description

To identify a Blue Ocean market approach, the weld monitoring system is compared to possible alternatives. Common current practices are destructive testing, where a small sample of production parts are thoroughly examined by pulling welds apart and checking for strength, "open loop" systems where no validation of final quality is included, and non-destructive testing such as x-ray inspection. Alternate in-line systems include the present weld monitoring system, a monitoring system from Prometec and acoustic emission monitoring systems which are currently under development. Key factors include price, response time, accuracy, sampling of parts, expected re-work needs, risk of errors in parts at the end-of-line, flexibility of materials and ability to add on to existing manufacturing equipment. A summary of the Blue Ocean market analysis is shown in Figure A- 1 below. The closest competitors are Prometec's solution and acoustic emission. Our offering will be most similar to Prometec, but differentiated based on much lower price, greater material flexibility and the ability to add on to existing manufacturing equipment. Acoustic emission testing is expected to be capable of a similar offering as well, but is anticipated to be at a higher cost, have lower accuracy resulting in greater risk of end-of-line errors and have lower material flexibility.

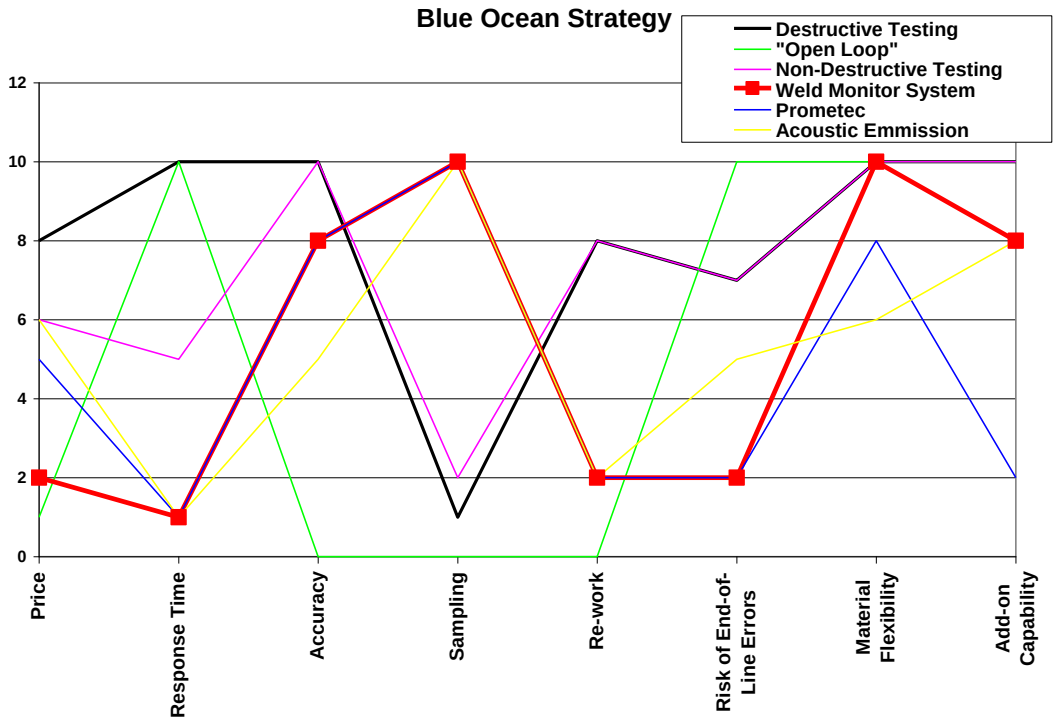

Figure A- 1 Blue Ocean Strategy for Weld Monitoring System

A.4.5. Market Size

The market is treated as the automotive body welding market, which is the first targeted segment, and the broader welding equipment and supplies market.

Automotive Welding

The main reasons for acceptance of Laser welding in auto industry as a replacement of spot welding are due to the facts that Laser welding is easy to automate, has higher welding speeds and produces better welds. It also provides longer continuous welds that provide greater strength and can greatly reduce idle times between welds. Laser welding can help engineers make better trade-offs between weight and strength by reducing

the size of the flange attached to the weld. In spot welding it can be as big as 15 mm. Laser welding can cut that by about 50 percent.

Moreover in spot welding, the lower electrode sometimes needs an access hole to reach the lower part of the sheet metal to complete the two-sided welding process. But laser welding does not require such a hole. Adopting Laser welding however requires part modification to suit the process. Thereby, engineers enjoy additional options in the balancing of strength versus weight. Volkswagen in Germany was an early adopter of this technology.

North American Market Assessment

Currently the total laser welding market in North America is about $175m. Automotive applications account for more than half of the total Laser welding market. Yet, according to a report by Frost & Sullivan, the total penetration of Laser Welding in the automotive industry is only 5-10%.

The Auto industry in North America is shifting significantly towards laser welding from the traditional approach of spot welding for automotive body components. Volkswagen is the most aggressive manufacturer for using lasers in the body shop. But other experienced European users like Volvo, Opel and Mercedes are transferring laser technology to Ford, GM and Chrysler in North America through their respective business alliances.

Current applications include welding the roof of the body to the frame. Another area of application is under-the-hood electronic enclosures. Among suppliers, ArvinMeritor is known to use laser welding in the wheel hubs in their plant in Brazil. In a report by Jay

Baron, Director of Manufacturing Systems at the Center for Automotive Research (CAR), based in Ann Arbor, the auto industry is now considering expanding use of laser welding.

This trend can be supported by enabling laser welding to be a solution to reduce scrap caused by welding failures. Of the 14 million vehicles annually produced in North America, it is estimated that 1% of body structures are either destroyed during testing to identify weld quality issues or otherwise require re-work due to welding defects. Since these are major components of a vehicle and re-work requires significant levels of manual labor, we conservatively estimate that the value of each lost body structure is $2000. The resulting estimate is that the North American automotive industry currently spends $280M as a direct result of inferior welding.

European and Other International Markets

The automotive sector is the single largest applications group accounting for $14.8 million of the UK laser welding equipment market by 2011. However, its market share will contract over the long term as Laser welding applications penetrate into other manufacturing sectors. The most rapid growth will be seen in the combined electronics and medical equipment sector, which by 2011, will account for 27.7 per cent of all laser welding revenues - ultimately overtaking the automotive sector in terms of revenue generation.

Germany accounts for more than half of the total European market for Laser welding. Growth in the German laser welding equipment market will be based on a three-pronged platform: first, from existing users increasing their use of laser welding equipment for specific applications and from competitors within the same industry sector following

suit; second, from the development of new applications for existing technologies and; third, from the identification of innovative technologies for new applications. Together, these will extend the application range of laser welding and promote market expansion. Frost & Sullivan reported that the German Laser Welding Equipment Market earned revenues of $357.7 million in 2004 and estimates to reach $481.1 million in 2011.

Frost & Sullivan reports the market for Laser welding in Europe is constantly rising, from $542.8 million in 2004 to an estimated $802.2 million in 2011. This is an industry that employs a significant amount of metal joining per unit of output, and Laser welding offers ease of automation, high welding speeds and better weld quality. Apart from Germany, France and Italy are the other countries increasingly adopting this technology.

In Italy, the market is set to double from its position in 2004 by 2011. The Laser Welding Equipment market earned revenues of $ 41.8 million in 2004 and estimates to reach $77.7 million in 2011. The Fiat group of companies is a leader for laser welding in the automotive market. Figure A- 2 below summarizes the laser welding markets.

Laser Welding Equipment Market						
North America	**2008**	**2009**	**2010**	**2011**	**2012**	**2013**
Total Laser Welding Revenue	$175,000,000	$185,043,032	$195,662,422	$206,891,245	$218,764,477	$231,319,098
Automotive Laser Welding Revenue	$87,500,000	$88,995,726	$106,570,513	$125,641,026	$139,102,564	$152,564,103
United Kingdom						
Total Laser Welding Revenue	N/A	N/A	N/A	$63,166,383	N/A	N/A
Automotive Laser Welding Revenue	$14,800,000	$15,649,354	$16,547,451	$17,497,088	$18,501,224	$19,562,987
European Union						
Automotive Laser Welding Revenue	$678,544,903	$717,485,752	$758,661,367	$802,200,000	$848,237,261	$896,916,543

Figure A- 2 Laser Welding Opportunities in North America, UK, and EU (Not Incl. Monitoring Systems)

Welding Industry

Most of the welding applications are metal because fusion welding is the most popular and effective way of the joining metals. Prior to the estimate of the welding monitoring market, an estimation of the total welding market is informative.

The estimation of the world welding market (welding equipment and supplies) was $ 9.9 billion in 2002 and was $ 12.7 billion in 2007, with an average annual growth rate of about 5.0% as shown in Figure A- 3.

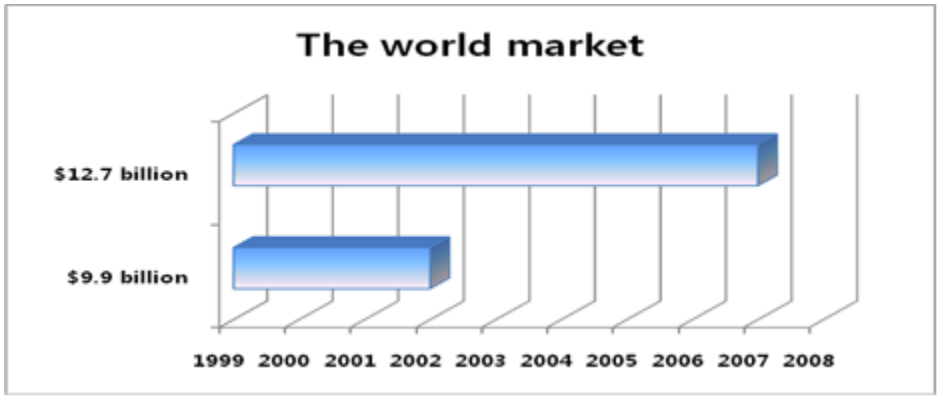

Figure A- 3 World Market for Welding

This value includes the most popular types of the welding methods, such as:

- Laser Welding (both Nd:YAG and CO_2 types)
- Shielded Metal Arc Welding (SMAW)
- Metal Inert Gas (MIG) Welding
- Flux Cored Arc Welding (FCAW)
- Tungsten Inert Gas (TIG) Welding
- Plasma Arc Welding (PAW)
- Oxy-Fuel Gas Welding (OFW, also known as brazing)
- Resistance Welding (also referred to as spot welding)

- Electron Beam Welding (EBW)

Within the same period, the welding market of North America was $ 3.9 billion in 2002 and was $ 4.6 billion in 2007, with an average annual growth rate in North America of about 3.5% as shown in Figure A- 4.

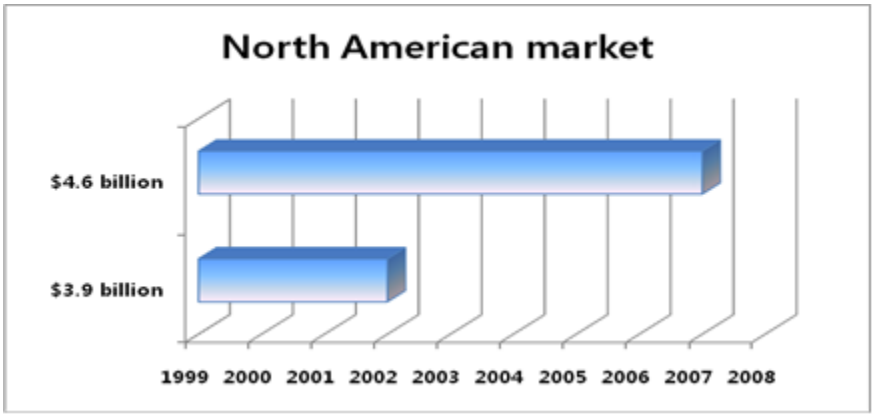

Figure A- 4 North American Market for Welding

As shown in two graphs below, the portion of the North American welding market size against the world market is getting smaller from 39% to 36%. The reason is that significant shares of manufacturing are moving away from the United States to emerging markets as indicated in Figure A- 5 .

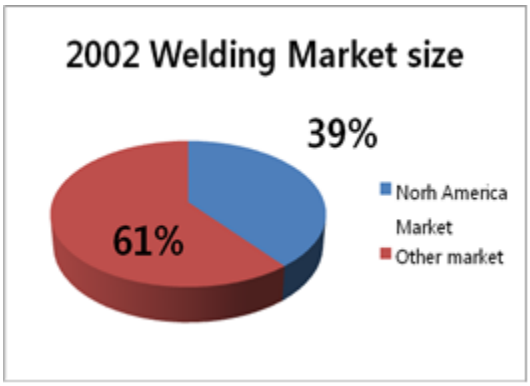

Figure A- 5 North American Share of World Welding Market

Among the welding methods, the application area of our technology requires a plasma (arc). In other words, the potential market includes arc welding and laser welding. As shown in the Figure A- 6 below, approximately 85% of the North America welding market consists of arc welding and laser welding. Based on the 2007 data, our total market size would be more than $ 3.91 billion.

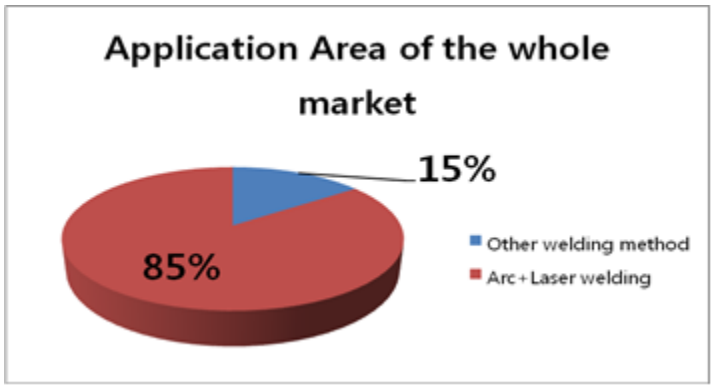

Figure A- 6 Relevant Share of Welding Market

By assessing the welding equipment and supply market, and assuming that the value of the welding processes is reasonably captured in that data, we can estimate the value from an improvement from 99% effectiveness (i.e. 1% scrap rate) to 100% effectiveness (i.e. 0% scrap rate) of the approximately 85% of the market which is relevant to our technology. For the North American market in 2007, this improvement would result in an increase of $40M in the welding market's value and for the world market in 2007 this assessment would be $108M. By generating application-specific value propositions, such as described above for the automotive market the potential is much more significant.

A.5. Company Strategy and Development Plan

To capture the value from building a knowledge base of specific welding defect characteristics, the technology will best be commercialized through building a stand-alone business rather than a licensing arrangement. One area of concern regarding our technology revolves around compatibility with existing welding equipment. We are aware that many of the end users of the technology have customized and complicated welding processes and existing equipment which is quite expensive to replace. Without compatibility with those existing processes it's likely that the switching costs for the end users will outweigh the benefits.

A.5.1. Interim Plan

To bring the technology from its current university research status to being a commercial entity with demonstrated value as an early stage investment. The current plan is for the company to be incorporated with Jyoti Mazumder taking the initial role of CEO and CTO. Jyoti currently fills this role at POM Group (see www.pomgroup.com), an early-stage company specializing in rapid product development and prototyping technologies. Seung Hwan Lee will serve as Lead Development Engineer focused on furthering the identification of signal characteristics for relevant applications. An additional team member is anticipated to serve as a Development Engineer working with Seung Hwan. An additional Development Engineer with relevant experience in electrical engineering and signal processing will need to be added to the team shortly to further the product development efforts. A CEO with early stage management experience should also be identified in the near term to replace Jyoti and take the company forward. The interim

activities are expected to be funded as the "Round A" of financing described below, which is planned to come from the founders, friends and family and grants.

A.5.2. Stage 1: First Two Years

Our first two years of operation will rely on getting our technology in a manufacturing setting so that OEMs can understand the merits of our technology, without convincing managers to authorize huge investments required to change processes. This will require us to develop our technology into a "bolt-on" application that allows OEMs to easily integrate it into their existing welding and manufacturing processes with our support. Although our resources will be fully devoted to integrating the bolt on application, during free time our sales team will be aggressively pitching the technology to welding machine manufacturers. Our plan is to integrate our technology into the welding machines that OEMs and other end users currently purchase when their existing machines become outdated and are replaced.

A.5.3. Stage 2: (Month 24 and On)

After two successful years developing and offering a bolt-on solution, we will begin to devote more development efforts to creating an integrated application with one or more welding system partners and fully building out an indirect sales channel through them. The first benefit is that new users who haven't adopted our technology as a bolt-on application may be more likely to try it if the cost is packaged into welding machines they would be buying anyway. Not only is the marginal cost relative to the welding machine very small, but if they are purchasing from a trusted welding machine supplier, that gives our product added validity. The second benefit comes from customers who have

experienced our technology through the "bolt-on" application, and want to continue use. As their existing welding machines are replaced by new welding machines, the option to have an integrated solution rather than a supplemental application purchased from us will likely be very attractive and encourage adoption within other divisions due to the simplicity and elimination of switching and integration costs.

A.6. Projected Financing Needs

Projected investment needs to develop the weld monitoring system into a profitable company are outlined below in Table A- 2, including the key milestones expected to be achieved as a result of each funding round (for example after the A funding but prior to the B funding the on-campus results are planned to be replicated). The objective is to transition to cash flow positive after the E round of funding. It should also be noted that some portion of the C and subsequent rounds could be generated from early customers or development partners. In particular, the add-on business is likely to begin generating cash flows in the third and fourth years which may offset the development costs of the integrated system.

The revenue opportunities that can be used to fund operations are outlined in Figure A- 6. The investment model shows three rounds of financing totaling under $ 4mm to bridge the venture to year three, when the company turns cash flow positive. Whether the VC chooses to harvest in 5 or 10 years, the multiples of invested capital available under our assumptions are very compelling given today's private equity environment.

Table A- 2 Projected Financing Needs and Milestones

Round	A	B	C	D	Self-funded
Equipment & Supplies	$89,700	$49,100	$44,300	$4,000	$10,100
Lab/Office Space	$12,000	$12,000	$18,000	$18,000	$18,000
Salaries	$200,000	$400,000	$1,200,000	$1,450,000	$1,700,000
Misc. out-of-pocket (travel, conferences etc.)		$20,000	$40,000	$40,000	$50,000
Total	$301,700	$481,100	$1,302,300	$1,512,000	$1,778,100
Duration:	6 months	6 months	1 year	1 year	1 year
Key Milestones:	Establish test capabilities off campus	Identify a partner with a manufacturing application to develop towards	Develop plant-ready demonstrator system	Scale add-on installation business	First bundled system sale
	Replicate on-campus results	Develop plant-ready prototype system	First add-on customer installation	Develop bundled welder system	Achieve positive cash flow
	Validate multiple welding processes/materials		Identify welding machine partner		
Assumptions	$35k ea. For two welding machines	One additional welding machine	One additional welding machine and spectroscope	Welding machine from partner	Replace 1st spectrometer
	$50k salary for two engineers, $100k salary for management team leader (CEO/CTO)	Hire dedicated sales/marketing professional, add two development engineers	Add finance manager, product manager	Add second product manager for bundled system, add tech. support engineer	Second support engineer, second sales professional
			Increase office/lab space 50%	Replace PCs from initial investment	

Laser Welding Monitoring for North American Auto Industry--Investment Model						
Year	**1**	**2**	**3**	**4**	**5**	**10**
Est. Production/ Yr	14,000,000	15,000,000	16,000,000	16,000,000	16,000,000	16,000,000
Penetration %	*10%*	*11%*	*13%*	*14%*	*16%*	*17%*
Scrap Rate	*1%*	*1%*	*1%*	*1%*	*1%*	*1%*
Scrap cost ($/part)	$2,000	$2,000	$2,000	$2,000	$2,000	$2,000
Value to Automotive Industry	$28,000,000	$33,990,000	$40,512,000	$44,800,000	$49,600,000	$54,400,000
% of Value Captured by Us	*0%*	*0%*	*5%*	*10%*	*15%*	*25%*
Our Revenue	$0	$0	$2,025,600	$4,480,000	$7,440,000	$13,600,000
Our Expenses	($782,800)	($1,452,300)	($1,612,000)	($1,828,100)	($3,009,214)	($5,500,714)
EBITDA	($782,800)	($1,452,300)	$413,600	$2,651,900	$4,430,786	$8,099,286
Multiple	N/A	N/A	5.0x	5.0x	5.0x	5.0x
Enterprise Value	N/A	N/A	$2,068,000	$13,259,500	$22,153,929	$40,496,429
Grant and Founder Inv.	$282,200	$0	$0	$0	$0	$0
VC Req. Inv if Single Round	$500,000	$1,300,000	$1,500,000	$0	$0	$0
VC Ownership Percentage	*9.20%*	*28.33%*	*46.00%*	*46.00%*	*46.00%*	*46.00%*
Post Money Value (25% Disc.)	$5,435,339	$6,794,173	$8,492,717	$10,615,896	$13,269,870	$40,496,429
Pre-Money Value	$4,935,339	$5,494,173	$6,992,717	$10,615,896	$13,269,870	$40,496,429
VC MOIC at Harvest	N/A	N/A	0.3x	1.8x	3.1x	5.6x

Figure A- 7 Laser Welding Monitoring Equipment Investment Model

A.7. Claims of Weld Monitoring System's Patent

Our technology currently includes all twenty-two out of the twenty-five claims made in the patent application.

1) The basic method that plasma light emitted from the welding process is read by an optical sensor and data is transferred to a computer to measure light intensity and electron temperature.
2) An optical lens that measures a specific spectral region
3) A spectral "region of interest" is identified which relates to identification of welding failures
4) There are two separate regions of interest for iron and zinc, which are relevant for galvanized steel used in automotive body structures.
5) Discusses the distance the optical lens is positioned from the weld.
6) Allows for a feedback control to adjust the welding process based on the monitoring system.
7) Allows for our technology to use more than one type of optical sensor, which is currently being utilized through two partially tested sensors we have successfully used to read the characteristics of the weld.
8) Clarifies that our technology is proprietarily protected to read two elements of the plasma light characteristics.
9) Clarifies how the two light elements are characterized as ratios to one another to read light intensity.

10) Clarifies how the two light elements are characterized as ratios to one another to read electron temperature.

11) Specifies the two elements in claim eight as iron and zinc, which are components of galvanized steel and are utilized in automobile, aerospace and shipping manufacturing industries.

12) Specifies the ratios of light and electron temperature emitted for iron and steel to each other.

13) Describes that the entire process is able to decipher whether a weld will be acceptable.

14) Fourteen

15) Extends the scope of the first two claims that the process reads plasma light during the welding process.

16) Further explains that it's specifically measuring light intensity and electron heat.

17-24) Claims seventeen through twenty-four specify the exact wavelength regions of the spectrum that our technology reads and allows for these "regions of interest" to be used in correspondence with the ratio measurements specified above.

25) Describes the hardware requirements for the weld monitoring system

BIBLIOGRAPHY

1. Glaze B, Goyal K, J T, Lee S H and Pollack M L. Commercialization plan of welding monitoring system. Finance 629 Report. Ross School of Business, University of Michigan, Ann Arbor, 2008.

2. Duley W W. 1999 *Laser Welding*. Wiley Inter-Science 161-165.

3. Shao J and Yan Y 2005 *Journal of Physics: Conference Series*. **15** 101

4. Allen S, Elijah Kannatey-Asibu, Jr. and Mark G 1999 *Journal of laser applications*. **11** 153-68

5. Liu X and Kannatey-Asibu J E 1991 *Journal of Applied Mechanics*. **58** 889-94

6. Mao Y L and Duley W W 1994 *Journal of physics D, Applied physics*. **27** 1379-83

7. Luo H, Zeng H, Hu L, Hu X and Zhou Z 2005 *Journal of Materials Processing Technology*. **170** 403-11

8. Xiangzhong J, Lijun L and Yi Z 2002 *Journal of Physics D: Applied Physics*. **35** 2304

9. Miyamoto I, Kamimuki K and Mori K 1993 *Proc SPIE Vol 2306, Laser Materials Processing, proceedings of ICALEO*

10. Park H and Rhee S 1999 *Optics & Laser Technology*. **31** 119-26

11. Sun A, Kannatey-Asibu J E and Gartner M 2002 *Journal of laser applications*. **14** 114-21

12. Tu J, Miyamoto I and Inoue T 2002 *Journal of laser applications*. **14** 146-53

13. Park Y W, Park H, Rhee S and Kang M 2002 *Optics and laser technology*. **34** 135-42

14. Rockstroh T J and Mazumder J 1987 *Journal of Applied Physics*. **61** 917-23

15. Ancona A, Spagnolo V, Lugarà P M and Ferrara M 2001 *Applied Optics*. **40** 6019-25

16. Balzer H, Hoehne M, Sturm V and Noll R 2005 *Spectrochimica Acta Part B: Atomic Spectroscopy*. **60** 1172-8

17. Sibillano T, Ancona A, Berardi V, Schingaro E, Basile G and Mario Lugarà P 2006 *Optics and Lasers in Engineering*. **44** 1039-51

18. Lober R and Mazumder J 2007 *Journal of Physics D: Applied Physics*. **40** 5917-23

19. Dasgupta A K, Mazumder J and Li P 2007 *Journal of Applied Physics*. **102** 053108-15

20. Akhter R and Steen W M, Year *Lasers in Manufacturing--Proceedings of the 5th International Conference (LIM-5)*.

21. Dasgupta A, Mazumder J and Bembenek M, Alloy based laser welding US Patent 6,479,168. 2002.

22. Steen W M and Mazumder J. 2010 *Laser Material Processing*. 4th ed. Springer 41-50.

23. Ki H, Mazumder J and Mohanty P 2002 *Metallurgical and Materials Transactions A*. **33** 1817-30

24. Kannatey-Asibu J E. 2009 *Principles of Laser Materials Processing* Wiley

25. Hou K-C and Galvanuaskas A. 2008 *High-Peak-Power Fiber-Laser Technology for Laser-Produced-Plasma Extreme-Ultraviolet Lithography PhD Thesis* University of Michigan.

26. Tünnermann A 2005 *Laser Technik Journal*. **2** 54-6

27. Giesen A and Speiser J 2007 *Selected Topics in Quantum Electronics, IEEE Journal of*. **13** 598-609

28. National Institute of Standards and Technology *Atomic Spectra Database Lines Form* 2011 Available from: http://physics.nist.gov/PhysRefData/ASD/lines_form.html.

29. Harvard-Smithsonian Center for Astrophysics *Astrophysics Data Base* 2011 Available from: http://www.cfa.harvard.edu/amp/ampdata/kurucz23/sekur.html.

30. Ki H, Mazumder J and Mohanty P 2002 *Metallurgical and Materials Transactions A.* **33** 1831-42

31. Park H and Sehun R 1999 *Optics & Laser Technology*. 119-26

32. Young W, Munjin K, Hyunsung P and Sehun R 2002 *Optics and laser technology*. **34** 135-42

33. Sun A, Kannatey-Asibu J E and Gartner M 1999 *Journal of laser applications*. **11** 153-68

34. Sabbaghzadeh J, Dadras S and Torkamany M J 2007 *Journal of Physics D: Applied Physics*. **40** 1047

35. Nek M S, Rashid B, Hafeez S, Jamil Y and Baig M A 2006 *Journal of Physics D: Applied Physics*. **39** 1384

36. Yi Z, Lijun L and Gang Z 2005 *Journal of Physics D: Applied Physics*. **38** 703

37. Griem H R. 2005 *Principles of Plasma Spectroscopy*. Cambridge University Press

38. Lacroix D, Jeandel G and Boudot C 1997 *Journal of Applied Physics*. **81** 6599-606

39. Lee S H and Mazumder J. 2009 *The International Congress on Applications of Lasers & Electro-Optics (ICALEO)* Orlando, FL Laser Insitutue of America.

40. Chang J J and Warner B E 1996 *Applied Physics Letters*. **69** 473-5

41. Nek M S, Hafeez S, Rashid B, Mahmood S and Baig M A 2006 *Journal of Physics D: Applied Physics*. **39** 4377

42. Vapnik V N 1999 *Neural Networks, IEEE Transactions on*. **10** 988-99

43. Vapnik V N. 1998 *Statistical Learning Thoery*. John Wiley & Sons, Inc.

44. Anabitarte F, Mirapeix J, Portilla O M C, Lopez-Higuera J M and Cobo A 2012 *Sensors Journal, IEEE*. **12** 64-70

45. Cristianini N and Shawe-Taylor J. 2000 *An introduction to support vector machines and other kernel-based learning methods*. Cambridge

46. Cortes C and Vapnik V 1995 *Machine Learning*. **20** 273-97

47. Chih-Wei H and Chih-Jen L 2002 *Neural Networks, IEEE Transactions on*. **13** 415-25

48. Burman P 1989 *Biometrika*. **76** 503-14

49. Kar A and Mazumder J 1994 *Physical Review E*. **49** 410-9

50. Xi C and Hai-Xing W 2001 *Journal of Physics D: Applied Physics*. **34** 2637

51. Knight C J 1979 *The American Institute of Aeronautics and Astronautics (AIAA) J*. **17**

52. Zhang C, Salama I A, Quick N R and Kar A 2006 *Journal of Applied Physics*. **99** 113530--10

53. Zhang C, Salama I A, Quick N R and Kar A 2006 *Journal of Physics D: Applied Physics*. **39** 3910

54. Rémy F, Frédéric C, Dominique G and Mathieu K 2006 *Journal of Physics D: Applied Physics*. **39** 401

55. Rémy F, Sonia S, Fréderic C and Francis B 2005 *Journal of Physics D: Applied Physics*. **38** 1881

56. Pan Y and Richardson I M 2011 *Journal of Physics D: Applied Physics*. **44** 045502

57. Osher S and Sethian J A 1988 *Journal of Computational Physics*. **79** 12-49

58. Sethian J A. 1999 *Level Set Methods and Fast Marching Methods*. 2nd ed. Cambridge University Press, Cambridge, United Kingdom

59. Bennon W D and Incropera F P 1987 *International Journal of Heat and Mass Transfer*. **30** 2161-70

60. Ki H, Mohanty P S and Mazumder J 2001 *Journal of Physics D: Applied Physics*. **34** 364

61. Ki H 2010 *Journal of Applied Physics*. **107** 104908-6

62. Knight C J 1979 *AIAA J*. **17**

63. Patankar S V. 1980 *Numerical Heat Transfer and Fluid Flow*. Taylor & Francis

64. Semak V V, Knorovsky G A, MacCallum D O and Roach R A 2006 *Journal of Physics D: Applied Physics*. **39** 590

65. Giesen A, Hügel H, Voss A, Wittig K, Brauch U and Opower H 1994 *Applied Physics B: Lasers and Optics*. **58** 365-72

66. Zenteno L 1993 *Lightwave Technology, Journal of*. **11** 1435-46

67. Gravel J-F Y, Doucet F R, Bouchard P and Sabsabi M 2011 *Journal of Analytical Atomic Spectrometry*. **26** 1354-61

68. Yousuke K, Masami M and Seiji K 2007 *Journal of Physics D: Applied Physics*. **40** 5854

69. Kim C, Kim J, Lim H and Kim J 2008 *Journal of Materials Processing Technology*. **201** 521-5

70. Thorne A, Litze U and Johansson S. 1999 *Spectrophysics:Principles and Applications* Springer 217-225.

71. Aragón C and Aguilera J A 2008 *Spectrochimica Acta Part B: Atomic Spectroscopy*. **63** 893-916

72. Konjević N, Ivković M and Jovićević S 2010 *Spectrochimica Acta Part B: Atomic Spectroscopy*. **65** 593-602

73. Shaikh N M, Hafeez S and Baig M A 2007 *Spectrochimica Acta Part B: Atomic Spectroscopy*. **62** 1311-20

74. Gornushkin I B, King L A, Smith B W, Omenetto N and Winefordner J D 1999 *Spectrochimica Acta Part B: Atomic Spectroscopy*. **54** 1207-17

75. Cowpe J S, Pilkington R D, Astin J S and Hill A E 2009 *Journal of Physics D: Applied Physics*. **42** 165202

76. Ribic B, Burgardt P and DebRoy T 2011 *Journal of Applied Physics*. **109** 083301-10

77. Bengoechea J, Aguilera J A and Aragón C 2006 *Spectrochimica Acta Part B: Atomic Spectroscopy*. **61** 69-80

78. Bredice F, Borges F O, Sobral H, Villagran-Muniz M, Di Rocco H O, Cristoforetti G, et al. 2007 *Spectrochimica Acta Part B: Atomic Spectroscopy*. **62** 1237-45

79. Charfi B and Harith M A 2002 *Spectrochimica Acta Part B: Atomic Spectroscopy*. **57** 1141-53

80. Bogaerts A and Chen Z 2005 *Spectrochimica Acta Part B: Atomic Spectroscopy*. **60** 1280-307

81. Radziemski L J and Cremers D A. 1989 *Laser-induced plasmas and applications*. Dekker 72-75.